Expedition Unknown: Characterizing and Modelling Perturbed Debris Disks in Search for Elusive Planets

by

Katherine Crotts
B.Sc., University of Washington, 2017
M.Sc., University of Victoria, 2020

A Dissertation Submitted in Partial Fulfillment of the
Requirements for the Degree of

DOCTOR OF PHILOSOPHY

in the Department of Physics & Astronomy

© Katherine Crotts, 2024
University of Victoria

All rights reserved. This dissertation may not be reproduced in whole or in part, by photocopying or other means, without the permission of the author.

Expedition Unknown: Characterizing and Modelling Perturbed Debris Disks in Search for Elusive Planets

by

Katherine Crotts
B.Sc., University of Washington, 2017
M.Sc., University of Victoria, 2020

Supervisory Committee

Dr. Brenda Matthews, Co-Supervisor
(Department of Physics & Astronomy)

Dr. Ruobing Dong, Co-Supervisor
(Department of Physics & Astronomy)

Dr. Gaspard Duchêne, Outside Member
(Department of Astronomy, University of California, Berkeley)

ABSTRACT

Debris disks, which are defined as optically thin, dusty disks around main sequence stars, are intimately connected with planets in their systems. Not only does the mere existence of a debris disk suggest the presence of planets, as they efficiently stir the orbits of planetesimals leading to collisional evolution, but they can also easily shape the morphologies of their disk. To better understand planet-disk interactions, one crucial step is to uncover the variation in disk morphologies that are present in currently resolved disks. Further studies can then be done to understand how these disk morphologies are related to known or unknown planets.

In my thesis, I conducted a uniform, empirical analysis of 23 debris disks imaged with the Gemini Planet Imager (GPI) in polarized intensity. For this study, I characterized each disk through multi-wavelength, near-IR data to identify any asymmetries present. I find that the majority of disks (19/23) present a significant asymmetry in either geometry, surface brightness, disk color, or a combination of the three. These findings suggest that perturbations in our sample, as seen in scattered light, are common. Some of these perturbations are consistent with planet-disk interactions, including surface brightness asymmetries, eccentric disks, and warps. Additionally, I identified several possible trends between disk properties and stellar properties that may give further insight into debris disk evolution. This includes a trend between disk color and stellar temperature, and trends between the disk vertical aspect ratio and stellar temperature in tandem with the disk radius.

Within the GPI disk sample, I identify one of the most asymmetric disks, HD 111520. In another empirical analysis, I take a closer look at the HD 111520 debris disk to better understand its complex morphology. Using both polarized and total intensity multi-wavelength GPI observations, alongside observations taken with the Hubble Space Telescope (HST), I confirm that the disk hosts a variety of asymmetrical features and structures. This includes the strong 2 to 1 brightness asymmetry observed in previous studies, as well as a significant disk color asymmetry, a distinct 4° degree warp from the disk midplane past ∼180 au, and a bifurcation or "fork"-like structure on the NW side. While the color asymmetry and extreme brightness asymmetry suggests that the disk may have undergone a recent giant collision, the warp and fork structures strongly suggests the presence of an unseen planet.

Once these complex disk structures/features are identified, the disk morphology can effectively be used to probe unseen planets. In the final part of my thesis, I used

the n-body code REBOUND to simulate the features of the highly asymmetrical disk around HD 111520 via planet-disk interactions. I find that a planet with a mass of $\approx$1 M_{jup}, that is on an eccentric and inclined orbit outside of the warp location, can create a similar radial asymmetry, warp, and "fork"-like structure in the disk as seen in observations. This work demonstrates how disk morphologies can be used to constrain the mass and orbit of a hidden planet in a perturbed debris disk system.

CONTENTS

LIST OF TABLES

LIST OF FIGURES

ACKNOWLEDGEMENTS

I would first like to acknowledge with respect the Lekwungen (Songhees and Esquimalt) Peoples on whose territory the University of Victoria stands and where the majority of this thesis took place. I acknowledge the Lekwungen and W̱SÁNEĆ Peoples whose historical relationships with the land continue to this day.

I owe my biggest thanks to my supervisor **Brenda Matthews** who saw my potential when not many others did, and taking me on as a graduate student. I would have never gotten this far in my career and had as many amazing opportunities without your support and guidance. I truly could not have asked for a better supervisor. I would also like to thank my co-supervisor, **Ruobing Dong**, and my external, **Gaspard Duchêne**, for their additional support over the course of my graduate career. Finally, I'd like to thank the rest of the **GPI Collaboration**, which consists of a welcoming and inclusive group of people who I have learned so much from.

I would like to thank my sister in crime, **Jaclyn Jensen**, who's friendship has been the highlight of grad school. I truly could have not asked for a better and more caring person to call my best friend. Thank you for hyping me up when I'm down, being my maid of honor, and climbing all the mountains in Victoria with me!

I'd also like to give shout outs to **James Metcalfe** for being a wonderful friend and roommate, as well as for teaching me Japanese. Shout out to **William Thompson** for your intelligence, kindness, and bringing into my life your amazing wife, **Natalie Thompson**, who is unmatched in her humor and hosting skills. To my friends back home, namely **Shelby Sauer** and **Nico Lindblom**, who continue to support me even from across borders. Finally, to my fellow disk group: **Jess Speedie, Dori Blakely, Shunyuan Mao, Camryn Mullin, Xiaoyi Ma, Mars Eduardo,** and **Lowell Peltier**.

To my life partner and husband, **Tyler Bates**. I'm so grateful for your love and support over the last 11 years. Through highs and lows, you are always there for me, and I can always depend on you no matter what. You are my rock, and I can't wait to continue this journey with you.

Finally, I'd like to acknowledge my pup, **Sir Blueberry the first**. The best and cutest Corgi a girl could ask for, and the light of my life. Enough said.

Not all who wander are lost.
J.R.R Tolkien

DEDICATION

To my friends and family, especially my parents who have provided me unconditional love and support. Also to **me** and my determination and perseverance in finishing this degree, I could not have gotten here without it!

Chapter 1

Introduction

1.1 Stating the Problem

Over the last two decades, observations and studies have shown that there is an intimate connection between debris disks and planets (i.e. Wyatt 2005, 2006). An increasing number of debris disk observations have shown that they host a wide variety of morphologies such as warps, gaps, and eccentric disks; structures that are associated with sculpting from a planet. While the morphologies and complex structures of debris disks are often associated with planets, it is difficult to confirm that this is the case, when the planets themselves are not easily detectable.

One reason that these planets cannot be currently observed is due to biases in current exoplanet detection methods. Whereas detection methods such as transit and radial velocity are biased towards larger planets close in to their host star ($\sim 0.01-10$ au), other methods such as direct imaging are biased towards young, massive planets ($\sim$multi-Jupiter mass) at larger separations from their host star. Given that observed debris disks are often young Kuiper belt analogues at $\sim$20-50+ au from their star (see Figure 3 in Hughes et al. 2018), any planets detected via the transit or radial velocity method are most likely not dynamically coupled with the disk. Therefore, in debris disk systems where planets are not observed, we may be inferring a planet population of gas giant analogues, i.e. longer orbit planets, that are smaller ($\sim$1 M_{jup} and below) than what can currently be detected with direct imaging.

If we want to fully understand the connection between debris disk morphology and sculpting by planets, the presence of these unseen planets need to be confirmed. Doing so will help validate our assumption of planet-disk interactions, and will also allow us to more confidently extrapolate planetary properties from substructures of

Figure 1.1: Schematic of the different components that make up a debris disk architecture in comparison to the solar system, as well as an illustration of a a stellar SED and how each component makes up the SED. Figure from Hughes et al. (2018).

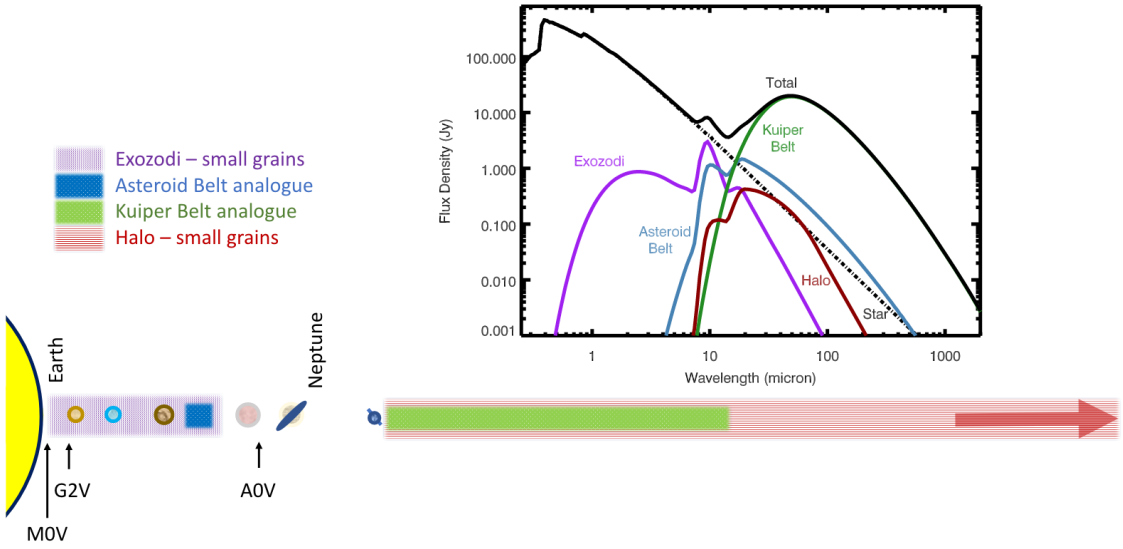

current and newly resolved debris disks. Unveiling this planet population of gas giant analogues is crucial, as it increases our knowledge of exoplanetary architectures and demographics. Additionally, by directly connecting debris disks and planets, this work will have important implications for the evolution of exoplanetary systems.

1.2 Debris Disks and their Connection to Planets

Our Solar System is comprised of 8 planets, alongside two planetesimal belts; the Asteroid belt and the Kuiper belt. The structure and evolution of these two belts have been largely dominated by the planets in our system. Whereas the Asteroid belt is shaped by the gravity and orbit of Jupiter (e.g. Delgrande & Soanes 1943; Petit et al. 2001), the Kuiper belt has been shaped by the gravity and orbit of Neptune (e.g. Malhotra 1995; Thommes et al. 2002; Hahn & Malhotra 2005). Both planetesimal belts, consisting of TNOs (Trans-Neptunian Objects), asteroids and comets, are considered our Solar System's debris disk.

As in our Solar System, debris disks around other stars can be thought of as the aftermath of planet formation during the protoplanetary disk phase which takes place during the first few million years of a star's lifetime. While the primordial (i.e originating from the initial molecular cloud which also formed the star) gas and dust

of the protoplanetary disk eventually disperse, the rocky bodies that were formed in the disk remain. While we cannot detect the individual planetesimals themselves, we can detect the plethora of dust that reside in these belts. Figure 1.1 presents a schematic of a debris disk architecture which show the different dust components that make up the disk with reference to our own solar system. This includes the exozodi dust close to the star, the Asteroid and Kuiper belt analogues, as well as the disk halo which consists of small dust grains on hyperbolic orbits.

The fact that we observe such dusty debris disks in the first place is significant, as forces such as radiation pressure from the star are able to clear out dust grains on relatively short timescales (∼a couple hundred years, Artymowicz 1997). Therefore, we know that the dust in debris disks must be continually replenished. Such replenishing is done through a process called a "collisional cascade", where the rocky planetesimals left over from the planet formation phase are continually colliding and generating new dust grains in the process. Additionally, in order for collision between planetesimals to occur, the orbits of these planetesimals must be perturbed. Given that we now know that planets are extremely common and likely to be around most stars, planets are thought to be a likely source of perturbation of planetesimal orbits, meaning that the mere presence of a debris disk may be an indicator of planets residing in the system.

If the existence of a debris disk suggests the presence of planets, the question is then whether or not these planets are also dynamically interacting with their disk, similar to how the planets in our solar system interact and shape the Asteroid and Kuiper belts. Unlike protoplanetary disks, debris disks are optically thin and relatively gas poor, meaning that planets can more easily exert dynamical forces onto the dust, shaping the disk and creating observable morphologies. Additionally, with the absence of more complex physics due to gas, which can also create structures such as rings and gaps, we can more confidently connect debris disk substructures to planets. However, in order to understand whether or not planet-disk interactions are taking place, we first need to fully understand the morphologies of these disks.

1.3 Detecting Debris Disks

Debris disks are found around ∼20% of young and main sequence stars of various ages (Thureau et al., 2014; Montesinos et al., 2016; Sibthorpe et al., 2018). Initially, debris disks are first inferred by their star's Spectral Energy Distribution (SED, see Figure

1.1), which measures the star's flux as a function of wavelength. This is because the presence of dust in the system boosts the flux at longer wavelengths, far above what we would expect solely from the star. For the last several decades, many debris disks have been inferred from their stellar SEDs using mid- to far-infrared (MIR and FIR, respectively), space based telescopes such as *The Infrared Astronomical Satellite* (IRAS), *Spitzer*, and *Wide-field Infrared Survey Explorer* or WISE. In fact, multiple surveys with these instruments have been used to discover hundreds of debris disks (e.g. Trilling et al. 2008; Chen et al. 2014; Patel et al. 2014), where Vega was the first debris disk to be detected with IRAS alongside β Pictoris, Fomalhaut and ϵ Eridani (Aumann et al., 1984; Neugebauer et al., 1984). Some of the more recent and more sensitive debris disk surveys include several from the FIR space-based telescope, *Herschel*, which detected many nearby disks through the DEBRIS (Sibthorpe et al., 2018) and DUNES (Montesinos et al., 2016) surveys.

However, one issue is that the SED only provides limited information on the disk, such as its potential radius, temperature, and brightness compared to the star, whereas the SED does not provide any information on the shape or extent of the disk. Therefore, debris disks must be spatially resolved with direct imaging in order to obtain such information. Similar to planets, debris disks are relatively faint objects, and therefore need specialized instruments to image and resolve them. This endeavour is important, as spatially resolving debris disks allows us to characterize their morphologies and connect their structures to possible planets in the system.

Beginning with the first ever directly imaged debris disk, β Pic (Smith & Terrile, 1984), shortly after it was discovered with IRAS, this observation paved the way for other directly imaged debris disk observations using a variety of instruments. One of the earliest instruments includes the *Hubble Space Telescope* (HST), which has been fundamental for debris disk imaging in the optical and NIR (e.g. Schneider et al. 2014), observing nearby debris disks such as β Pic as early as the 90's (Kalas & Jewitt, 1995), and continues to be one of the best disk imagers to this day. Other instruments such as *Spitzer* and *Herschel* have also imaged many debris disks in the MIR and FIR, where the disk flux peaks, although these observations are not fully resolved given the large beam sizes of these instruments (e.g. Stapelfeldt et al. 2004; Su et al. 2005; Matthews et al. 2010). In more recent years, even better instruments revolutionized the field further by imaging a plethora of debris disks in the NIR and at millimeter wavelengths with higher spatial resolution. These includes instruments such as *Spectro-Polarimetric High-contrast Exoplanet REsearch*

Figure 1.2: **Top:** Observations of the debris disk, Fomalhaut, at various wavelengths including the optical with HST (panel a, Kalas et al. 2013), FIR with Herschel (panel b, Acke et al. 2012) and the millimeter with ALMA (panel c, from MacGregor et al. 2017). **Bottom:** HST optical scattered light image of the AU Mic disk (Schneider et al., 2014) overlaid with contours of the 1.3 mm ALMA thermal emission. Figure from Hughes et al. (2018).

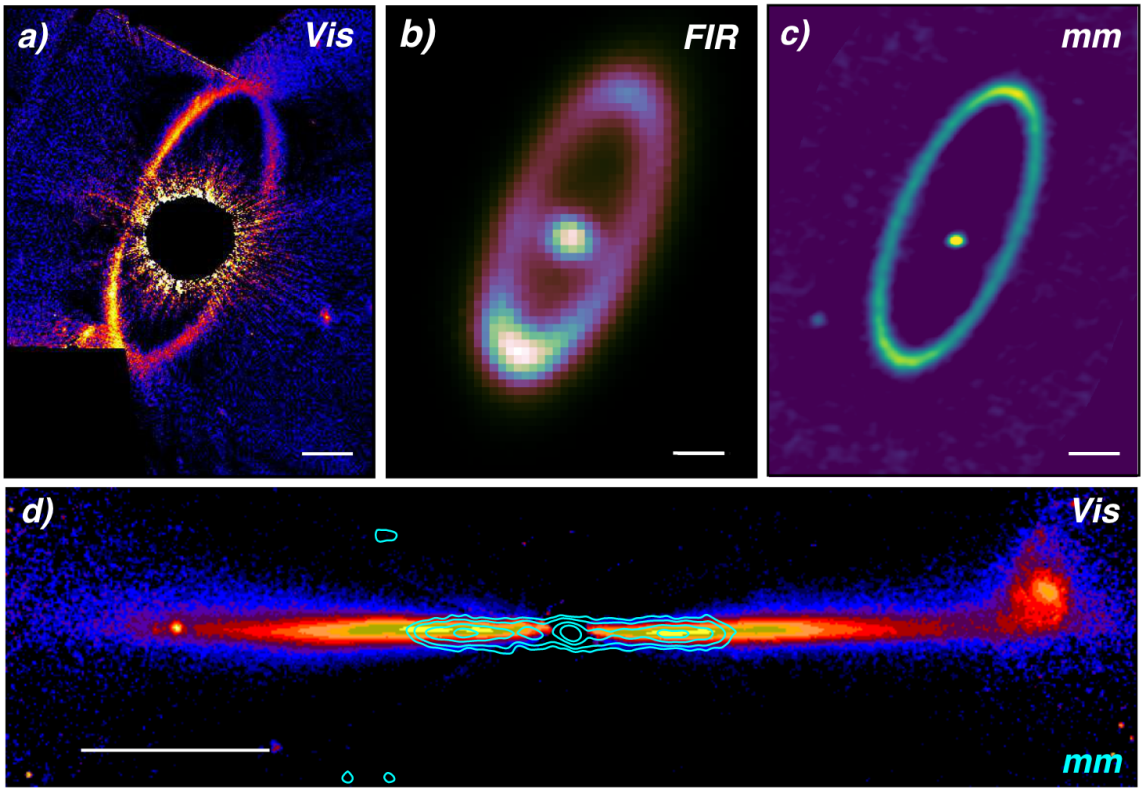

or SPHERE (e.g. Langlois et al. 2021), the *Gemini Planet Imager* or GPI (discussed further in Section 1.5) (e.g. Esposito et al. 2020), and the *Atacama Large Millimeter/submillimeter Array* or ALMA (e.g. Lieman-Sifry et al. 2016; MacGregor et al. 2022).

The wavelength at which a debris disk is observed can provide distinct but equally important information about the disk. Dust grains in particular are most efficient at scattering (from the star) or thermally emitting light with wavelengths close to the size of the dust grains themselves. This means that we are probing different sized populations of dust grains depending on the wavelength of the observation. Additionally, whether or not an observation is dominated by scattering or emission, again depends on the wavelength as well as the star. For example, at optical wavelengths where the star is bright, we are primarily probing scattered light off the smallest dust

grains that populate the disk halo, i.e. sub-micron sized grains that are actively being blown out by radiation pressure from the star and are on highly eccentric orbits. At NIR wavelengths, scattering still dominates; however, we are probing slightly larger micron-sized dust grains which populate the main planetesimal belt, i.e. the Kuiper belt analogue as seen in Figure 1.1. At FIR and millimeter wavelengths, where the star is dim and the disk is at its brightest, we are primarily probing the thermal emission of the larger dust grains, which again populate the main planetesimal belt and hold the majority of the dust disk mass. These larger dust grains are also less affected by radiation pressure and therefore are more concentrated radially. Figure 1.2 visually shows how the dust extent and emission varies as function of observations wavelength.

While it is important to have multiwavelength observations to fully understand a disk's morphology, in this thesis, I will focus entirely on scattered light observations of debris disks in the optical and NIR, therefore probing sub-micron to micron sized dust grains in the disk halo and planetesimal belt. This is due to several factors; Mainly, it is much easier in many cases to obtain high resolution images of debris disks in the optical and NIR. For example, it often requires less exposure time due to the brightness of scattered light at short wavelengths (where the star is brightest) compared to emitted light in the millimeter, allowing for more efficient observations. Additionally, the sub-micron to micron sized dust grains are often much more radially extended compared to millimeter sized grains, which again are more radially concentrated close to the star, making the smaller grains easier to resolve. This leads to a wealth of a high resolution observations in the optical and NIR which allow for characterization of their morphologies.

1.4 High-Contrast Imaging

Because debris disks are much fainter than their host stars in scattered light, this requires instruments that can reach deep contrasts (contrast = $\text{Flux}_{disk}/\text{Flux}_{star}$) in order to separate the disk signal from the star. Such contrasts can be reached with high-contrast imaging (HCI) which includes a variety of techniques, such as adaptive optics (AO), coronagraphy, and differential imaging techniques (Oppenheimer & Hinkley, 2009; Follette, 2023).

For ground based instruments, AO is particularly important, as the Earth's atmosphere distorts the incoming light. With AO, light distorted by the atmosphere

is corrected through the use of deformable mirrors, while wavefront sensing is used to measure these distortions on millisecond timescales in order to determine how the mirror deforms. The use of coronagraphs is also important for HCI, both for ground and space-based instruments, as coronagraphs block the light from the star, allowing for fainter objects around the star to be revealed. Finally, differential imaging techniques can be used to further improve the contrasts of an observation through removing the point stellar function (PSF) of the star.

In this thesis, I focus on two particular differential imaging techniques, angular differential imaging (ADI, Marois et al. 2006) and polarized differential imaging (PDI, e.g. Brandner et al. 2005). ADI works on the basis that the stellar PSF does not change as the sky rotates over the course of an observing sequence. Therefore, to employ ADI, the telescope is fixed on the target but does not rotate with the sky, leading to a series of images of the target at different rotation angles. This allows for the separation of the stellar PSF signal from the target signal as the latter will rotate throughout the sequence, while the stellar PSF remains static. In addition to ADI, PDI is a particularly useful tool for imaging disks, as dust grains are very efficient at polarizing light from the star and primarily polarize light in the linear direction. PDI is one of the most successful disk imaging techniques as light from the star itself is inherently unpolarized, allowing for disk imaging with minimal interference from the star. While the polarized intensity of the disk is only a fraction of its total intensity, the use of PDI can often detect fainter disks, due to the fact that subtraction of the stellar PSF is unnecessary. Such PSF subtraction, which is required for total intensity observations, can often lead to subtraction of the disk close to the star, where there is less angular rotation of the disk signal. Therefore, polarized light observations can also give a better representation of the true disk structure.

To summarize, HCI is key to spatially resolving faint debris disks for optical to NIR scattered light observations. There are several instruments that employ HCI, and have been used to observe many debris disks. This includes the The Space Telescope Imaging Spectrograph (STIS) on HST, SPHERE on the Very Large Telescope, The Subaru Coronagraphic Extreme Adaptive Optics (SCExAO), and for this thesis, the Gemini Planet Imager.

Figure 1.3: Gallery of debris disks imaged with GPI in H band polarized light. Figure from Esposito et al. 2020.

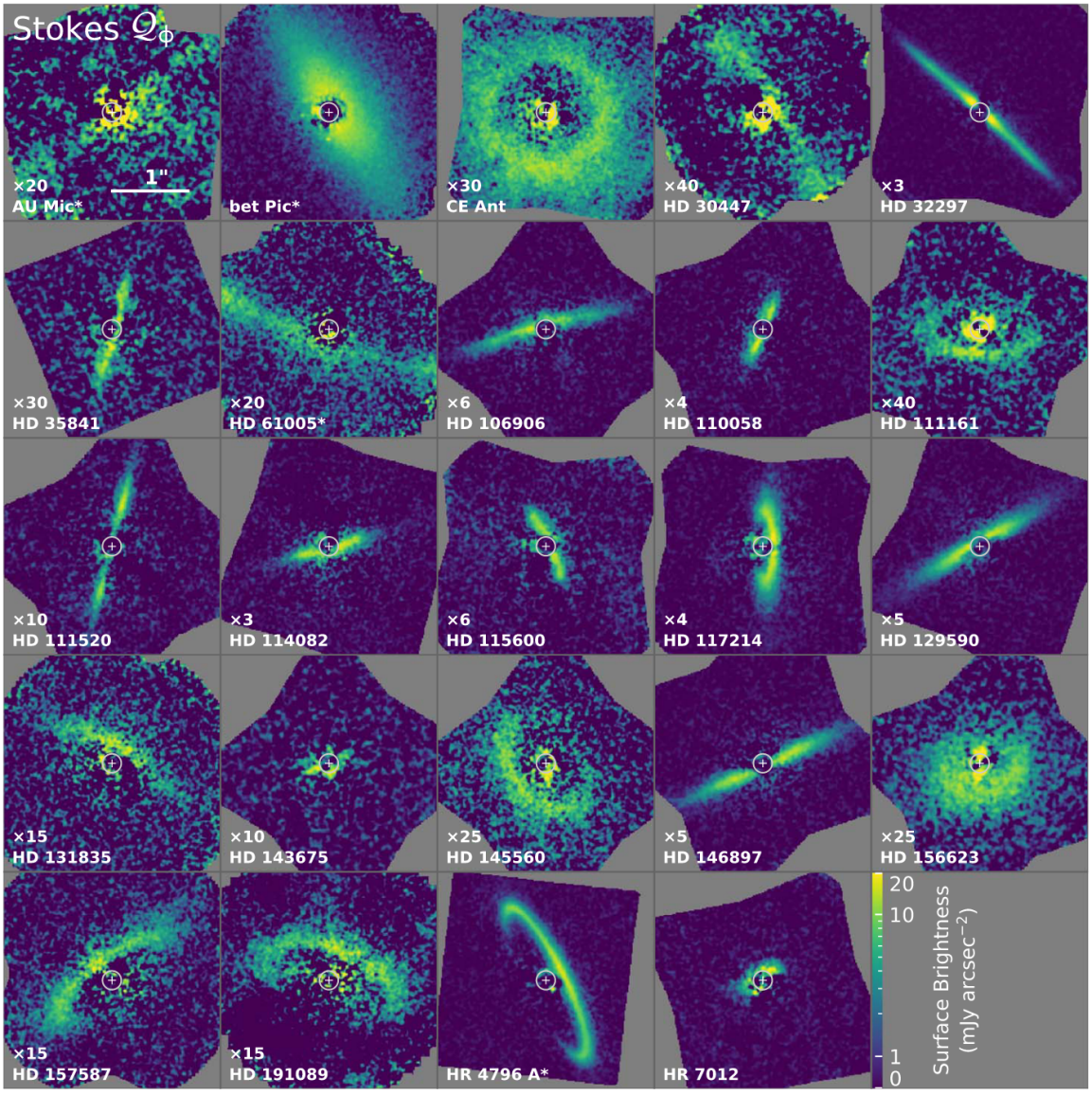

1.5 The Role of the Gemini Planet Imager

The Gemini Planet Imager (GPI) is a NIR instrument that was installed at Gemini South in the Andes of Chile from 2014 - 2022. It is currently being upgraded to GPI 2.0 and will then be deployed on Gemini North on Maunakea, Hawaii. GPI is considered an *extreme AO* (Guyon, 2018) instrument, meaning that its AO system is optimized to deliver a high degree of wavefront sensing compared to regular AO systems, allowing GPI to obtain an even deeper contrast. In addition to its deep contrast capabilities, GPI also has total intensity and polarized intensity modes, and can achieve small inner working angles (IWA), meaning that it can achieve deep contrasts close to the star. While GPI, as the name suggests, was designed with the goal of imaging planets, its capabilities make it the perfect debris disk imager as well.

Between 2014 and 2018 GPI conducted a large 800 hour campaign, named the Gemini Planet Imager Exoplanet Survey (GPIES, PI B. Macintosh), dedicated to searching for Jupiter sized planets around ∼600 nearby stars (Macintosh et al., 2018). During this campaign, GPI also imaged a large sample of debris disks in both polarized and total intensity, resolving a total of 26 debris disks in H band ($\lambda_c \sim 1.65$ μm), 2 of which were imaged in scattered light for the first time (Esposito et al., 2020). The sample of GPIES disks imaged in polarized light can be seen in Figure 1.3. In addition to the H band observations taken by GPIES, other GPI surveys have imaged many of these disks in the J ($\lambda_c \sim 1.25$ μm) and $K1$ ($\lambda_c \sim 2.05$ μm) bands as well, supplying multiwavelength data. These observations provide some of the highest spatial resolution images of the planetesimal belts for these debris disks to date (∼0.0142 arsec/pixel), allowing for detailed characterization of the disk morphology in scattered light. The GPI sample of disks also provides an opportunity to employ a uniform, multiwavelength analysis to compare the different disk morphologies and search for trends (see Chapter 3).

1.6 Current Work/Understanding on Planet-Disk Interactions

As we spatially resolve more and more debris disks, we find a multitude of different morphologies such as warps, gaps, narrow rings, eccentricities, brightness asymmetries, etc (see Figure 1.4). Many of these morphologies can be explained by planets,

Figure 1.4: Composite figure of disk structures. Debris disks show a variety of dust substructures across the wavelength spectrum. Some are narrow rings but many are broad belts, some with gaps. Edge on disks can show warps, such as the well-studied β Pictoris disk (Panel e). Figure from Hughes et al. (2018).

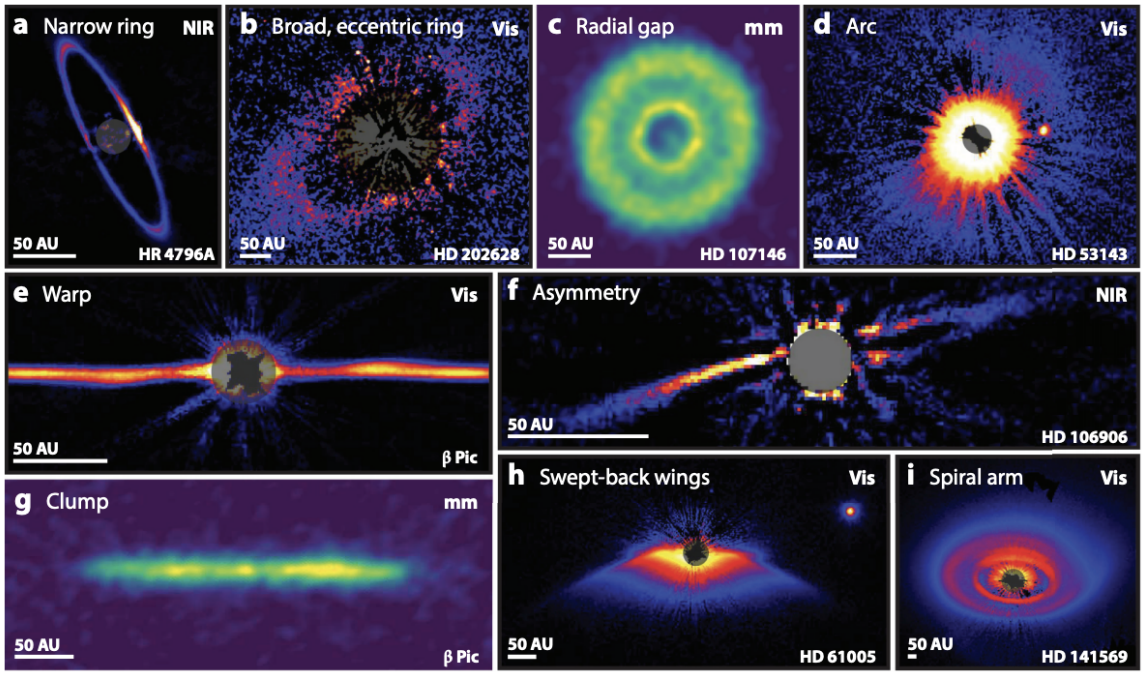

although we are often not able to directly image such planets. There are very few systems in which a planet has been directly detected and an associated debris disk has been well resolved. Such cases include β Pic, HD 95086, HR 8799, and HD 106906 (Lagrange et al., 2010; Macintosh et al., 2014; Marois et al., 2008, 2010; Bailey et al., 2014) which harbour young and massive multi-Jupiter sized planets which can be directly imaged given their size and location. For these particular examples, the morphologies of the known debris disks can be directly linked to the known planets. For example, the dramatic warp of the edge-on disk of β Pic (Mouillet et al., 1997; Heap et al., 2000) led to the prediction of the planet β Pic b, detected over a decade later (Lagrange et al., 2010). This confirmed exoplanet-disk connection of β Pic reinforced the expectation that substructure and asymmetries in debris disks could be a reliable signpost of planetary systems, and even reveal their likely mass and location relative to the disk structures (e.g., Hughes et al. 2018 and references therein).

In the majority of debris disk systems, however, no planets have yet been detected. One explanation is that planets do not need to be massive to sculpt their disk, therefore, it is likely that the responsible planets are simply below the sensitivity of current

direct imaging instruments. Due to this issue, indirect methods over the past decade have been focused on characterizing disk morphologies, N-body simulation work and inferring planets via other dynamical arguments such as disk stirring and inner edge sculpting.

1.6.1 Characterizing debris disk morphologies

To understand the relationship between planets and disks, It is important to first understand the different types of morphologies that debris disks present. Characterizing the morphologies of spatially resolved debris disks is work that has been conducted since the first debris disk, β Pic, was directly imaged in 1984 (Smith & Terrile, 1984), and has also been the focus of my research as a graduate student (Crotts et al., 2021, 2022, 2024). Through this characterization, it has become clear that debris disks host a large variety of substructures as mentioned previously. These substructures suggest that debris disks are actively being sculpted by some mechanism, with planets being the most popular explanation.

The nature of these substructures can help determine the nature of the planet itself. For example, a disk that is eccentric suggests that the perturbing planet is also eccentric, or a warp (such as in the case of β Pic) suggests that the planet is on an inclined orbit relative to the disk. Additionally, other features, such as the size of the disk gap can be used to estimate the planet's mass (Faber & Quillen, 2007). These are important quantities to constrain in order to understand the feasibility of detecting the planet with a particular detection method and/or instrument.

1.6.2 N-body simulations

Once the variety of disk morphologies is established, N-body simulations can be utilized in attempt to replicate these morphologies via planet-disk interactions. N-body simulations are a useful astronomical tool, as it allows one to model the dynamical evolution of an object or system. For the application of debris disks, N-body simulations are typically set up with a central star and a planet with a defined mass and orbit, while the disk is modelled as a collection of massless particles. By integrating this scenario over time, we can better understand how the defined planet affects the morphology of the disk. This tool has been used to replicate certain disk structures using planet-disk interactions, as well as constrain the orbit of known planets in systems with debris disks.

Figure 1.5: Debris disk morphologies created from an N-body simulation using a 10 $M_\oplus$ on an eccentric orbit. Such morphologies are observed in several known debris disks. Figure from Lee & Chiang 2016.

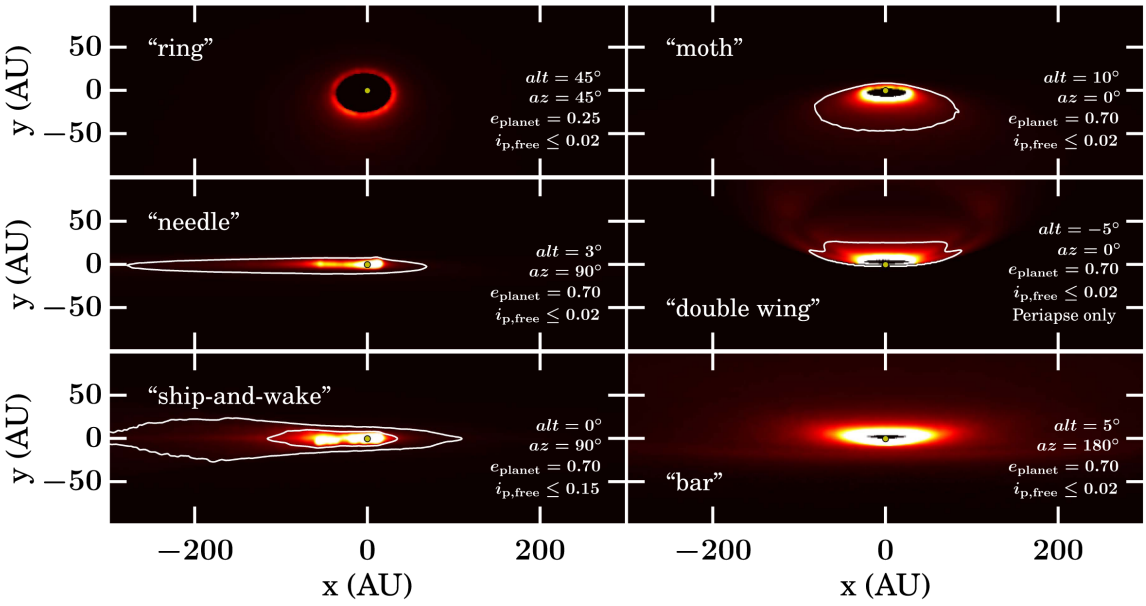

For example, Lee & Chiang (2016) found that by simulating an eccentric, 10 $M_{\oplus}$ planet orbiting within the disk inner edge, they were able to recreate multiple morphologies observed in known debris disks including the "Moth" (e.g. HD 61005; Hines et al. 2007) and the "Needle" (e.g. HD 15115; Kalas et al. 2007). These morphologies consist of several types of substructures/asymmetries, such as brightness asymmetries, radial asymmetries and eccentric disks that are viewed at different angles from Earth. Examples of some of the different disk morphologies created can be seen in Figure 1.5. This work also demonstrates how a planet as small as 10 $M_{\oplus}$ (Neptune = 17 $M_{\oplus}$ for reference) can easily shape its disk.

In cases where planets are known, N-body simulations have been used to confirm that the planet is responsible for perturbing the disk, and to help constrain its orbit. For example, such work has been done for the system HD 106906, which harbours both an asymmetrical disk and known planet which orbits far outside the disk ($a \approx 730$ au, (Bailey et al., 2014)). Nesvold et al. (2017) found that the 11 M_{jup} planet, HD 106906 b, on an eccentric orbit can create a similar disk morphology as observed, including the disk's eccentricity, brightness asymmetry, and needle-like halo. Additionally, this work helped place constraints on the planet's relative inclination to the disk, suggesting that the inclination cannot be more than 10° or else the disk would become too vertically warped. Later work done by Moore et al. (2023) also showed, with the use of N-body simulations, that the current configuration of HD 106906 system must have occurred relatively recently, or else, again, the disk would be too warped and puffy.

These mentioned works give examples of how N-body simulations can be used to replicate disk morphologies through planet-disk interactions, as well as used to infer the evolution and properties about the perturbing planet. Similar work can be done to help constrain the orbit and mass of disk perturbing planets by simply modelling a disk's morphology (see Chapter 5).

1.6.3 Stirring and sculpting arguments

A planet can sustain the detectability of a debris disk by dynamically exciting the planetesimals, also known as stirring (Wyatt, 2008; Mustill & Wyatt, 2009). This occurs through secular perturbations by the planet which excite the relative velocity and eccentricity of the planetesimals, causing them to eventually collide and produce the observable dust. In this case, the planet mass and eccentricity determine the

Figure 1.6: Planets inferred from disk stirring (red) and sculpting arguments in the case of a single planet (green) or multiple, smaller planets (blue). Black x's represent planets predicted from protoplanetary disks Figure taken from Pearce et al. (2022).

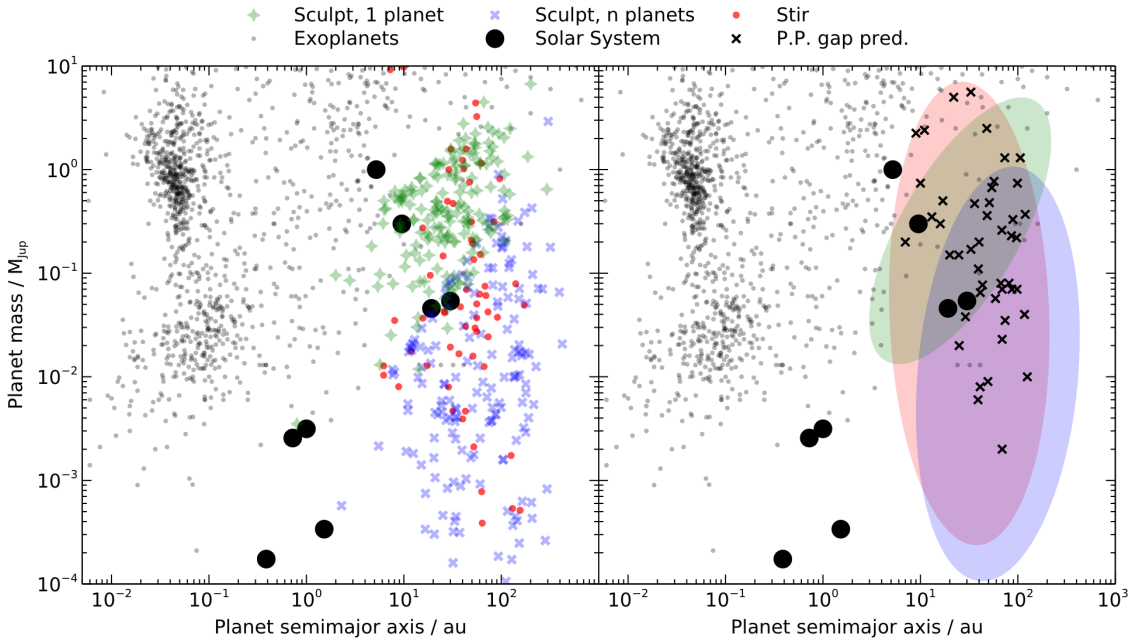

degree of stirring and excitation of the disk which is represented by the disk radial width (i.e. the more excited the planetesimals, the wider the disk) or the shape of the outer disk edge (Marino, 2021). Additionally, if the planet is close to the disk inner edge it can shape the disk by truncating the inner edge by removing nearby material, making it appear sharper (Pearce & Wyatt, 2014). Hence, these disk properties can also be used to estimate the mass and semi-major axis of possible planets shaping the disk.

As an example, Pearce et al. (2022) use these dynamical arguments to determine the planet mass and semi-major axis (assuming a circular orbit in most cases) required to stir or sculpt 178 debris disk systems using either thermal imaging observations with ALMA and Herschel, or SED data in the case that the disk is not spatially resolved. Results are shown in Figure 1.6, where the predicted planets are represented by the colored dots in the left figure. These results show how many of the predicted planets occupy a part of the planet mass/semi-major axis parameter space that has yet to be accessed with current instruments. This is because the predicted planets are too far from the star to be detected with radial velocity and the transit method, but are also too small to be detected with current direct imaging. While the James

Webb Space Telescope (JWST) may be able to image some of these planets, many may continue to allude us until future facilities see first light (e.g. the Roman Space Telescope).

Additionally, based on the predicted planet masses and semi-major axes, Pearce et al. (2022) are also able to come to several other conclusions. For example, given that the predicted planets from debris disks are similar to those predicted from protoplanetary disks suggests that planets may not significantly drift inwards as previously thought. The authors also find that self-stirring of the disk by the planetesimals alone leads to an unreasonably high disk mass, similar to previous studies (Mustill & Wyatt, 2009), again showing that planets are likely required to stir the disk. These results are another example of how debris disks can be used to infer small, wide-orbit planets, which have important implications on the architectures and evolution of exoplanetary systems.

1.7 Thesis Outline

In this thesis, I add upon the current work mentioned in the previous Section by analyzing the complex morphologies of debris disks in scattered light, and how these features may be connected to unseen planets in the system. To do this I take advantage of the large sample of multiwavelength GPI debris disk observations and other tools such as N-body simulations. The goal of my work is to characterize the GPI debris disks to search for perturbations from planet companions, and to connect certain disk morphologies directly to planets to infer their masses and orbits.

In Section 2, I explain the method of uniformly reducing the GPI J and $K1$ band polarized data, which previously had not been done for my sample. This step is important as uniformly reducing the J and $K1$ band datasets allowed me to effectively clean the datasets, and pull out as much disk signal as possible, leading to better characterization of each disk's morphology. I focus mainly on polarized intensity data, as they do not require PSF subtraction, meaning that they do not suffer from severe disk self subtraction such as is often seen in total intensity observations. Therefore, as mentioned previously, these polarized intensity observations give a better representation of the true disk structure.

In Section 3, I take my reduced J and $K1$ band datasets, alongside the H band observations reduced in Esposito et al. (2020), and perform a uniform, empirical, multiwavelength analysis. The goal of this work is to characterize the morphologies

of these GPI disks in a uniform manner, focusing on what we can learn directly from the data rather than using complex radiative transfer modelling. I also focus on any asymmetries/complex structures seen in the disk that may suggest the presence of a perturbing planet. Such a large sample of debris disks also allows us to look for broader trends between certain disk properties, as well as between the disk and its host star.

In Section 4 I take a closer look at one of the most asymmetric disks from the GPI sample, HD 111520. With GPI, the disk appears to have a large brightness and radial asymmetry, where the northwest side is almost 2 times brighter and more radially extended than the southwest side. Previous studies also show the possibility of a warp in the total intensity GPI data (Draper et al., 2016a), while HST data show the possibility of a bifurcation or "fork" like structure in the disk halo (Padgett & Stapelfeldt, 2015). Compared to Section 3, I conduct a deeper analysis of the disk morphology in both polarized and total intensity, while also measuring the structure of the disk halo to better understand the nature of its asymmetries.

Finally, in Section 5, I use the N-body code, REBOUND (Rein & Liu, 2012), to model the complex morphology of the HD 111520 disk based on our results from Section 4. By simulating planet-disk interactions over the course of the system's lifetime, I am able to recreate many of the disk's asymmetric structure. The goal of this work is to demonstrate how a planet may be responsible for the disk's morphology, as well as constrain the possible mass and orbit of the planet.

Chapter 2

GPI J and $K1$ Data Reduction

In recent years, high-contrast imaging has drastically improved in both resolution and sensitivity, which has allowed us to spatially resolve more debris disks than ever before. The Gemini Planet Imager (GPI), an extreme adaptive optics instrument located on Gemini South in Chile, is one of the most recent ground-based instruments optimized for exoplanet detection (Macintosh et al., 2014), but has also been one of the most fundamental instruments used to observe debris disks as well. As mentioned previously, through the GPIES campaign, 26 debris disks were imaged in polarized and/or total intensity, two of which were imaged in scattered light for the first time (Esposito et al., 2020).

While GPIES focused solely on H-band observations, other GPI surveys have additionally targeted these disks in multiple wavelengths. This includes an awarded Large and Long Program (PIDGS-2018A-LP-6), where roughly half of the debris disks observed through GPIES were also observed in the J and $K1$ bands. Unlike the H-band data, which have been uniformly reduced in Esposito et al. (2020), the J- and $K1$-band data had remained largely untouched. Furthermore, these fully reduced datasets are not widely accessible, limiting the usefulness of these datasets for further studies by the community.

In this chapter, I present my uniform reductions of the J and $K1$ data in polarized intensity, first published as a group in Crotts et al. (2024), which I will discuss in Chapter 3. These datasets were reduced similarly to the H-band data presented in Esposito et al. (2020), and were optimized to reduce the amount of noise in each image and recover as much disk signal as possible. Further details about the reduction process can be found in Section 2.1. In addition to the uniform J and $K1$ reductions, I plan to archive all three datasets (GPI J, H and $K1$ polarized intensity) on the

publicly accessible website, CANFAR, with the intention of making my reduced data easily obtainable for future research. Further details on this will be discussed in Section 2.2.

2.1 Observations & Data Reduction

The observations of the J ($\lambda_c = 1.25$ μm with $\Delta\lambda = 0.23$ μm) and $K1$ ($\lambda_c = 2.05$ μm with $\Delta\lambda = 0.29$ μm) data were executed over the span of several years, from December of 2015 through July of 2018 as part of the Debris Disk Large and Long Program (PI: C Chen). This included 10 disks observed in the J band and 11 disks observed in the $K1$ band, listed in Table 2.1. All data were taken in polarimetric ("J-Pol" and "K1-Pol") mode with a pixel scale of 14.161±0.021 mas per lenslet (De Rosa et al., 2020) and a field of view (FOV) of 2.8″ by 2.8″. In polarimetric mode, a rotating half-wave plate is utilized and positioned at angles [0.0°, 22.5°, 45.0°, 67.5°] for each observing sequence to measure the different linear polarization states (i.e. Stokes parameters I, Q and U), while a polarizing Wollaston prism beam splitter is then used to divide the light into two orthogonal polarization states. The focal plane mask (FPM) differs in size between the J and $K1$ bands, where the FPM has a radius of ∼0.09″ in the J band and a radius of ∼0.15″ in the $K1$ band. Further details about the observations and systems themselves can be found in Tables 1 and 2 in Chapter 3. Additionally information about the H-band observations can be found in Esposito et al. (2020).

All data were reduced using the GPI Data Reduction Pipeline (Perrin et al. 2014a, and references therein). To start the data reduction process, the raw data frames are retrieved and are visually inspected for quality control. For example, several data frames, typically at the beginning or end of the observing sequence, often have poor alignment of the star behind the coronagraph, and are therefore removed. Once bad data frames are removed, the raw data are then processed through the reduction pipeline, via the "Basic Polarization Sequence (From Raw Data)", to create 3-dimensional data cubes. The first two dimensions of these cubes contain the spatial information (x,y), and the third dimension contains the orthogonal polarizations. During this step, the raw data are dark subtracted and *destriped* with a Fourier filter (Ingraham et al., 2014) and bad pixel corrected. A cross-correlation algorithm is also used to match the detector with the expected positions of each lenslet's two PSFs (Draper et al., 2014) before they are assembled into the 3D cubes. The data are flat-fielded and the position of the central star is measured using fiducial satellite spots

Table 2.1: Summary of observations. The InnerRadius and OuterRadius refer to the radius in pixels used to measure the instrumental polarization behind the focal plane mask. The last column state which data frames were removed due to poor alignment of the star behind the coronagraph. [a] First presented in Crotts et al. (2021). [b] First presented in Crotts et al. (2022).

Name	Band	Date	InnerRadius	OuterRadius	Frames Removed
HD 32297	J	151206	10	13	N/A
...	K1	161118	7	11	336-339
HD 35841	J	180127	7	11	46-59
...	K1	171228	7	11	36-38, 88-91
HD 61005	J	151201	7	11	N/A
...	K1	180126	7	11	127-131
HD 106906	J[a]	160326	2	7	161
...	K1[a]	160328	2	7	203-206
HD 110058	J	180126	10	13	N/A
...	K1	170420	7	11	136-139
HD 111520	J[b]	160326	0	25	219-224
...	K1[b]	160328	10	13	248-252
HD 114082	K1	170420	7	11	173-176
HD 115600	J	180128	10	13	N/A
...	K1	180127	7	11	225-227, 273-276
HD 129590	K1	170421	7	11	125-128
HD 146897	J	160327	7	11	N/A
...	K1	180709	7	11	158-159
HD 157587	J	160326	7	11	363
...	K1	160327	7	11	N/A
HD 191089	J	170701	7	11	145-151

Figure 2.1: Example of the quadrupole noise removal from the HD 32297 J-band data. The noise is first measured in the U_ϕ data (**top**), which is then removed from the Q_ϕ data (**bottom**). The **left** figures show the initial Q_ϕ and U_ϕ data, the **middle** figures show the Q_ϕ and U_ϕ data with the quadrupole noise subtracted, and the **right** figures show the measured quadrupole noise alone.

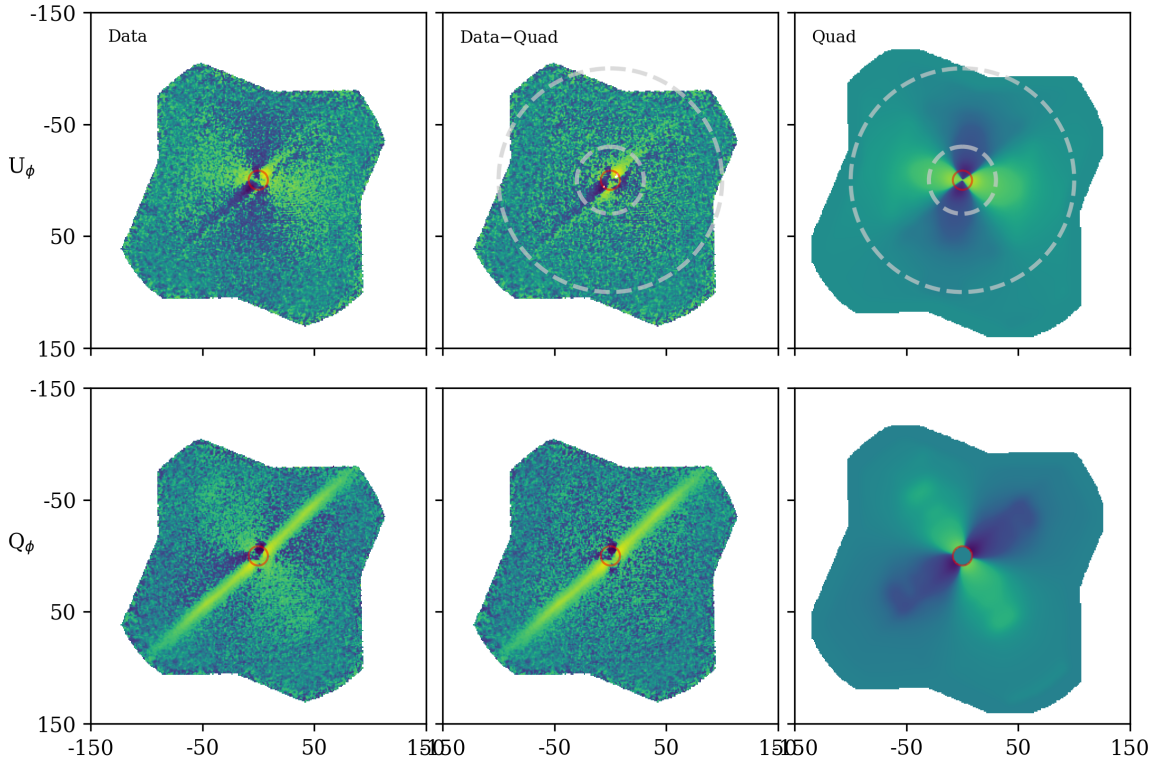

(Wang et al., 2014a) which are later used for photometric calibration. Once the raw data are processed into 3D data cubes, the data cubes are again visually inspected to ensure no bad calibration files were used. Additionally, the location of the star is double checked through searching "PSFCENTX" and "PSFCENTY" in the headers for each data cube to identify any additional frames where the star was not centered correctly behind the coronagraph. The frames that were removed for each dataset are stated in Table 2.1 under "Frames Removed".

Once the raw data are processed into data cubes and all bad frames are identified, the remaining data cubes are further reduced into a single azimuthal Stokes image using the "Basic Polarization Sequence (From podc cubes)". The cubes are accumulated, cleaned using a double differencing procedure developed specifically for GPI ADI data (Perrin et al., 2015), and then smoothed using a Gaussian kernel with a FWHM of 1 pixel. In the next step, the mean stellar polarization is subtracted from

Figure 2.2: Example transformation between the autoreduced data (**left**) and my uniformly reduced data (**right**) for the HD 157587 disk in the J band. Both data are scaled by the number in the lower left corner. The circles represent the size of the focal plane mask ($0.09''$), and the crosses represent the location of the star.

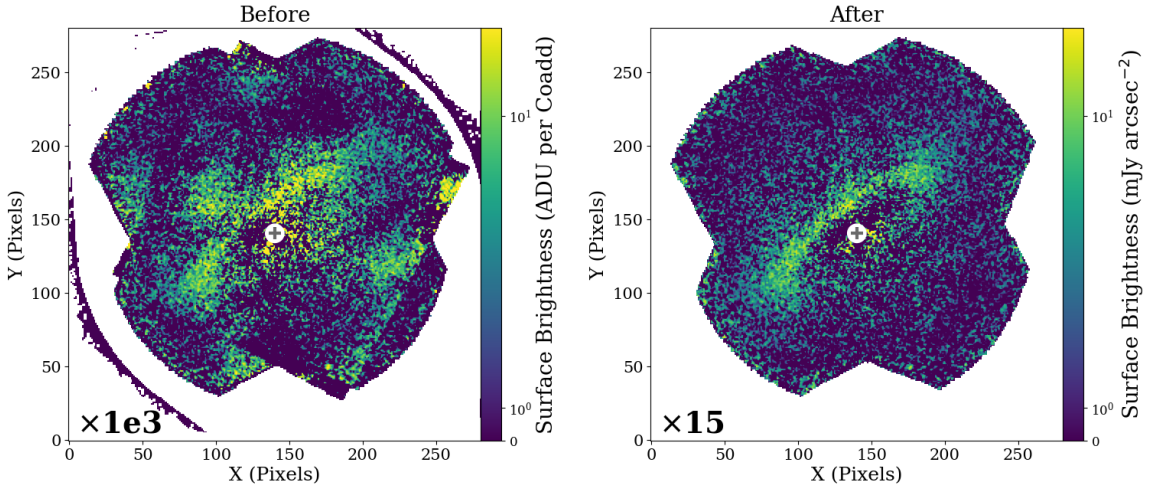

the image, which is done by measuring the polarization in an annulus near the FPM (Millar-Blanchaer et al., 2016). The default settings for the annulus in this step is an inner radius of 0 pixels and an outer radius of 25 pixels from the star, however, changing the inner and outer radius can lead to a much cleaner final image. I find that a 2-5 pixel wide annulus centered between 2 and 13 pixels from the star was the most effective at removing the mean stellar polarization. The inner and outer radius of the annulus used for each data set can be found in Table 2.1. It should be noted that the determination of the best annulus location and size was done merely by eye. Once the mean stellar polarization is removed, the image is rotated so that North is up and combined into a single cube with Stokes parameters [I,Q,U,V], where I is the total intensity component, Q and U are the linear polarization components, and V is the circular polarization component. The combined image is then transformed to azimuthal Stokes vectors Q_ϕ and U_ϕ defined as

$$\begin{aligned} Q_\phi &= -Q\cos 2\phi - U\sin 2\phi \\ U_\phi &= +Q\sin 2\phi - U\cos 2\phi \end{aligned} \tag{2.1}$$

where ϕ is the azimuthal angle between each pixel and the star measured counter-clockwise from $-\pi$ to π (Schmid et al., 2006; Millar-Blanchaer et al., 2015). As a

result, Q_ϕ contains the linearly polarized disk signal and U_ϕ (which is aligned $\pm 45°$ from Q_ϕ) should only contain noise assuming an optically thin debris disk causing single scattering. Finally, the image is converted from units of ADU per coadd to real units of Jy arcsec^{-2} using the satellite spot measurements of the stellar flux.

While the reduction process would typically stop here, I conduct one extra step, similar to the H-band data as described in Esposito et al. (2020). To summarize, I attempt to remove a quadrupole-like noise pattern that is commonly seen in GPI polarized intensity data due to imperfect subtraction of the instrumental polarization. This is done by measuring the contribution and orientation of this quadrupole pattern in U_ϕ using the function $B = B_0 I_r \sin 2(\theta + \theta_0)$, where I_r is the azimuthally averaged total intensity as a function of radius. As described in Esposito et al. (2020), the function is fit by varying the scaling factor B_0 and offset angle θ_0 to minimize the sum of the squared residuals. The best fitting function is then subtracted from the U_ϕ image, rotated by 45°, and then subtracted from the Q_ϕ image. An example of this quadrupole subtraction can be seen in Figure 2.1.

At this stage, the data have been effectively cleaned as much as possible. As an example, Figure 2.2 shows the new reduction of the HD 157587 disk in the J band compared to the initial auto-reduction, highlighting the major improvement in data quality. To quantify this improvement, I compare the signal-to-noise ratio (SNR) along the disk's major-axis for both reductions. I find the autoreduced data to have an average SNR of 1.4 along the major-axis, while in the new reduction, the average SNR increases to 2.0, signifying a ∼35-40% improvement in SNR. The final data reductions for all the disks in the J and $K1$ bands can be seen in Figure 2.3. In all cases, the noise was significantly reduced, and the disk itself was better recovered. For only one disk, HD 61005, does a high amount of noise persist in both the J and $K1$ bands. While I am unable to significantly reduce the noise in these datasets, given that they are very low signal-to-noise observations to begin with, the disk signal is still better recovered compared to the autoreduced data. I also note that the J- and $K1$-band data for the HD 106906 and HD 111520 were first presented in Crotts et al. (2021) and Crotts et al. (2022), respectively, but were still reduced in a similar manner to the rest of the sample.

Figure 2.3: Final J (**top**) and $K1$-band (**bottom**) Q_ϕ reductions. The circles represent the size of the focal plane mask in the J and $K1$ bands (0.09″ and 0.15″, respectively), and the crosses represent the location of the star. Similar to Figure 1.3 from Esposito et al. (2020), the data are scaled in units of mJy arcsec^{-2} by the numbers in the lower left corner in order to have similar brightness. Additionally, the disk surface brightness is linear from 0 to 1, and log scale from 1 to 20 mJy arcsec^{-2}. For all data, East is left and North is up.

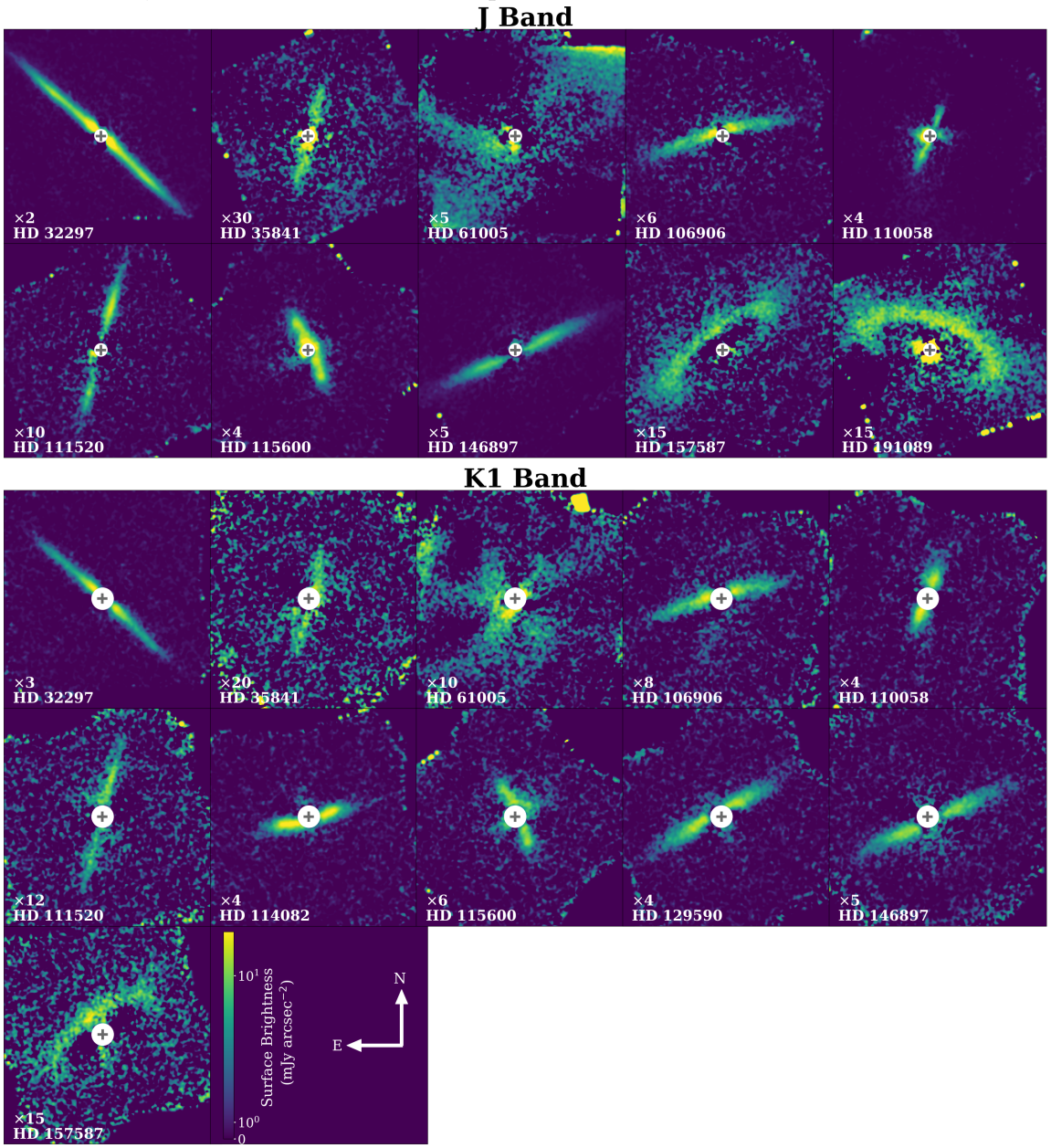

2.2 Data Archive

Now that both datasets are uniformly reduced in an optimized manner, the data can be stored publicly for future analysis and research by any member of the astronomy community. In addition to being full reductions, these data also contain important and useful details in their headers including information about the observation and observing conditions, reduction steps, parameters and calibrations files used, etc. I chose to store these data (alongside the H-band data) on the platform CANFAR, i.e. the Canadian Advanced Network for Astronomical Research. CANFAR is a consortium dedicated to serving computing and data intensive resources to members of Universities and Centers engaged in astronomical research, and can be used to store and manage data via a VOSpace. Through their storage system, CANFAR also provides the Data Publication Service which allows one to connect a Digital Object Identifier (DOI) to datasets presented in a research paper. Therefore, by storing these datasets on CANFAR, I can attach a DOI that will make the data easily and permanently searchable. Following this procedure, the data can be obtained through the following DOI[1]: https://doi.org/10.11570/24.0089. The data stored on CANFAR are categorized by filter (J, H, and $K1$) and are labelled by filter and name of the object for easy finding. A "README" file can also be found with extra information regarding citation requirements and the DRP recipe template mentioned in Section 2.1 with the listed steps. To summarize, I have provided a permanent location to store our best reductions of the polarized intensity, multiwavelength, GPI debris disk observations, alongside additional resources to help summarize the data reduction process.

2.3 Conclusions

In this chapter I discuss the data reduction steps of the GPI J and $K1$ polarized intensity observations. I ensure the best quality reductions by removing frames with poor alignment of the star behind the coronagraph, double checking the quality of the calibration files, adjusting the annulus size and location to efficiently remove the mean stellar polarization, as well as removing a quadrupole-like pattern in each final image. The data are now prepared to be uniformly analyzed, which will be described

[1]Until the DOI is activated, the data can be obtained through the following link: https://www.canfar.net/storage/list/AstroDataCitationDOI/CISTI.CANFAR/24.0089/data

in the next two chapters.

In addition to the data reduction, I am also providing a public space on CANFAR to permanently store these GPI datasets. The purpose for this is to give other members of the astronomy community the ability to easily obtain our well reduced data for future research and analysis.

Chapter 3

A Uniform Analysis of Debris Disks with GPI. An Empirical Search for Perturbations from Planets

In Chapter 2, I discuss the data reduction process for the J and $K1$ band debris disk data taken with GPI in polarized intensity. In this Chapter, I take a step beyond the work of Esposito et al. (2020) by combining the J and $K1$ data with the H band data, creating a multiwavelength GPI disk sample, to perform a uniform, empirical analysis. The goal of this study is to fully characterize the disk morphology in the NIR, and identify disks that are potentially perturbed. We choose to perform solely an empirical analysis, as radiative-transfer modelling can be computationally expensive and often not ideal for fitting asymmetric disks. Again, we focus primarily on polarized intensity observations, as they do not suffer from disk self-subtraction due to the PSF-subtraction process as is often prevalent in total intensity observations.

Through our analysis, we derive the disk geometry, surface brightness, and disk color for the disks with multiwavelength observations. As part of the disk geometry, we also fit for offsets of the disk along the major- and minor-axis to check whether or not the disk is eccentric or has an asymmetric geometry, such as from a warp. We additionally measure whether or not any surface brightness or disk color asymmetries are present. The methods for deriving these disk properties are laid out in Section 3.2, while the results for each individual disk can be found in Chapter 3.5.3. We then use these derived disk properties to categorize each disk based on similarities in asymmetries and discuss possible sources of perturbation in Section 3.3, along with discussion of broader trends found between disk and stellar properties. For reference, this work is published in the Astrophysical Journal under Crotts et al. (2024).

Table 3.1: Summary of system properties including distance, age, stellar effective temperature/mass and luminosity. Distance measurements are from Gaia Collaboration (2020), except for β Pic which is taken from Nielsen et al. (2020). T_{eff}, M_* L_* values are taken from Esposito et al. (2020), and are new measurements done for the GPIES campaign, along with two of the system ages, as described in Nielsen et al. (2019). Age References: (1) Nielsen et al. (2016), (2) Bell et al. (2015), (3) Nielsen et al. (2019), (4) Zuckerman (2019), (5) Pecaut & Mamajek (2016).

Name	distance (pc)	Age (Myr)	T_{eff} (K)	M_* ($M_\odot$)	L_* ($L_\odot$)
AU Mic	9.71 ± 0.00	23-29 (1)	3500	$0.64^{+0.03}_{-0.02}$	0.06 ± 0.03
β Pic	19.44 ± 0.05	23-29 (1)	8200	$1.73^{+0.00}_{-0.02}$	9.33 ± 3.13
CE Ant	34.10 ± 0.03	7-13 (2)	3420	$0.31^{+0.06}_{-0.06}$	0.07 ± 0.07
HD 30447	80.31 ± 0.14	38-48 (2)	6900	$1.45^{+0.00}_{-0.01}$	3.51 ± 0.72
HD 32297	129.73 ± 0.55	15-45 (3)	7700	$1.69^{+0.02}_{-0.02}$	8.12 ± 1.68
HD 35841	103.08 ± 0.14	38-48 (2)	6500	$1.30^{+0.01}_{-0.01}$	2.35 ± 0.54
HD 61005	36.45 ± 0.02	45-55 (4)	5600	$0.98^{+0.02}_{-0.07}$	0.68 ± 0.07
HD 106906	102.38 ± 0.19	12-18 (5)	6500	$2.70^{+0.12}_{-0.11}$	5.89 ± 1.15
HD 110058	130.08 ± 0.53	12-18 (5)	8000	$1.70^{+0.03}_{-0.02}$	9.33 ± 2.13
HD 111161	109.37 ± 0.25	12-18 (5)	7800	$1.72^{+0.02}_{-0.03}$	9.33 ± 1.17
HD 111520	108.05 ± 0.21	12-18 (5)	6500	$1.26^{+0.09}_{-0.07}$	2.69 ± 0.37
HD 114082	95.06 ± 0.20	12-18 (5)	7000	$1.42^{+0.08}_{-0.11}$	4.74 ± 0.56
HD 115600	109.04 ± 0.25	12-18 (5)	7000	$1.54^{+0.02}_{-0.10}$	5.27 ± 0.37
HD 117214	107.35 ± 0.25	12-18 (5)	6500	$1.47^{+0.02}_{-0.01}$	5.01 ± 0.90
HD 129590	136.32 ± 0.44	14-18 (5)	5910	$1.40^{+0.02}_{-0.01}$	3.35 ± 0.96
HD 131835	129.74 ± 0.47	14-18 (5)	8100	$1.77^{+0.05}_{-0.04}$	10.41 ± 2.21
HD 145560	121.23 ± 0.29	14-18 (5)	6500	$1.29^{+0.14}_{-0.05}$	3.47 ± 0.14
HD 146897	132.19 ± 0.41	7-13 (5)	6200	$1.28^{+0.02}_{-0.01}$	3.40 ± 0.66
HD 156623	108.33 ± 0.33	14-18 (5)	8350	$1.90^{+0.04}_{-0.05}$	13.06 ± 1.80
HD 157587	99.87 ± 0.23	165-835 (3)	6300	$1.44^{+0.01}_{-0.01}$	2.69 ± 0.23
HD 191089	50.11 ± 0.05	23-29 (1)	6400	$1.35^{+0.01}_{-0.01}$	2.54 ± 0.17
HR 4796 A	70.77 ± 0.24	7-13 (2)	9600	$2.23^{+0.04}_{-0.05}$	26.44 ± 5.48
HR 7012	28.79 ± 0.13	23-29 (1)	7700	$1.70^{+0.01}_{-0.02}$	8.13 ± 1.67

3.1 Observations

A summary of the system properties for each disk can be found in 3.1, such as the system age and stellar properties. Additionally, a summary of the observations for each disk and each band can be found in Table 3.2. Although the HD 143675 disk is included as a part of GPIES, because the disk is so radially small and close to the focal plane mask (FPM), we were unfortunately unable to determine the geometry

and therefore do not include it in this study. We direct the interested reader to Hom et al. (2020) for an analysis of both the polarized and total intensity observations, where the total intensity observations are better resolved.

While the data reduction process is already described in Chapter 2, we re-plot our final Q_ϕ reductions in the J and $K1$ bands alongside the H band. Figure 3.1 shows the debris disks with multiwavelength observations (from left to right: J, H, $K1$), and 3.2 shows the remaining 11 disks which are only observed in the H band. Using the U_ϕ data, we also create noise maps for each disk. This is under the assumption that U_ϕ contains no disk signal, as expected for an optically thin debris disk causing single scattering, however, this has not been found to be entirely the case for the H-band data (see Appendix A in Esposito et al. 2020). To create noise maps, we simply calculate the standard deviation at each radius in 1-pixel wide stellocentric annuli of the U_ϕ image. These noise maps are used to estimate the uncertainty in the surface brightness for each disk, and can also be divided from Q_ϕ to create signal-to-noise (S/N) maps. Our S/N maps can be seen in Figure 3.15 located in Section 3.5 at the end.

3.2 Empirical Analysis & Results

3.2.1 Disk Geometry

To understand the disk morphology as a whole, we first measure the geometry for each disk. For this process, we separate lower inclined disks ($i \lesssim 75°$) from higher inclined disks ($i \gtrsim 75°$), as a slightly different fitting process is required. The cut off of $\sim$75° is chosen because it is at this point that radial structure becomes significant, and the disks are therefore no longer fit well with the method used for higher inclined disks. For higher inclined disks, we fit a Gaussian profile to the surface brightness along vertical slices at multiple radial separations from the star, avoiding noisy regions close to the star. For lower inclined disks which show more radial structure, we instead fit a Gaussian profile to the surface brightness measured along radial slices to more accurately trace the disk geometry. This is done by rotating the image between, at minimum, -90° to +90° from the given PA, and taking vertical slices at each angle (see Figure 3.3 for a visual representation). Depending on how much of the disk is visible for the lower inclined disks in our sample, we rotate the image beyond -90 and +90 degrees to also trace the geometry of the back side of the disk. The FWHM and

Table 3.2: Summary of observations. Here, t_{exp} = the integration time for each frame in seconds, t_{int} = the total integration time in seconds, and ΔPA = the total parallactic angle rotation in degrees.

Name	Band	Date	t_{exp} (s)	t_{int} (s)	ΔPA (°)
AU Mic	H	140515	59.65	2624.44	166.9
β Pic	H	131212	5.82	3258.73	91.5
CE Ant	H	180405	119.29	3817.37	12.8
HD 30447	H	160922	59.65	3101.61	125.8
HD 32297	H	141218	59.65	2147.27	19.1
...	J	151206	88.74	3549.6	24.2
...	K1	161118	88.74	2839.68	19.8
HD 35841	H	160318	88.74	2484.78	3.7
...	J	180127	59.65	5726.40	19.4
...	K1	171228	88.74	4703.22	93.9
HD 61005	H	140324	59.65	2087.62	140.1
...	J	151201	59.65	4891.30	164.5
...	K1	180126	88.74	4969.44	150.8
HD 106906	H	150701	59.65	2564.79	20.3
...	J	160326	59.65	3221.10	35.2
...	K1	160328	88.74	3549.60	36.5
HD 110058	H	160319	59.65	2147.27	25.2
...	J	180126	59.65	4712.35	54.21
...	K1	170420	88.74	2484.72	31.7
HD 111161	H	180310	59.65	4533.13	38.0
HD 111520	H	160318	88.74	2839.75	28.3
...	J	160326	59.65	3519.35	39.1
...	K1	160328	88.74	3194.64	35.8
HD 114082	H	170807	59.65	2087.62	12.3
...	K1	170420	88.74	2839.68	23.7
HD 115600	H	150703	59.65	2624.44	24.0
...	J	180128	29.10	2357.10	43.4
...	K1	180127	88.74	4437.0	34.3
HD 117214	H	180311	59.65	1908.68	18.5
HD 129590	H	170809	59.65	2147.27	17.9
...	K1	170421	88.74	2395.98	44.3
HD 131835	H	150501	59.65	1908.68	74.2
HD 145560	H	180812	59.65	1670.10	17.6
HD 146897	H	160321	88.74	1774.84	28.9
...	J	160327	59.65	4533.40	45.6
...	K1	180709	88.74	4170.78	97.6
HD 156623	H	190427	88.74	2129.81	28.2

Table 3.3: Continuation of Table 3.2.

Name	Band	Date	t_{exp} (s)	t_{int} (s)	ΔPA (°)
HD 157587	H	150829	88.74	2484.78	49.9
...	J	160326	88.74	2662.20	57.7
...	K1	160327	119.29	2027.93	32.6
HD 191089	H	150901	88.74	2484.78	101.3
...	J	170701	59.65	1908.80	11.8
HR 4796 A	H	131212	29.10	640.11	2.1
HR 7012	H	180921	4.36	1117.28	19.3

Figure 3.1: Polarized intensity observations of the 12 out of 24 debris disks detected by GPI in the J, H and $K1$ bands. The circles represent the size of the FPM for each band ($\sim$0.09″, $\sim$0.12″ and $\sim$0.15″ respectively), and the crosses represent the location of the star. Similar to Figure 5 in Esposito et al. (2020), the data are scaled in units of mJy arcsec^{-2} by the numbers in the lower left corner in order to have similar brightness. Additionally, the disk surface brightness is linear from 0 to 1, and log scale from 1 to 20 mJy arcsec^{-2}. The arrows in the lower right corner represent the North and East directions.

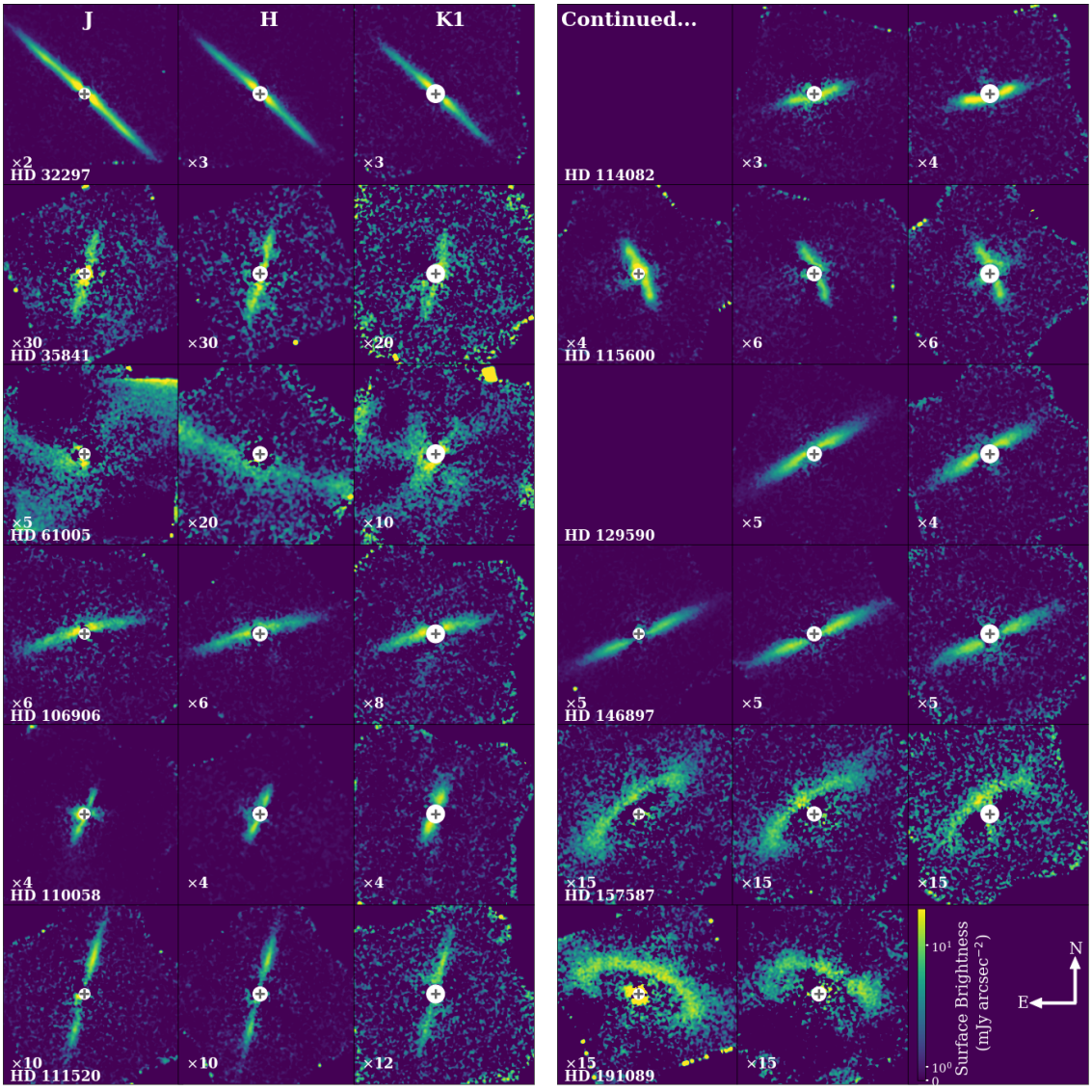

Figure 3.2: Reduced polarized intensity observations of the remaining 11 debris disks resolved by GPI in the H band. The circles represent the size of the FPM in H band ($\sim$0.12″), and the crosses represent the location of the star. The data are scaled similarly as Figure 3.1, where the disk surface brightness is linear from 0 to 1, and log scale from 1 to 20 mJy arcsec^{-2}. The arrows in the lower right corner represent the North and East directions.

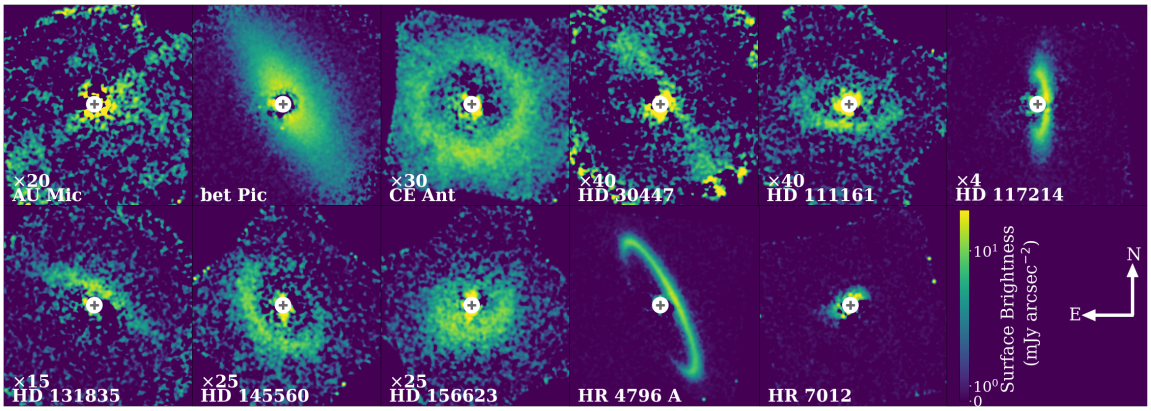

mean of the Gaussian are then extracted, giving us an estimation of the disk width, either vertically or radially depending on the disk inclination, along with either the vertical or radial offset of the disk peak surface brightness from the star. For the majority of our sample we use the H-band observations as they tend to have a higher S/N compared to the J and $K1$ band observations, however, for the cases in which the disk is higher S/N in the J or $K1$ bands (this includes HD 114082 and HD 191089), we opt to use these observations instead.

Using the derived FWHM of the disk, we estimate the vertical or radial aspect ratio by comparing the measured FWHM to R_0, where R_0 is defined as the radius of the peak dust density based on scattered light observations, and is derived from modelling the dust density profile. The R_0 values used are taken from Esposito et al. (2020), which they compiled from their own work and from the literature. To measure the aspect ratio, we calculate the weighted average of the intrinsic disk FWHM. To obtain the intrinsic FWHM, the original measured FWHM from our Gaussian fitting procedure is corrected for the instrumental PSF and any smoothing applied to the image. This is done by subtracting the FWHM of the instrumental PSF and smoothing Gaussian kernels in quadrature from the measured FWHM. Once this is done, we then simply divide R_0 from the corrected weighted average FWHM. We note that these aspect ratios are significantly higher than those reported for several of the same higher-inclined disks analyzed in Olofsson et al. (2022), including

Figure 3.3: Example of how the FWHM and vertical/radial offset are measured for high inclined disks compared to lower inclined disks. While a Gaussian function is fit to vertical slices along the disk at multiple radial separations (represented by the dotted lines in the left image), for lower inclined disks, a Gaussian function is fit to radial slices (represented by the dotted lines in the right image).

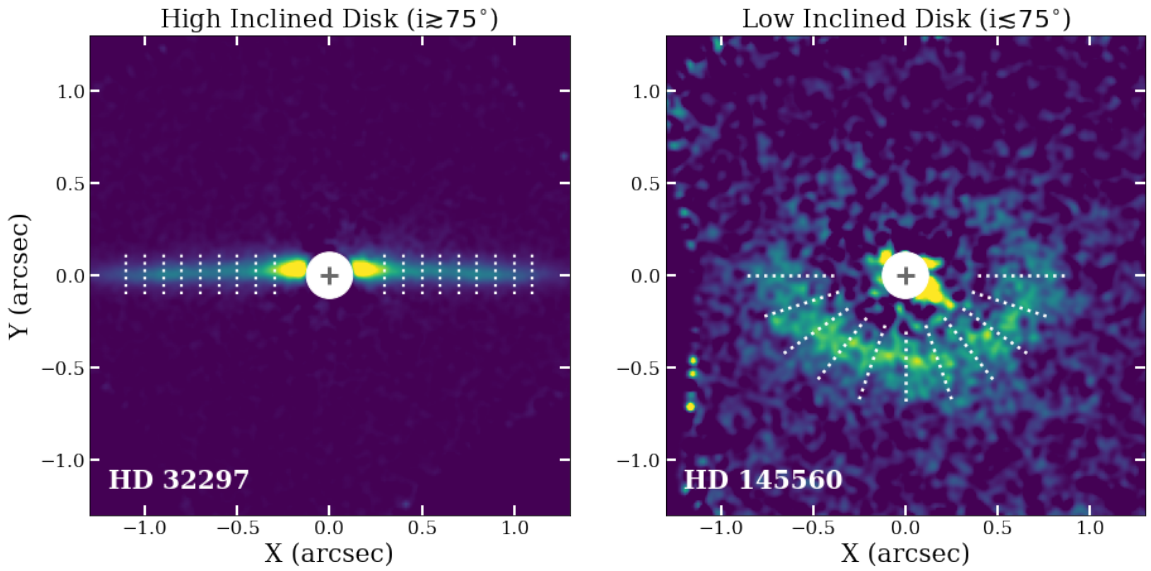

AU Mic, HD 32297, HD 61005, HD 106906, HD 115600, HD 129590 and HR 4796. This discrepancy is mainly due to the difference in measuring the vertical FWHM, where we are empirically measuring the vertical FWHM from the data, compared to Olofsson et al. (2022) who determines the vertical FWHM from disk models. By performing this measurement empirically, the vertical width becomes correlated with the disk inclination. Additionally, we are probing the contribution of the small grains in the disk halo, rather than just the planetesimal belt. We therefore do not consider these measurements as true aspect ratios, but use it mainly to compare the vertical or radial width of each disk as a function of inclination.

The aspect ratio as a function of inclination is shown in Figure 3.4. A general trend can be seen from high to low disk inclinations, where the aspect ratio increases with decreasing inclination as we move from probing the vertical aspect ratio alone to probing the radial aspect ratio. We can use this information to also identify disks with large vertical aspect ratios compared to the other disks in our sample at similar inclinations, highlighted in Figure 3.4. These four disks will be discussed further in Section 3.3.

To constrain the disk geometry, we fit a simple, geometrical inclined ring model

Figure 3.4: The aspect ratio for each disk, which is defined as the intrinsic FWHM divided by R_0 given in Esposito et al. (2020), as a function of disk inclination. The red square encapsulates the disks with anomalously high aspect ratios compared to other disks with similar inclinations.

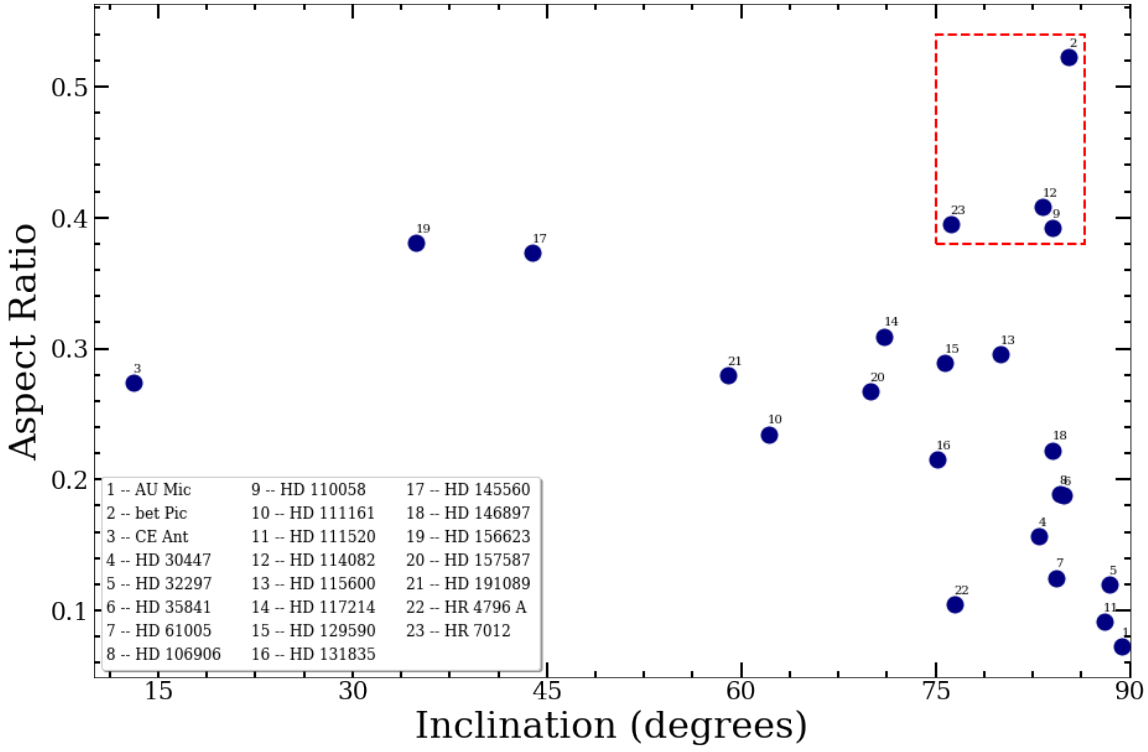

to the vertical/radial offset profile, which has also been used in previous debris disk studies (Duchêne et al., 2020; Crotts et al., 2021, 2022). This model assumes that the disk is radially narrow, although this is unlikely to be the case for many of the disks in our sample (see Section 3.3.1 for further discussion on this topic). The reasoning for choosing such a model is its simplicity, allowing us to constrain each disk's geometrical properties in an efficient and empirical manner, without having to rely on more complicated (and often degenerate) radiative-transfer modelling. Our model consists of a circular ring with radius, R_d, inclination, i, position angle, PA (defined as East of North), as well as disk offsets along the major- and minor-axes (δ_x and δ_y, respectively). For the lower inclined disks, we fit two ring models simultaneously, the first ring model being a fit to the front side of the disk, while the second ring model is the first model reflected across y-axis to fit the back side of the disk. The best fitting model is found using the MCMC code *emcee* (Foreman-Mackey et al., 2013) by deploying 200 walkers in our defined parameter space over 2000 iterations.

The results for these models can be found in Table 3.4 and the vertical/radial offsets with the best fitting ring models for each disk can be found in Figure 3.5. Additionally, the best fitting models overlaid on the images of each disk can be found in Figure 3.16 located in Section 3.5. We note that in Figure 3.5, each image is rotated by the measured disk $PA - 90°$ so that the major-axis of the disk is horizontal in the image when measuring the vertical/radial offset profile. For simplicity, in this new reference frame, we refer to the disk emission left of the star as the **East** side/extension, and refer to the disk emission right of the star as the **West** side/extension. This reference frame and terminology will also be used when measuring the surface brightness, as well as for measuring asymmetries in the surface brightness and disk color. See Table 3.8, located in Section 3.5, for information regarding the degrees of rotation and change in cardinal directions for each disk into the new reference frame.

While we fit for an offset along the minor-axis (δ_y) we do not consider it in our results for the higher inclined disks in our sample, as we find that with this method, δ_y is strongly correlated with other disk properties such as the inclination, vertical width and radial width. In terms of lower-inclined disks, because we are able to fit both the front and back sides of the disk, measurements of δ_y are more robust, and therefore can be useful to determine eccentricity. While we do not find these same correlations significantly for δ_x, it is important to take into account that δ_x can be difficult to properly constrain for radially broad disks, as well as for low S/N observations. We also note that a disk offset using this method does not necessarily mean that the disk

is eccentric, but can also be the result of other asymmetries in the disk geometry, such as a warp. The uncertainties for both the δ_x and δ_y offsets in Table 3.4 include uncertainties in the location of the star for GPI, which has been found to be ∼0.05 pixels or 0.7 mas (Wang et al., 2014a).

3.2.2 Surface Brightness

Once the disk vertical or radial offset and FWHM are measured, we can use these values to measure the surface brightness as a function of stellar separation, as well as measure any brightness asymmetries present between the East and West extension of each disk. The East and West extensions are compared specifically rather than between the front and back side of the disk as brightness asymmetries between the front and back sides are due to preferential forward or backward scattering of dust grains, rather than inherent asymmetries such as an eccentric disk.

We first measure the surface brightness along each disk for each band. This is done by first rotating the images by their derived PA values (found in Table 3.4) minus 90°, followed by binning the image into 2×2 pixel bins in order to diminish any correlation between pixels. The vertical/radial offset values are then used to define the location of the peak surface brightness along the disk, where the surface brightness is averaged along several pixels centered around the peak surface brightness location. For the lower inclined disks, the image is rotated between the same angles from the measured PA as done when measuring the vertical/radial offset, followed by averaging the surface brightness around the peak surface brightness location. The resulting surface brightness profiles can be found in Figure 3.6.

To measure the brightness asymmetry between the East and West extensions, we place apertures at similar separations from the star on either side of each disk. For higher inclined disks, we place a single rectangular aperture on the East and West extensions of the disk, while for lower inclined disks we place two to three square apertures covering from the front of the disk to the disk ansae on either side. In all cases, the height of the aperture is determined by the measured average FWHM of the disk, while the length/placement of the rectangular apertures are determined by the S/N of the disk (i.e. the apertures are placed where the S/N is the highest, again, at a similar separation from the star on either side of the disk). Once the aperture(s) are determined and placed, we then average the flux over the aperture(s) for both our image and uncertainty maps in each band to determine 1σ uncertainties. The average

Figure 3.5: The vertical or radial offset from the star for each disk as a function of separation from the star, represented by the dark blue data points. Each disk is rotated by its measured $PA - 90°$; therefore negative separations define the East side of the disk, while positive separations define the West side of the disk. Orange curves represent the best fitting narrow, inclined ring.

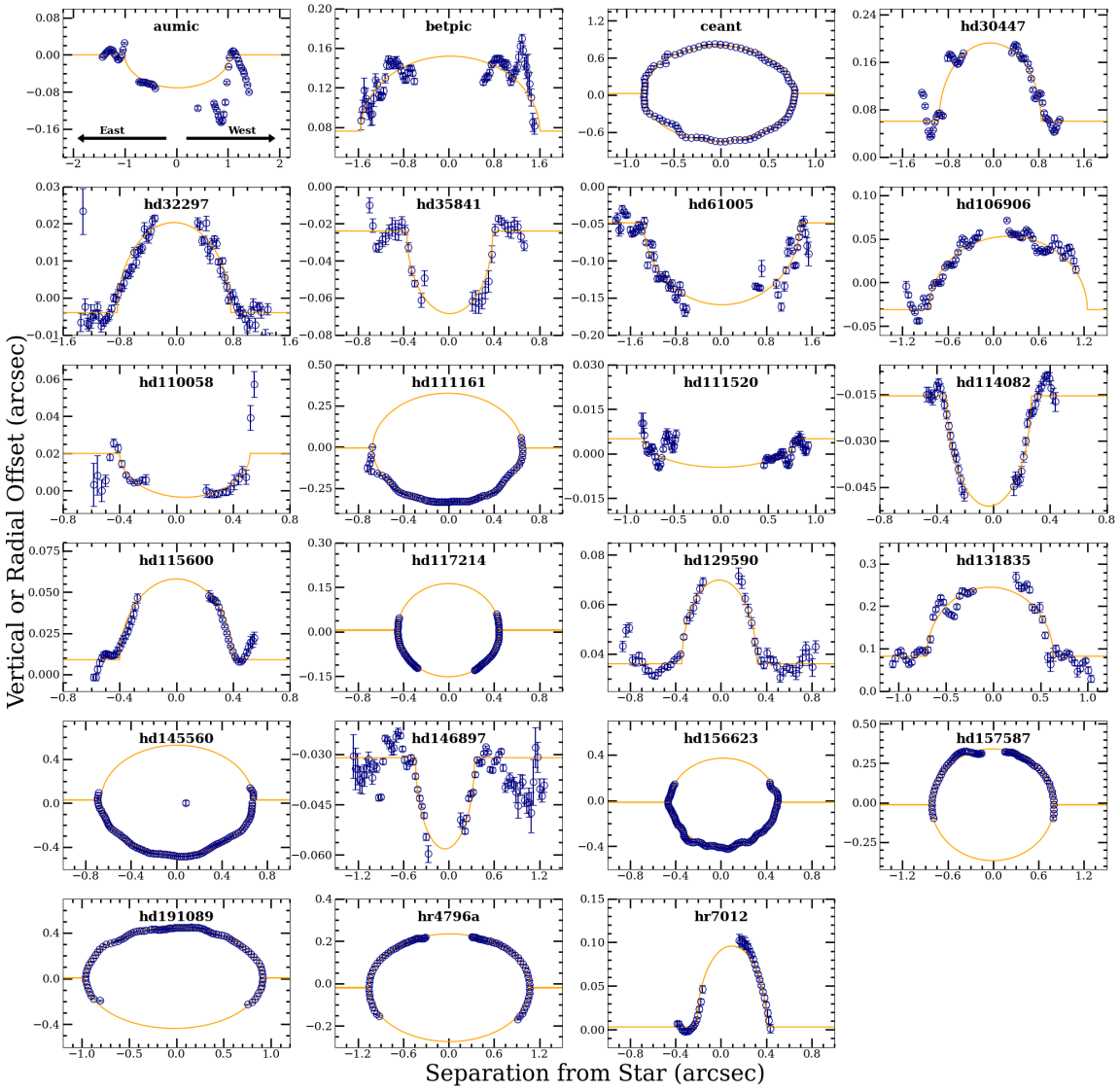

Table 3.4: Parameters for best fitting inclined ring model using H-band data.

Name	R_d (AU)	δ_x (AU)	δ_y (AU)	i (°)	PA (°)
AU Mic	$9.91^{+0.01}_{-0.01}$	$0.20^{+0.02}_{-0.02}$	$-0.02^{+0.02}_{-0.02}$	$86.00^{+0.01}_{-0.01}$	$126.68^{+0.01}_{-0.01}$
β Pic	$27.06^{+1.18}_{-0.34}$	$0.26^{+0.83}_{-0.32}$	$1.82^{+0.05}_{-0.07}$	$88.90^{+0.09}_{-0.10}$	$32.24^{+0.04}_{-0.10}$
CE Ant	$27.13^{+0.01}_{-0.01}$	$-0.86^{+0.04}_{-0.04}$	$0.86^{+0.04}_{-0.04}$	$15.10^{+0.95}_{-1.05}$	$91.02^{+0.20}_{-0.19}$
HD 30447	$75.43^{+0.68}_{-0.72}$	$-6.53^{+0.23}_{-0.36}$	$2.92^{+0.19}_{-0.19}$	$81.47^{+0.05}_{-0.05}$	$33.56^{+0.39}_{-0.01}$
HD 32297	$105.85^{+1.62}_{-1.06}$	$-4.58^{+0.90}_{-0.95}$	$-0.58^{+0.13}_{-0.13}$	$88.26^{+0.04}_{-0.04}$	$47.63^{+0.02}_{-0.01}$
HD 35841	$39.12^{+0.36}_{-0.28}$	$1.05^{+0.33}_{-0.36}$	$-2.49^{+0.13}_{-0.13}$	$83.27^{+0.20}_{-0.24}$	$167.47^{+0.05}_{-0.05}$
HD 61005	$50.21^{+0.17}_{-0.17}$	$0.68^{+0.19}_{-0.38}$	$-1.79^{+0.07}_{-0.06}$	$85.41^{+0.06}_{-0.06}$	$70.80^{+0.01}_{-0.12}$
HD 106906	$107.98^{+0.69}_{-0.79}$	$20.67^{+1.10}_{-1.10}$	$-3.20^{+0.20}_{-0.09}$	$85.34^{+0.05}_{-0.06}$	$104.00^{+0.03}_{-0.01}$
HD 110058	$59.56^{+12.47}_{-0.77}$	$8.19^{+1.01}_{-13.30}$	$2.54^{+1.25}_{-0.23}$	$87.06^{+0.23}_{-0.19}$	$158.55^{+0.11}_{-1.00}$
HD 111161	$72.48^{+0.08}_{-0.09}$	$-1.44^{+0.16}_{-0.16}$	$-0.66^{+0.09}_{-0.09}$	$59.78^{+0.08}_{-0.06}$	$83.29^{+0.04}_{-0.08}$
HD 111520	$91.42^{+13.80}_{-10.1}$	$-2.24^{+13.38}_{-10.18}$	$-1.80^{+0.39}_{-0.34}$	$89.45^{+0.27}_{-0.27}$	$165.66^{+0.11}_{-0.13}$
HD 114082	$28.50^{+1.40}_{-0.19}$	$-2.95^{+0.20}_{-0.22}$	$-1.48^{+0.10}_{-0.16}$	$83.32^{+0.54}_{-0.20}$	$105.01^{+0.05}_{-0.04}$
HD 115600	$44.02^{+7.36}_{-7.32}$	$-0.04^{+7.19}_{-7.22}$	$-1.01^{+2.17}_{-0.17}$	$82.97^{+1.32}_{-1.30}$	$24.20^{+0.01}_{-0.19}$
HD 117214	$42.77^{+0.09}_{-0.10}$	$-0.19^{+0.18}_{-0.13}$	$0.41^{+0.20}_{-0.23}$	$69.57^{+0.46}_{-0.34}$	$180.51^{+0.15}_{-0.18}$
HD 129590	$45.50^{+0.48}_{-1.08}$	$-1.89^{+0.51}_{-0.90}$	$4.96^{+0.15}_{-0.14}$	$84.11^{+0.28}_{-0.26}$	$120.28^{+0.04}_{-0.03}$
HD 131835	$89.62^{+0.81}_{-0.80}$	$-4.60^{+0.78}_{-0.84}$	$11.01^{+0.22}_{-0.22}$	$75.94^{+0.23}_{-0.23}$	$60.81^{+0.02}_{-0.18}$
HD 145560	$81.23^{+0.06}_{-0.05}$	$0.86^{+0.13}_{-0.12}$	$3.33^{+0.13}_{-0.12}$	$41.91^{+0.49}_{-0.09}$	$39.51^{+0.01}_{-0.03}$
HD 146897	$51.84^{+0.19}_{-0.78}$	$-6.33^{+0.85}_{-0.27}$	$-4.08^{+0.11}_{-0.12}$	$85.99^{+0.01}_{-0.01}$	$114.62^{+0.02}_{-.01}$
HD 156623	$52.56^{+0.69}_{-0.25}$	$2.10^{+0.17}_{-0.55}$	$1.68^{+0.09}_{-0.09}$	$34.70^{+0.46}_{-0.96}$	$102.86^{+0.03}_{-0.49}$
HD 157587	$81.24^{+0.05}_{-0.04}$	$-0.65^{+0.12}_{-0.11}$	$1.32^{+0.19}_{-0.17}$	$64.02^{+0.04}_{-0.02}$	$127.71^{+0.10}_{-0.08}$
HD 191089	$46.96^{+0.01}_{-0.03}$	$-1.20^{+0.05}_{-0.09}$	$0.35^{+0.09}_{-0.09}$	$61.85^{+0.09}_{-0.08}$	$71.40^{+0.10}_{-0.07}$
HR 4796 A	$77.71^{+0.05}_{-0.04}$	$0.58^{+0.10}_{-0.09}$	$-1.56^{+0.09}_{-0.09}$	$76.15^{+0.06}_{-0.07}$	$26.43^{+0.03}_{-0.03}$
HR 7012	$8.77^{+0.08}_{-0.05}$	$2.76^{+0.07}_{-0.14}$	$0.08^{+0.04}_{-0.04}$	$72.42^{+0.35}_{-0.16}$	$113.80^{+0.23}_{-0.19}$

surface brightness can then be compared between the East and West extensions to determine whether or not a surface brightness asymmetry is present. The surface brightness asymmetry for each disk can be found in Figure 3.7, which is defined as the brighter extension divided by the dimmer extension. We find 16/23 disks have a significant brightness asymmetry (i.e. by 3σ in at least one band), which is well over half the disks in our sample.

3.2.3 Disk Color

For the disks in our sample that have multiwavelength observations, we can also measure the disk color between bands. Given that the scattering properties of dust grains determines the disk color, these color measurements can give us information about the dust grain properties in the disk such as dust composition, minimum grain size, and porosity. While it is difficult to untangle these dust grain properties from the disk color alone, we can still use these results to compare the disk color of our sample in NIR wavelengths to look for trends, as well as compare the disk color between the East and West extensions to determine if any asymmetries are present.

To measure the disk color, we start with the same process as measuring the surface brightness asymmetry, where the flux on either side of the disk is averaged over the same apertures used previously. This averaged flux is then converted to magnitudes and compared between a pair of bands. Finally, the difference in stellar magnitude between the same pair of bands is measured and subtracted from the difference in magnitude of the disk (i.e. J-$H = \Delta\text{mag}(J_{disk} - H_{disk}) - \Delta\text{mag}(J_{star} - H_{star})$). This is done to eliminate the bias introduced by the color of the star. The average disk color (averaged across the whole disk) can be found in the top plot of Figure 3.8. In this case, a negative value indicates a blue disk color, meaning that the dust grains scatter more efficiently at shorter wavelengths, while a positive value indicates a red disk color, meaning that the dust grains scatter more efficiently at longer wavelengths. Lastly, a 0 value indicates a grey or neutral disk color, meaning that the scattering efficiency has no preference between short and long wavelengths, and can be the result of a large minimum dust grain size (on the order of a couple of microns or greater; Boccaletti et al. 2003).

In addition to the average disk color, we also measure the difference in color between the East and West extensions. The lower plot of Figure 3.8 shows the absolute value of the difference in disk color between the East and West extension. Here, a

Figure 3.6: Disk surface brightness as a function of separation from the star in all three bands. Again, the disk is rotated by measured $PA - 90°$ so that negative separations define the East side of the disk, while positive separations define the West side of the disk.

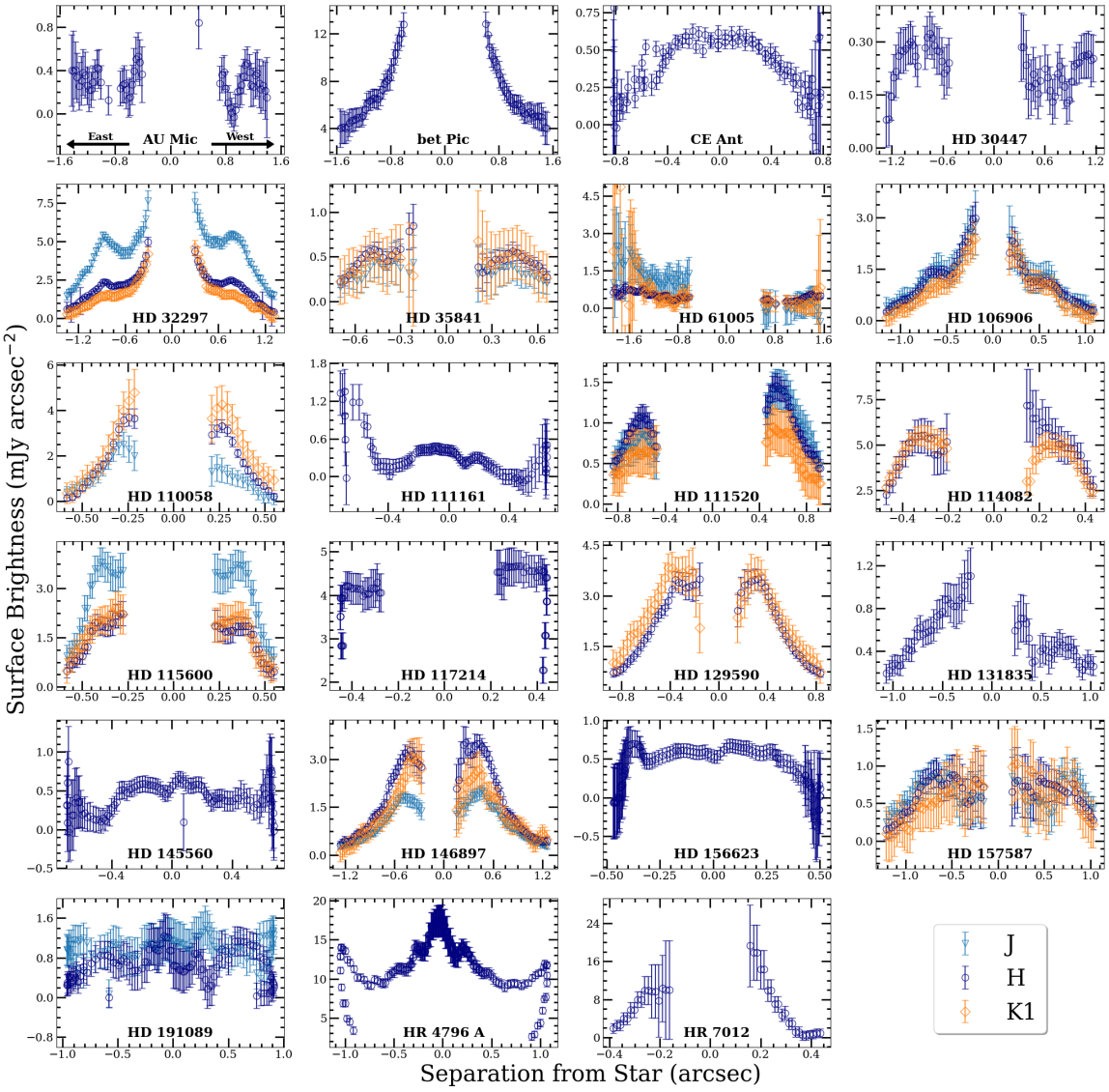

Figure 3.7: Brightness asymmetry between the East and West extensions for each disk in all three wavelengths. Values of 1 represent no brightness asymmetry. Red data points represent significant asymmetry of $\geq 3\sigma$.

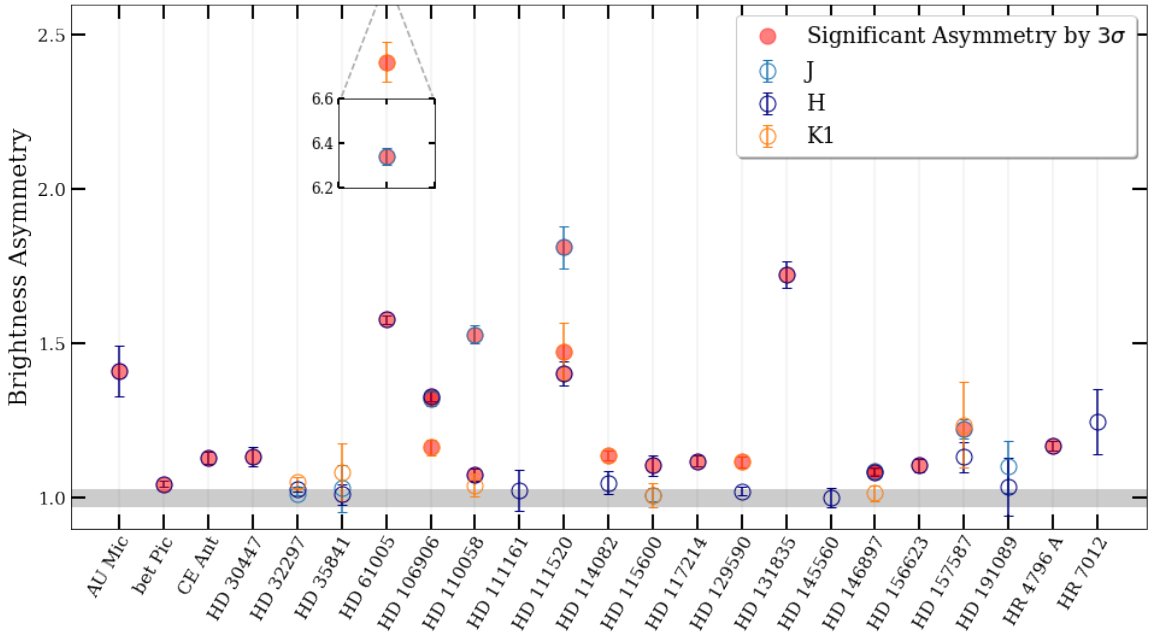

value of 0 means that no asymmetry is present. We find that 3/12 disks have significant color asymmetries of 3σ or greater in at least one band (HD 61005, HD 110058 and HD 157587), while 2 additional disks have color asymmetries with a significance between 2σ and 3σ (HD 111520 and HD 114082). In the case of an axisymmetric disk with a uniform distribution of dust grains, we would expect no difference in disk color between the East and West extensions. Therefore, an asymmetry in the disk color may be the result of an asymmetric distribution of dust grains. For example, a bluer East extension may suggest that a population of small dust grains have been released or redistributed to this area of the disk. Such an event could occur due to recent collisions in the disk or possibly an interaction with the interstellar medium (ISM; Debes et al. 2009).

3.3 Discussion

For a discussion of results for each specific disk system, along with comparison to the literature, we refer the reader to Section 3.5.3. Here we discuss the limitations of our model, as well as broader trends found in our sample.

Figure 3.8: **Top:** Average disk color for each disk, between all three wavelengths. Disks with a negative value have a blue color, while disks with a positive value have a red color and disks close to zero have a neutral disk color (shown by horizontal grey line). **Bottom:** Disk color asymmetry between all three wavelengths, measured by taking the absolute value of the East disk color subtracted from the West disk color. Values of 0 represent no disk color present. Red data points represent significant asymmetry by $\geq 3\sigma$.

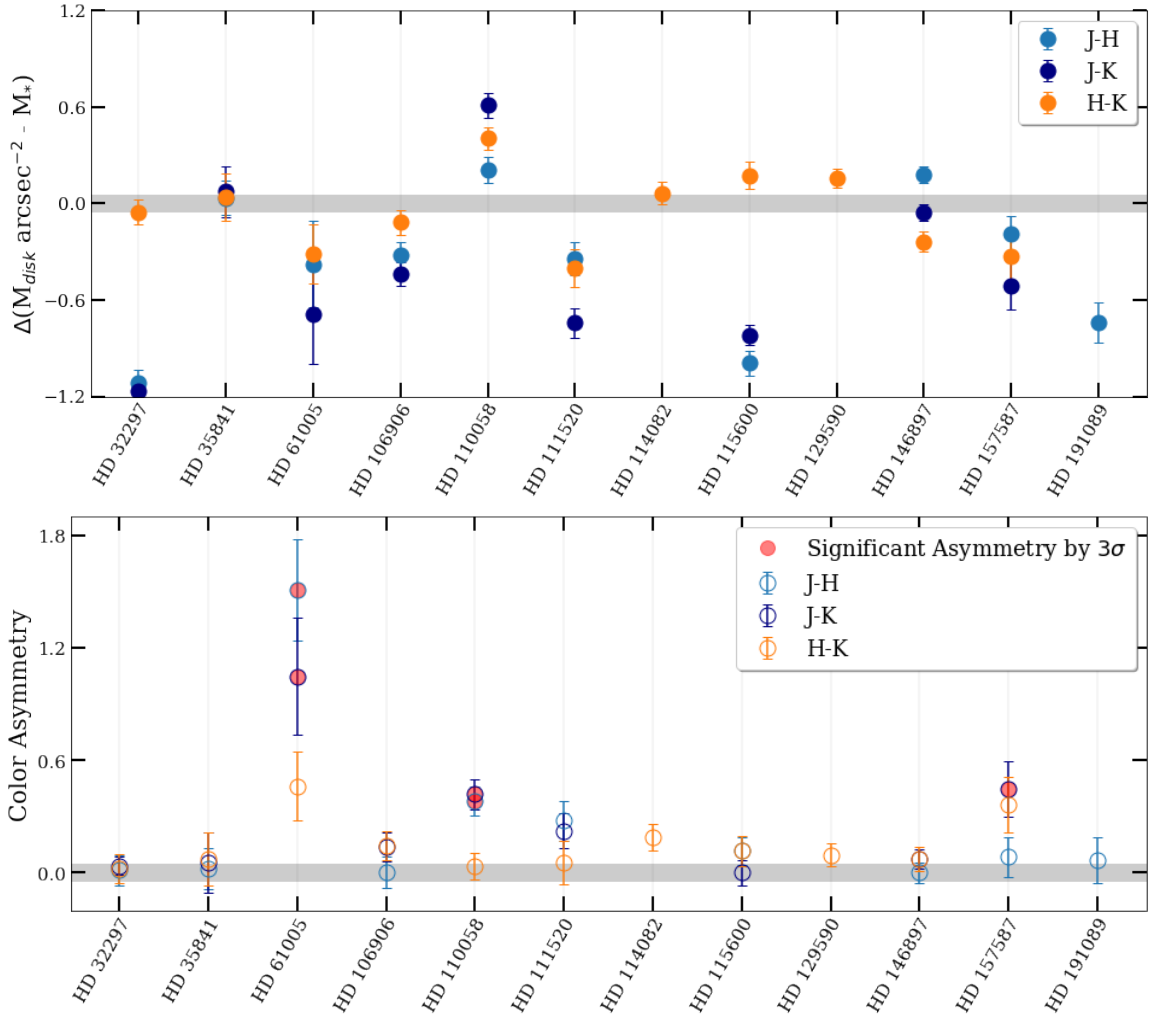

3.3.1 Ring Model Limitations

While our ring model for fitting the vertical/radial offset profiles is simplistic and allows us to efficiently derive geometrical properties for our large sample of disks, this simplicity comes with some caveats and limitations.

For one, our ring model assumes a radially narrow ring, which is likely not the case for many of the disks in our sample. This caveat may lead to poor fits, such as for β Pic, and may also have led to exaggerated offsets along the major-axis in some cases. For radially narrow disks, such as HR 4796 A, measurements of δ_x are more robust. As mentioned in Section 3.2.1, our simplistic model also has an effect on the measured offset along the minor-axis, or δ_y, where δ_y tends to be exaggerated for disks with higher inclinations ($\gtrsim$75°) as we are only fitting the front side of the disk. This influenced our decision to not take into account δ_y for the higher inclined disks in our discussion of disk morphologies, as it is difficult to untangle whether these offsets are real, or simply an effect of our chosen model and other properties of the disk.

The S/N of the observations should also be taken into account, as low S/N observations may also lead to poor fits of our ring model, creating small offsets that may not be real, such as the case with AU Mic. We do find that the several disks with the largest δ_x measurements are higher S/N observations which supports the conclusion that these disks are indeed either eccentric or harbour another geometrical asymmetry, such as a warp. However, future followup for the disks with low S/N observations will be needed to confirm our results.

In summary, our simple ring model is most effective for radially narrow disks, and for lower inclination disks where we can fit both the front and back side of the disk. Even in the case of higher inclined disks, and for most radially broad disks in our sample, this method is still successful in confirming inclination, PA, and disk radius, while δ_x measurements are also still useful for determining possible asymmetric geometries that may not be fully captured by more complex modelling, especially when taken into consideration with other factors such as surface brightness asymmetries.

3.3.2 Trends in Brightness Asymmetry

Our large sample size allows us to look at overall trends that may have implications on debris disk properties and evolution. Here, we look at trends seen in the measured brightness asymmetry derived in Section 3.2.2.

Comparing the average brightness asymmetry (brighter side/dimmer side) between all disks, three disks have significant brightness asymmetries over 1.5 (HD 61005, HD 111520, and HD 131835), two disks have significant brightness asymmetries between 1.2 and 1.5 (AU Mic and HD 106906), six disks have significant brightness asymmetries between 1.1 and 1.2, and six disks have significant brightness asymmetries <1.1. The majority of disks have brightness asymmetries where the brighter side is <1.2 times brighter than the dimmer side, while a small handful of disks have particularly large brightness asymmetries >1.2. Of the disks with the largest brightness asymmetries, HD 106906 is the only disk that has strong evidence of planet induced eccentricity (e.g. Nesvold et al. 2017; Crotts et al. 2021). It is unclear if the other three disks are eccentric, although all three have complex morphologies (i.e. multiple rings, clumps, warps, and radial asymmetries) suggesting that they are being actively perturbed by some mechanism.

When comparing the average brightness asymmetry between filters for disks with multiwavelength observations, we find that the average asymmetry is 1.75±0.04 in the J band, 1.16±0.03 in the H band, and 1.16±0.05 in the $K1$ band. Excluding HD 61005, which is an outlier in the J and $K1$ bands, changes these values to 1.24±0.04, 1.12±0.03 and 1.03±0.05 respectively. In both cases, the J band has a significantly higher brightness asymmetry on average than the H and $K1$ bands. When excluding HD 61005, the $K1$ band has the lowest brightness asymmetry on average. These results suggest that the brightness asymmetry is strongest in the smallest dust grains and decreases with increasing wavelength/particle size. This result aligns with trends seen between short and long wavelength observations, where disks appear to be more asymmetric at optical/NIR wavelengths and more symmetric at sub-mm/mm wavelengths.

3.3.3 Effects of Stellar Age & Temperature

In Section 3.2 we mainly focused on what our analysis showed for each individual disk, however, with such a uniform analysis on a large sample of disks, we can also use our results to look for larger scale trends. In this Section, we focus on debris disk properties, such as asymmetries and disk color, as a function of stellar temperature and age, to see if there are any correlations that may inform us about debris disk environments and evolution.

Figure 3.9: **Top:** Brightness asymmetry vs. stellar age. **Bottom:** Brightness asymmetry vs. stellar temperature.

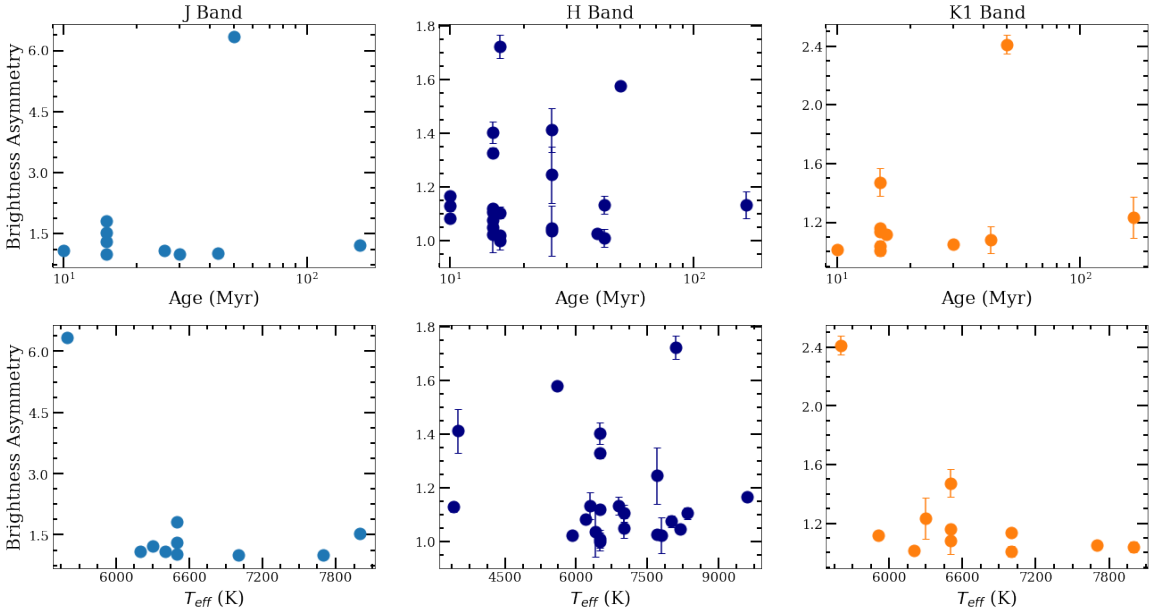

Brightness and Color Asymmetry

In Figure 3.9, we plot the measured brightness asymmetry in each band versus the stellar age and temperature. From Figure 3.9, there does not appear to be a significant trend between the degree of brightness asymmetry with either the stellar age or temperature. While at first glance it may appear as if there is a tentative trend between brightness asymmetry and stellar temperature in the J and $K1$ bands, this is simply due to our small sample size of observations in these bands along with one outlier (HD 61005).

Figure 3.10 shows the disk color asymmetry plotted vs. stellar age and temperature. Similar to the brightness asymmetry, no strong trends are seen between disks with a color asymmetry and the age of the system or stellar temperature. This result, along with the brightness asymmetry, suggests that asymmetric disks can be present regardless of the system's age or stellar temperature, although, it should be kept in mind that the average age of our sample is fairly young (less than 100 Myr). Again, it is important to note our small sample size for measured disk colors given the small sample of disks with J- and $K1$-band observations, therefore these results may not show the entire picture.

Figure 3.10: **Top:** Disk color asymmetry vs. stellar age. **Bottom:** Disk color asymmetry vs. stellar temperature.

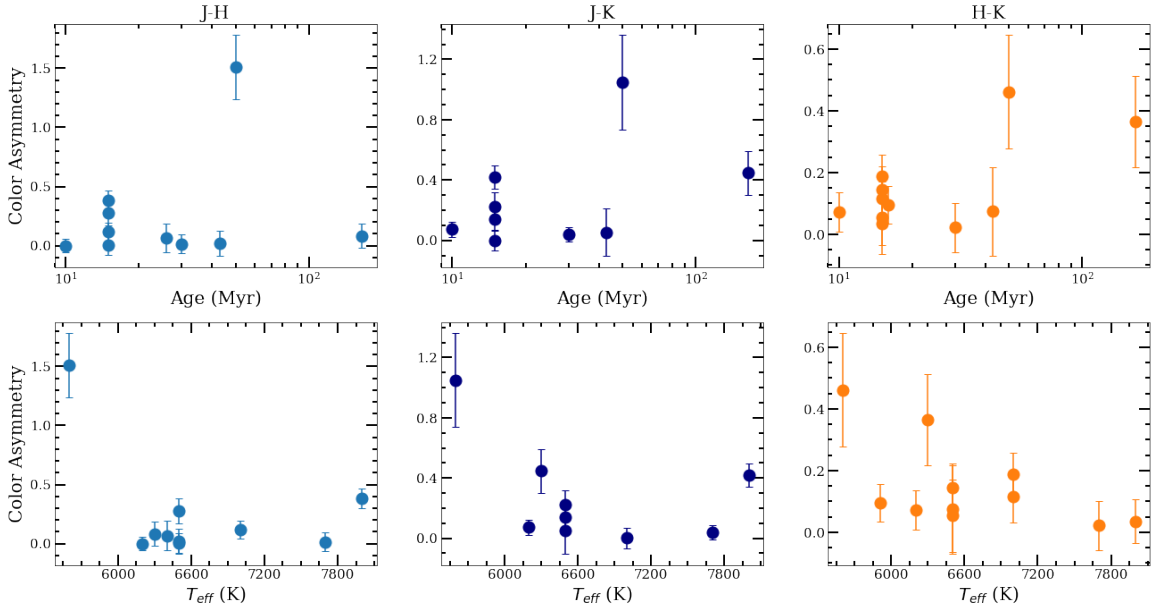

Average Disk Color

In the previous Section, we compare the brightness asymmetry and disk color asymmetry with stellar age and temperature, but we can also compare the disk color itself with these two parameters. As the disk color is the result of dust grain properties in the disk, as described in Section 3.2.3, trends between the disk color and the stellar age or temperature may be informative about the evolution of dust grains in these systems.

Figure 3.11 (top) shows, similar to the disk asymmetries, no significant trends between disk color and stellar age, demonstrating once again that age of the system does not have a drastic effect on the properties of debris disks in our sample. This is not the case with respect to the stellar temperature. A trend is suggested in the bottom plot of Figure 3.11, strongest in H-$K1$, where as we transition from cooler to hotter stellar temperatures, the disk color becomes increasingly grey/red. Calculating the strength of the correlation between the H-$K1$ color with temperature, we find a Pearson correlation coefficient of 0.6 with a p-value of 0.05, meaning that the correlation is significant at the 2σ (95%) confidence level. Similar trends have been seen in other color studies, such as with HST (Ren et al., 2023). Such a trend is also expected; as the stellar temperature increases, so does the blow-out size of

the system, i.e. the dust grain size where the force of radiation pressure is equal to the force of gravity. Because larger dust grains are more efficient at scattering at longer wavelengths compared to small dust grains, this leads to a more red disk color. Additionally, dust grains on the order of several microns or larger can exhibit a grey color, while disks with a larger population of small dust grains will tend toward a blue color.

While the trend between disk color and stellar temperature is strongest in H-$K1$, this trend weakens in J-H and J-$K1$. However, this may be due to several disks that break this trend. The two most notable disks are HD 32297 and HD 115600, both of which are around hotter stars (7700 K and 7000 K), but have exceptionally strong blue colors in J-H and J-$K1$. In both cases, the disk color becomes significantly more grey or red in H-$K1$, making them more inline with the overall trend. The strong blue color seen at short wavelengths for these two disks suggests that a larger population of small dust grains is present than would be expected for a debris disk orbiting a star of temperature >7000 K. One explanation is that these disks may have recently undergone a large/violent collision, producing dust grains smaller than the blow-out size for which radiation pressure has not had enough time to blow out these small grains.

However, a recent large collision may not even be necessary, as studies have shown that bright debris disks ($L_{disk}/L_* > 10^{-3}$) around F and A spectral-type stars (as for HD 32297 and HD 115600), with high collisional activity, can naturally produce large amounts of sub-micron sized dust grains that will leave a detectable signature (Thebault & Kral, 2019). Thebault & Kral (2019) show that the halo for these disks can contribute up to ∼50% to the total disk flux at short wavelengths while decreasing towards longer wavelengths. Additionally, small unbound grains can turn the disk color from red to blue. This may explain the strong blue colors in J-H and J-$K1$, which then becomes significantly less blue in H-$K1$. We note that the enhanced blue color is not observed for all bright debris disks around hot stars (i.e., HD 110058). In fact, the HD 110058 debris disk, which has the hottest host star for a disk with multiwavelength observations, is the only disk in our sample that is strongly red across all three wavelengths. Either another factor is affecting the color of this disk (such as composition), or the sub-micron sized grains have been successfully blown out of the system. Either way, these examples show how the disk color is affected by the stellar temperature, and can also be used to help understand the mechanics of a collisional cascade in certain disks.

Figure 3.11: **Top:** Disk color vs. Stellar Age. **Bottom:** Disk color vs. Stellar Temperature.

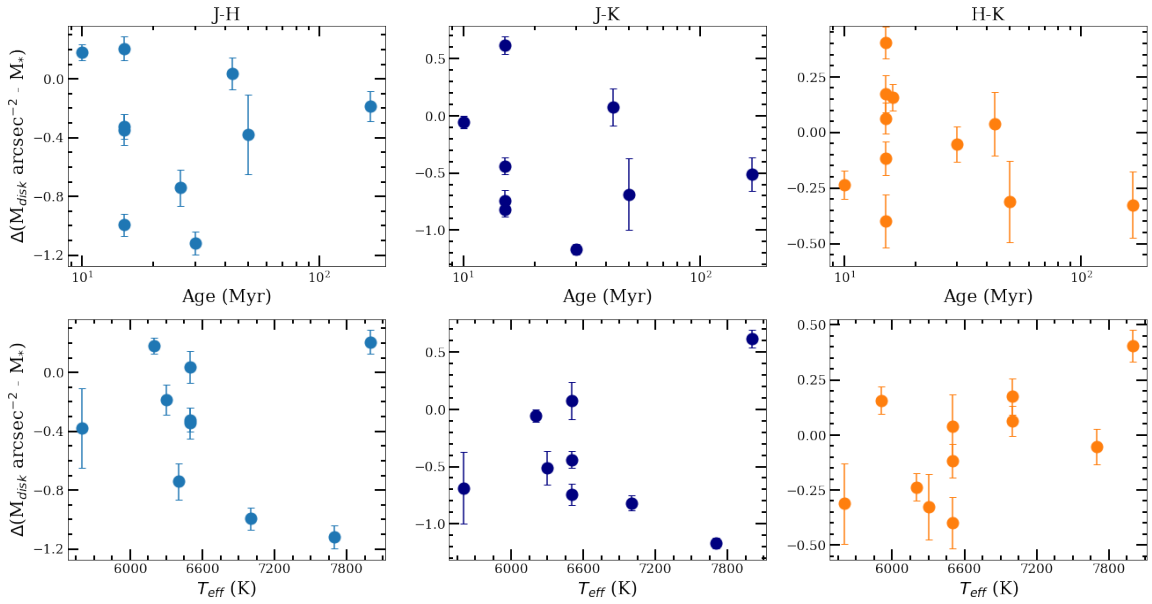

3.3.4 Disks with Large Aspect Ratios

In Section 3.2.1, we measured the vertical FWHM (or radial FWHM depending on the inclination) using our Gaussian fitting procedure and used the average FWHM to roughly estimate the aspect ratio. Plotting these aspect ratios vs. inclination showed several debris disks that had a larger vertical aspect ratio compared to other disks of similar inclination (highlighted by the red square in Figure 3.4). To understand the underlying reason for this discrepancy, we compare the aspect ratio with other disk and system parameters.

In Figure 3.12, we show the aspect ratio plotted vs. the stellar temperature for disks with $i > 70°$, where the color of each data point represents the reference radius, R_0, for each disk. The four disks that have particularly high aspect ratios compared to other disks with similar inclinations are highlighted by the red dashed square box, β Pic, HD 110058, HD 114082 and HR 7012. One reason these disks may have a high aspect ratio is the combination of their inclinations and the way we measure the aspect ratio, where there may be some back scattering from the far side of the disk that is contributing the vertical width. However, there are two things noticeable in Figure 3.12, with respect with the four highlighted disks, that are not related to disk inclination. One, these disks are around relatively hotter stars (7700 K to 8200 K) compared to other disks in our sample with higher inclinations, and two, these

four disks are more radially compact in terms of R_0), with $R_0 < 40$ au. Additionally, three out of these four disks (β Pic, HD 110058 and HR 7012) also have detectable amounts of CO (Dent et al., 2014; Hales et al., 2022; Schneiderman et al., 2021). HD 114082 has no gas detection, with only an upper limit on the CO mass of $< 5 \times 10^{-6}$ (Kral et al., 2020).

The fact that these four disks have multiple factors in common can help us understand what is causing these disk to have a large vertical aspect ratio. While all four disks are around hotter stars, and three out of four have detectable amounts of CO, there are two other disks that also meet this criteria, HD 32297 and HD 131835 (stellar temp = 7700 K and 8100 K), but do not have a high vertical aspect ratio. This suggests that the stellar temperature and the existence of a gas disk, either together or individually, are not the root cause of a disk becoming vertically thick. In fact, Kral et al. (2020) found that gas in debris disks should have the opposite effect, making the disk more vertically thin due to the settling of small dust grains. Looking more closely at HD 32297 and HD 131835, one thing that distinguishes these two disks from the other four is that they are both more radially extended in terms of R_0 ($R_0 = 98.4$ au and 107.7 au). In addition to this, AU Mic, which has a smaller R_0 of 30.2 au and is around an M-dwarf, has a small vertical aspect ratio. This suggests that the combination of a higher stellar temperature and a small R_0 are requirements for creating a disk that has a particularly large aspect ratio.

Further questions remain. For instance, it is not clear why these disks have small R_0 values, as Esposito et al. (2020) (first reported in Matrà et al. (2018)) shows that there is a positive correlation between stellar luminosity and R_0. This means that as the stellar temperature/luminosity increases, we would expect a peak dust density radius farther out from the star, making these four disks outliers. One possible explanation could be that due to the high inclination of these disks, it is difficult to measure the exact peak radius, leading to an underestimation of R_0. While HR 7012 is undoubtedly compact, this cannot be easily said for the other three disks which extend well beyond their measured values of R_0 in scattered light. However, in the case of HD 110058 and HD 114082, ALMA observations also show relatively compact disks, with a peak radius of mm-sized grains at 31 au and 24.1 au, respectively (Hales et al., 2022; Kral et al., 2020), consistent with their measured R_0 in scattered light within uncertainties. The β Pic disk is the most uncertain, where both the small grains in scattered light and large grains as seen by ALMA extend way beyond R_0, which is near the measured inner radius, and is more consistent with being radially

broad. While we do measure a consistent disk radius of 27.06 au, this is at the edge of GPI's FOV, and therefore it is possible for the disk radius to lie beyond this distance.

Another explanation for these disks being more compact in terms of R_0 could be due to shaping from planet or stellar companions. In the case of HR 7012, as mentioned previously, the system has a stellar companion located >2000 au from the main star (Torres et al., 2006), which has been suspected to be the cause of the disk's significant truncation, however, this has yet to be confirmed. For HD 110058, there is evidence of a warp past 40 au, which suggests perturbation from a planet companion. If there is a planet that is orbiting closely outside of this warp, this could lead to a truncation of the disk. That being said, a planet could cause a similar warp inside of the disk, similar to the β Pic system, where Pearce et al. (2022) predicts that a sculpting planet of mass $\geq 0.5 \pm 0.4$ M_{Jup} with semi-major axis $\leq 8 \pm 8$ au is sufficient to create a warp at 40 au. While a planet is known to exist in the HD 114082 system (Engler et al., 2022; Zakhozhay et al., 2022), this planet is within 2 au of the star, making it dynamically uncoupled from the disk. However as seen in Engler et al. (2022), there is a clear opening within the inner radius of the disk, likely meaning that there are additional planets closer to the disk edge, and given that the disk is radially narrow, this suggests that there may also be a shepherding planet outside of the outer disk edge. Finally, the β Pic is also known to have two planets, β Pic b and c, (Lagrange et al., 2010, 2019). These planets are very likely perturbing the disk and have even been directly linked to the known disk warp located at ∼50 au (Mouillet et al., 1997). While this may not fully explain the small R_0 value, Matrà et al. (2019) found using ALMA observations that the vertical structure of the disk is best fit with two Gaussians rather than one, suggesting the existence of both a cold and hot population of dust grains. The authors state that this distribution of dust grains is not consistent with stirring from β Pic b alone, but could be the result of another unseen planet migrating outwards toward the inner disk edge.

Aspect Ratio & Particle Size Distribution

While an unknown planet may be puffing up the β Pic disk, in the case of HR 7012, there is strong evidence of the disk as a whole being the result of a high-speed collision between large planetesimals. While the disk is shown to harbour SiO and CO as a result of these collisions (Lisse et al., 2008; Schneiderman et al., 2021), another piece of evidence is the disk's dust grain size distribution power-law (q) of 3.95 (Johnson

et al., 2012). This power law is steeper than the typical power-law for a collisional cascade of $q = 3.5$ (Dohnanyi, 1969), where lab work has shown that a high q-value is consistent with what is expected for the aftermath of a giant hypervelocity impact (Takasawa et al., 2011). This motivates us to look more closely at the affects of q on the vertical aspect ratio, alongside R_0 and stellar temperature. For disks that have measured q-values in the literature (see Table 3.5), we plot these values vs. their measured aspect ratios, which can be seen in the left plot Figure 3.13. We note that most of these q values are measured by extrapolating from millimeter to centimeter observations, however, some disks only have measured q values from radiative transfer modelling of scattered light observations and/or the SED. Plotting aspect ratio vs. q, we find a tentative positive trend between q and the vertical aspect ratio, where the average q-value for disks with an aspect ratio $\gtrsim$0.25 is $\sim$3.74, while the average q-value for disks with an aspect ratio $\lesssim$0.25 is $\sim$3.20. While the disks with $q \gtrsim 3.5$ are on average more compact in terms of R_0, there otherwise does not seem to be a correlation between q and R_0. The left plot of Figure 3.13 is similar to Figure 3.12, however, we replace R_0 with q. Doing so, we find that regardless of the stellar temperature (in contrast to the findings in MacGregor et al. 2016), q appears to increase with the vertical aspect ratio. Measuring the statistical significance of the correlation between the aspect ratio and q, we derive a Pearson correlation coefficient of 0.6 with a p-value of 0.05. When removing β Pic, which appears to be an outlier, the Pearson correlation coefficient increases to 0.7 with a p-value of 0.01. These values show that the correlation between aspect ratio and q is significant, however, it is important to keep in mind that our sample size is small.

A steep q-value suggests a large population of the smallest dust grains in the system, and as mentioned before, can be a sign of a giant hypervelocity collision between planetesimals. The two disks with the largest q-values are HD 114082 and unsurprisingly, HR 7012, both which have large vertical aspect ratios. While HR 7012 is highly suspected to have a recent giant impact, the same is not true for HD 114082. Unlike the HR 7012 disk, the HD 114082 disk has no significant amount of gas detected (Kral et al., 2020). Additionally, past studies of the disk have found a relatively large minimum dust grain size of between 5-10 μm (Engler et al., 2022; Wahhaj et al., 2016), which is larger than the expected blowout size of 2.4 μm and is supported by our findings of the disk being neutral in color, again inconsistent with a giant impact scenario. Other studies have shown that a steep q-value (between $\sim$3.65 and 4) can simply be the result of collisions between similar sized bodies in

Table 3.5: Measured grain size power law index, q, values with uncertainties for each disk listed, taken from the literature.

Disk	q	Reference
AU Mic	<3.33	Löhne (2020)
β Pic	3.49 ± 0.06	Löhne (2020)
HD 32297	3.07 ± 0.12	Norfolk et al. (2021)
HD 35841	$2.90^{+0.10}_{-0.20}$	Esposito et al. (2018)
HD 61005	3.33 ± 0.04	Löhne (2020)
HD 106906	$3.19^{+0.11}_{-0.20}$	Crotts et al. (2021)
HD 114082	>3.9	Wahhaj et al. (2016)
HD 115600	3.65 ± 0.15	Thilliez & Maddison (2017)
HD 131835	3.13 ± 0.07	Löhne (2020)
HD 157587	$3.73^{+0.81}_{-0.08}$	Bruzzone (2018)
HR 4796 A	3.43 ± 0.06	Löhne (2020)
HR 7012	3.95 ± 0.10	Johnson et al. (2012)

the strength-regime (Pan & Schlichting, 2012), meaning that the collisional bodies are held together by their own material strength rather than by gravity. Analytical and numerical calculations indicate that rocky bodies do not become dominated by self gravity until they reach a size of $\sim$1 km (Wyatt et al., 2011), suggesting that collisions in these two disks are primarily between smaller bodies. This is expected for HR 7012, as the fine dust is expected to be from the sub-sequential collisions between sub-mm size dust grains rather than the initial giant impact (Johnson et al., 2012).

When studying the aspect ratio of our sample of debris disks, there are clear trends that have emerged. The stellar temperature, the disk's radial extent, and distribution of dust grain sizes, all appear to affect the vertical aspect ratio. Further study is needed to explore the relationship between the vertical aspect ratio and these other system parameters, in order to help better understand the processes that are occurring in these disks.

3.3.5 Polarized Intensity Profiles

One interesting observation when comparing the surface brightness profiles shown in Figure 3.6 side by side, is the similarity between the profile shapes for the disks in our sample. For the majority of higher inclined disks, the surface brightness profiles peak at separations closer to the star before gradually decreasing with increasing stellar

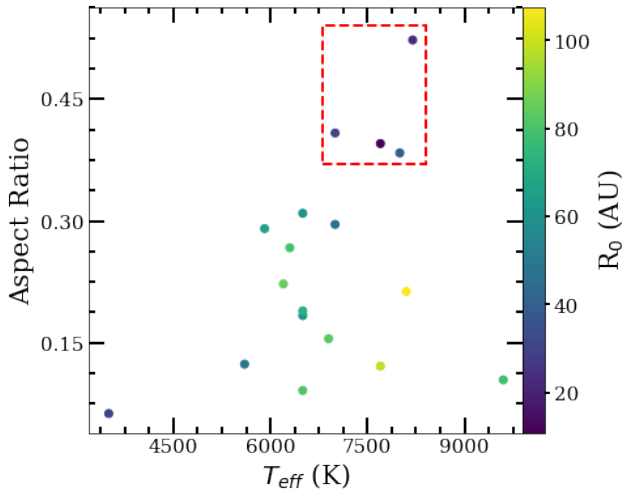

Figure 3.12: Aspect ratio for the disks in our sample with $i \gtrsim 70°$ as a function of stellar temperature. The color of each point represents R_0 in au, as indicated by the color bar, taken from Esposito et al. (2020). The four disks highlighted within the red dashed square are the same four disks highlighted in Figure 3.4.

Figure 3.13: **Left:** Aspect ratio for the disks listed in Table 3.5 as a function of their measured dust grain size power-law, q. The color of each point represents R_0 in au. **Right:** Aspect ratio vs. the stellar temperature, same as Figure 3.12, however, the color of each point represents q, instead of R_0.

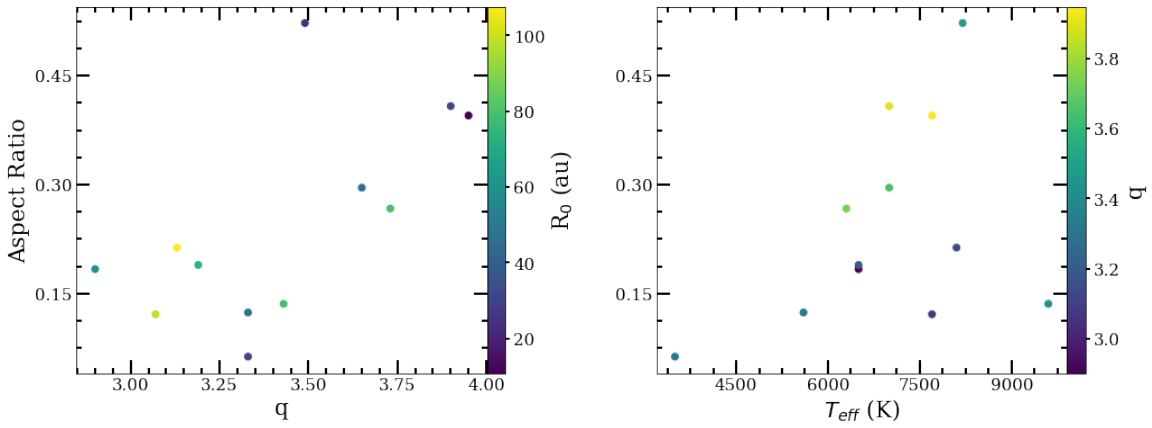

separation. In the cases of HD 32297 and HD 106906, the surface brightness profile peaks closest to the star, with a second, smaller peak at larger stellar separations. Several disks have more flat surface brightness profiles such as AU Mic, HD 61005 and HD 30447, although AU Mic and HD 61005 extend beyond GPI's FOV. For lower inclined disks, again all the surface brightness profiles are very similar in that the surface brightness gradually decreases from the star before peaking again at the disk ansae. One outlier is HD 191089, where the surface brightness stays fairly flat with separation from the star. However, this disk is relatively low in S/N compared to the other lower-inclined disks in our sample. These surface brightness profiles can provide information about the disk scattering phase function (SPF), suggesting that the SPF is very similar between disks. Other studies have also made this observation (e.g., Hughes et al. 2018) when comparing the SPF of several debris disks, solar system comets, and zodiacal dust. In another example, Hom et al. (2024) find that by using the same generic SPF, derived from the SPF of bodies in our solar system (i.e. the rings of Saturn/Jupiter and multiple comets), they were able to achieve low residual models for multiple debris disks a part of our GPI sample, further supporting a universal SPF. Such similarity of the SPF between debris disks and zodiacal dust implies that the dust in the majority of debris disks are porous aggregates, such as with cometary dust.

3.3.6 Sources of Disk Morphologies

While we cannot make any definitive statements of whether or not planets exist in some of these systems without direct detection of said planets, we can take all of our analysis and results for each disk to help determine which scenario the disk morphology is most consistent with, whether that be interaction with a companion or another mechanism. To do so, it is important to understand how different mechanisms affect the disk in different ways.

Planets by themselves can affect the disk morphology in numerous ways. This can be seen in studies such as Lee & Chiang (2016), where they show that a single 10 $M_{\oplus}$ planet on an eccentric orbit can create multiple different morphologies observed in multiple debris disks, such as "the Needle" and "the Moth". In addition to these outcomes, planets can create other features such as eccentric disks, brightness asymmetries, gaps, rings, and warps. If a planet lies close the disk edge, it can also effectively stir the disk as discussed in the previous Section. For example, Pearce

et al. (2022) uses disk stirring along with disk sculpting arguments to predict the masses of potential planets in a large sample of debris disks. It should be noted that interactions with stellar companions (if present), as well as stellar flybys can also perturb debris disks similarly to planets. While planets can effectively sculpt debris disks, it is unclear whether or not a significant color asymmetry would appear solely as a result of planet-disk interactions, although such interactions may result in additional collisions, populating the disk with small grains, and would change the scattering angles in the case of induced eccentricity on the disk.

For disks with a significant disk color asymmetry, other mechanisms may explain what is happening in the disk. Two mechanisms that have been commonly used to explain perturbed disks are interactions with the ISM (Debes et al., 2009) and large scale collisions in the disk (Jackson et al., 2014). Both these scenarios are able to alter the distribution of dust grains which could cause a disk color asymmetry. In the case of an ISM interaction, if the disk passes through a dense region of the ISM, this can cause preferentially small dust grains to be blown out in the opposite direction of the system's motion. If small grains are redistributed from one side of the disk to the other, this can cause one side of the disk to become brighter and bluer in color than the other, especially at shorter wavelengths. Additionally this can cause the bluer side to also become more radially extended and create a "Needle" or "Moth" like morphology depending on the viewing angle. On the other hand, recent large impacts can generate a large amount of small dust grains at the site of collision. These dust grains are put on highly eccentric orbits, making the opposite side of disk more radially extended, while the collision site becomes a pinched point through which the orbits of all the dust grains must pass (Jackson et al., 2014). Such an event could cause the side of the disk where the collision occurred to become more blue (due to a concentration of small dust grains) as well as become significantly brighter than the opposite side. For the three disks with brightness asymmetries and color asymmetries (HD 61005, HD 110058 and HD 157587) the brighter side of the disk is also bluer compared to the dimmer extension, as would be expected for either a ISM or large impact scenario.

To visually summarize our findings of asymmetries found for each disk, we plot the average brightness asymmetry between all bands, measured in Section 3.2.2, as a function of the offset found along the major axis shown in Figure 3.14. The orange shaded regions represents the area of parameter space where the brightness asymmetry is consistent with the direction of the major-axis offset (i.e. a brighter West side

Figure 3.14: Here we show the average brightness asymmetry across all bands vs. the measured major-axis offset or δ_x in au. Dark blue data points are disks with multiwavelength observations, while light blue data points are disks with H band observations only. Orange shaded regions represent the parameter space where disks have brightness asymmetries that are consistent with the direction of the major-axis offset.

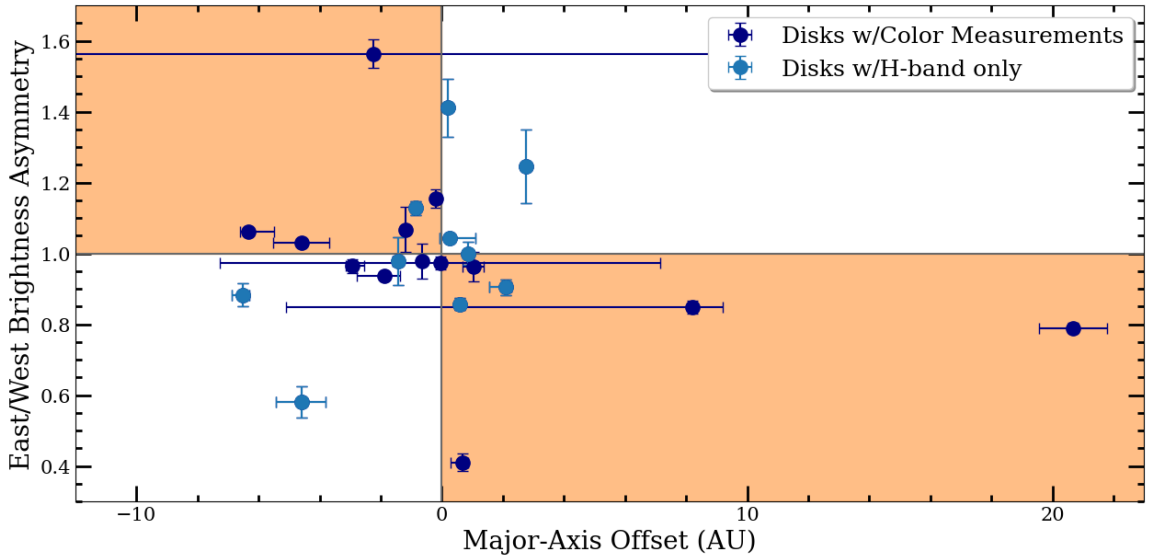

should be closer to the star and vice versa) as in the case of an eccentric disk. We find the majority of disks have brightness asymmetries as expected for an eccentric disk, although there are a handful of disks that have brightness asymmetries that are not consistent with an eccentric disk. A majority of the inconsistent disks do not have multiwavelength observations.

Going a step further, we place each disk into one of 6 categories based on their brightness asymmetry, major-axis offset, whether or not the brightness asymmetry is consistent with the offset direction, expected brightness asymmetry based on the offset, and the disk color asymmetry. This information can be found in Table 3.6, and will be discussed further in the subsequent Sections. To calculate the expected brightness asymmetry, we use the relationship between the surface brightness and radius from the star (i.e. $1/r^2$). However, given that the scattering angles change when the disk is offset from the star, the disk SPF also affects the expected brightness asymmetry. With this in mind, we also calculate the contribution from the SPF using the generic SPF derived in (Hom et al., 2024). This is an approximation as the SPF of the debris disks in our sample may not necessarily conform to this generic SPF, such as the case with HR 4796 A (see Figure 6 in Hughes et al. 2018), although,

as mentioned in Section 3.3.5, the similarities between surface brightness profiles suggest this is a fair assumption. In general, the effect of the SPF partially cancels out the expected brightness asymmetry based on $1/r^2$ alone, as the opposite side of the disk (apocenter) becomes brighter due to the change in scattering angles. Our approximation of the expected brightness asymmetry in Table 3.6 is represented as a range between the expected brightness asymmetry based on $1/r^2$ alone, and when taking into account the contribution from the SPF. For a fair comparison, we recalculate the surface brightness asymmetry for each disk (and each band) at the same radii as we calculate for the expected brightness asymmetry, focusing on stellar separations mid way between the star and the measured disk radius to avoid the effects of limb brightening at the ansae and noise close to the star. The average surface brightness asymmetry can be found in Table 3.6. For simplicity, we focus on the major-axis offsets to calculate the expected brightness asymmetries.

Category 1: Eccentric Disk

In this first category, the debris disks are consistent with having an eccentric disk. This means that the derived brightness asymmetries are consistent with the direction of the major-axis offset, the expected brightness asymmetry is consistent with the measured asymmetry, and finally these disks do not present a significant disk color asymmetry. There are five disks that fall into this category; HD 32297, HD 106906, HD 146897, HD 156623 and HR 4796 A.

While HD 32297 is close to axisymmetric, we place it in category 1 as we derive a significant offset of ∼4 au, which is present in both the J and H band. The derived offset is also still consistent with the insignificant brightness asymmetry given the large disk radii. On the other hand, the HD 106906 disk is very asymmetric, with a massive disk offset along the major-axis of ∼20 au and a significant brightness asymmetry. Despite such a large disk offset, the measured brightness asymmetry is still consistent within the range calculated for the expected brightness asymmetry. If confirmed, the HD 146897 disk also has a large offset relative to the derived disk radius, making it one of the more eccentric disks in our sample. Given the small disk radii, measuring the brightness asymmetry between the star and the disk radius requires us to average the disk surface brightness close to the star, resulting in a high uncertainty measurement of 1.20±0.15 (i.e. the West side of the disk is 1.20±0.15 times brighter than the East side). Despite this high uncertainty, the expected brightness asymmetry of ∼1.10-1.25

Table 3.6: Summary of asymmetry for each disk. Column three is the brightness asymmetry measured in the H band, while column 5 is the range of expected brightness asymmetries based on the $1/r^2$ relationship and the SPF. Column 6 is the average disk color asymmetry for each disk. The table is organized by disks with similar asymmetries or features. See Section 3.3.6 for descriptions of each Category.

Name	δ_x (au)	Brightness Asymmetry	Consistent w/ Offset Direction?
Category 1			
HD 32297	-4.51	1.13±0.05	Yes
HD 106906	20.67	1.28±0.04	Yes
HD 146897	-6.31	1.20±0.15	Yes
HD 156623	2.24	1.05±0.02	Yes
HR 4796 A	0.58	1.02±0.02	Yes
Category 2			
HD 61005	0.69	1.82±0.09	Yes
HD 110058	7.80	1.23±0.03	Yes
HD 111520	-2.24	1.78±0.09	Yes
HD 117214	-0.19	1.14±0.05	Yes
Category 3			
β Pic	0.0	1.04±0.02	-
CE Ant	-0.86	1.01±0.02	Yes
HD 115600	0.0	1.01±0.05	-
Category 4			
HD 114082	-2.95	1.14±0.04	No
HD 129590	-1.91	1.09±0.06	No
HD 157587	-0.65	1.18±0.05	No
Category 5			
AU Mic	0.19	1.95±0.20	No
HD 30447	-6.53	1.19±0.08	No
HD 131835	-4.54	1.11±0.06	No
HR 7012	2.74	1.94±0.49	No
Category 6			
HD 35841	1.03	1.08±0.13	Yes
HD 111161	-1.09	1.04±0.07	No
HD 145560	0.86	1.02±0.05	-
HD 191089	1.20	1.08±0.12	Yes

Table 3.7: Continuation of Table 3.6

Name	Expected Brightness Asymmetry	Disk Color Asymmetry
Category 1		
HD 32297	1.03-1.08	0.03±0.04
HD 106906	1.17-1.43	0.09±0.05
HD 146897	1.10-1.25	0.05±0.03
HD 156623	1.03-1.07	N/A
HR 4796 A	≤1.01	N/A
Category 2		
HD 61005	1.01-1.03	0.70±0.15
HD 110058	1.11-1.28	0.28±0.04
HD 111520	1.02-1.05, 1.09-1.25	0.15±0.06
HD 117214	≤1.01:1	N/A
Category 3		
β Pic	-	N/A
CE Ant	1.03-1.05	N/A
HD 115600	-	0.0±0.04
Category 4		
HD 114082	1.08-1.21	0.19±0.07
HD 129590	1.03-1.08	0.10±0.06
HD 157587	≤1.01	0.30±0.08
Category 5		
AU Mic	1.01-1.04	N/A
HD 30447	1.06-1.17	N/A
HD 131835	1.04-1.10	N/A
HR 7012	1.32-1.87	N/A
Category 6		
HD 35841	1.02-1.05	0.04±0.08
HD 111161 No	1.01-1.03	N/A
HD 145560	≤1:1.01	N/A
HD 191089	1.02-1.05	0.07±0.12

is consistent with the measured brightness asymmetry.

For both the HD 156623 and HR 4796 A disks, we derive brightness asymmetries of 1.05±0.02 and 1.02±0.02 between the star and disk radius. For both disks the expected brightness asymmetries derived at the same radii are consistent with these measured brightness asymmetries within 1σ. These two values are significantly lower than the brightness asymmetries measured across the entire disk in Section 3.2.2 (1.11±0.02 and 1.17±0.02, respectively). This is due to the brightness asymmetry being strongest near the disk ansae for both disks, as can be seen in Figure 3.6. For the HR 4796 A disk, Olofsson et al. (2019) found that with the derived eccentricity of ∼0.02, their model was unable to match the surface brightness at the ansae, leading to the conclusion that dust may be released preferentially near the East disk ansae due to more frequent collisions. A similar scenario could be the case for HD 156623, although more complex modelling may find that our derived eccentricity is sufficient enough to produce the brightness asymmetry along the entire disk.

A common explanation used to explain an eccentric disk is perturbation from an eccentric planet. For the HD 32297 debris disk, Lee & Chiang (2016) have shown that a planet on an eccentric orbit can create the double wing feature seen in the disk halo with HST. This requires the azimuth of the planet to be close to 0°, which can explain why the disk appears close to axisymmetric. For the planet to sculpt the inner edge of each disk, Pearce et al. (2022) derives a minimum planet mass and maximum separation of $1.1^{+0.4}_{-2.0}$ M_{Jup} and 70^{+8}_{-2} au for HD 32297, and 2.0 ± 0.4 and 43^{+7}_{-9} for HD 146897, however, this is not including the measured eccentricity from this study. The radially narrow ring of the HR 4796 A disk may be the result of a shepherding planet inside the planetesimal belt, as described in Olofsson et al. (2019). However, in the case of HD 156623, no inner clearing is observed as the polarized intensity is detected down to the FPM, meaning that either a planet is shaping the disk from within the FPM or outside the disk, or another source is causing the disk to become eccentric. Using an orbital separation of 10 au, Pearce et al. (2022) finds a planet mass of 0.6 M_{Jup} is required to sculpt the disk. Given that the HD 156623 disk is gas rich, if the gas disk is eccentric, this can force the dust disk to become eccentric as well (Lin & Chiang, 2019), a scenario that has also been used to help explain the moth-like wings of HD 32297. However, such a scenario still requires a perturber, such as a planet, to make the gas disk eccentric.

The HD 106906 system is the only one in this category with a known planet. Past studies have shown that perturbation from the planet HD 106906 b can replicate the

observed disk morphology and has a consistent orbit (Nesvold et al., 2017; Nguyen et al., 2021; Moore et al., 2023). Other studies have show that the disk morphology is also well created by a recent catastrophic collision taking place in the disk's East extension (Jones et al., 2023), making it an alternative scenario for the disk asymmetries, although no other evidence of a large collision has been found.

Category 2: Eccentric Disk + Additional Explanation Needed

Category 2 consists of debris disks in our sample that are consistent with an eccentric disk, but either have a significant color asymmetry in at least one or more bands and/or have measured brightness asymmetries much larger than expected. The four disks that fall under this category are HD 61005, HD 110058, HD 117214 and HD 111520.

The HD 61005 and HD 111520 disks have two of the largest brightness asymmetries in our sample; however, the estimated major-axis offsets are too small to explain these large brightness asymmetries. Even if we take the estimated 11 au offset based on the polarized surface brightness profile for HD 111520 (Crotts et al., 2022), this only creates a brightness asymmetry of $\sim$1.09-1.25 (compared to the measured 1.78$\pm$0.09 averaged between bands). It is possible that the expected brightness asymmetry would change when taking into account the full eccentricity (i.e. if both the offset along the major- and minor-axis were well constrained), as well as the argument of pericenter, although this is difficult to do empirically for such high inclined disks. In the case of HD 61005, the "moth"-like halo suggests an argument of pericenter close to 0, meaning that the disk eccentricity would be primarily along the minor-axis, and therefore should not cause a large brightness asymmetry along the major-axis. The halo of the HD 111520 disk shows more radial asymmetry including the warp, "fork"-like structure, and difference radial extent, suggesting that the argument of pericenter is much farther from zero, and that an offset along the major-axis is required. Dynamical modelling of the system may help to uncover the true orientation of the disk in order to create such asymmetries.

In Jones et al. (2023), the authors try to explain the morphology for both disks with a recent giant collision; however, neither disk is fully consistent with this scenario. In the case of HD 111520, while a giant collision can create a fork like structure as observed, the orientation of the fork is incorrect, where the micron sized grains align with the lower fork rather than between the two forks as would be expected. We

would also expect the site of the collision (i.e. the East extension) to be the brighter side, whereas we observe the opposite. For HD 61005, while a large collision can create the moth-like structure of the disk halo, the authors of Jones et al. (2023) note that the brightness ratio between the two sets of disk wings is incorrect, as well as the secondary wings are not as straight as seen in observations. The disk halo morphology may be better explained by interaction with a planet companion on an eccentric orbit, where Lee & Chiang (2016) show that such a planet can create the "moth" and "bar" like morphologies, although the "bar" morphology requires a steep dust grain size distribution close to the blow-out size. HD 111520 disk's morphology may also be explained by a planet-disk interaction, as the halo shows a clear 4° warp beyond 1.7″ (Crotts et al., 2022), a planet-disk interaction may also be able to create the fork-like structure (Pearce & Wyatt, 2014).

An interaction with the ISM is another mechanism that may be affecting either disk. This is a scenario that has been used to help explain HD 61005, and has been shown to be able to create both a moth- and needle-like morphology (Maness et al., 2009; Debes et al., 2009). Given that HD 61005 proper motion (corrected for solar reflex motion) is near perpendicular to the disk wings, this may be another explanation for the disk's morphology. Additionally, the proper motion also points slightly more West compared to the major-axis (∼19.2° from perpendicular), which may be able to explain the disk color asymmetry, which is found to be significant in the J and H bands, although further study is needed to confirm this. On the other hand, to create the more needle-like morphology of HD 111520's disk halo, the proper motion should be pointing away from the West extension. However, after correcting for solar reflex motion, the proper motion also near perpendicular to the disk, essentially ruling out this scenario.

Similar to the HD 61005 disk, the HD 117214 disk also has an insignificant offset along the major-axis (along with the minor-axis), while having a significant brightness asymmetry. It is unclear from our data alone what the source of this brightness asymmetry is, as we are unable to perform a multiwavelength analysis for this disk. A deeper analysis of the polarized-intensity data alongside the total-intensity observations (presented in Esposito et al. 2020) may help shed additional information about the disk morphology as a whole. Finally, the HD 110058 disk is one of the most asymmetric in our sample, with a large brightness asymmetry, possible eccentricity, disk color asymmetry and warp. While the disk offset may be the result of an asymmetric disk geometry due to the warp, especially given that past studies find no eccentricity,

the warp itself suggests that the disk is being perturbed by a planet companion. If the disk is eccentric, the expected brightness asymmetry is consistent with the observed brightness asymmetry. However, the disk also has a significant disk color asymmetry in J-H and J-$K1$, where the East extension is relatively more blue than the West extension, although the strong overall red disk color suggests a larger minimum dust grain size, on the order of $\gtrsim$1 μm (Boccaletti et al., 2003). Further analysis of recently published HST observations (Ren et al., 2023) may provide additional information.

Category 3: Additional Geometrical Asymmetries

Category 3 contains debris disks that have other geometrical asymmetries (rather than an eccentric disk) that may be contributing to their surface brightness asymmetries or are signs of dynamical perturbation from a companion. This category includes β Pic, CE Ant, and HD 115600.

In the case of β Pic and CE Ant, other morphological asymmetries may be responsible for the brightness asymmetries observed. For β Pic, a massive clump of gas and dust resides in the brighter West extension. While this clump mainly resides outside of GPI's FOV, at ∼52 au, the brightness asymmetry caused by the clump may extend within GPI's FOV as Han et al. (2023) show the clump to extend down to ∼35 au (at the edge of GPI's FOV). Han et al. (2023) also show that this clump is likely stationary, which is consistent with a recent giant impact scenario. For CE Ant, as mentioned previously and as seen in Figure 3.17, the disk contains a spiral arm in the SW quadrant. As our chosen apertures partially cover this area, it is possible that the extra flux from the spiral arm is contributing to the observed brightness asymmetry as measured in Section 3.2.2. When measuring the surface brightness only at radial separations halfway between the star and the disk radius, we find no significant brightness asymmetry. The existence of this spiral arm also suggests the presence of a planet companion, which hopefully could be imaged in future observations such as with JWST.

The HD 115600 disk is close to axisymmetric with no measured offset, significant brightness asymmetry or significant color asymmetry. However, after measuring the vertical offset profile, we find a tentative warp beyond ∼0.45″, where the East extension bends downwards and the West extension bends upwards. This makes the HD 115600 disk similar to the HD 110058 disk, which has a confirmed warp, and suggests that a planet on an inclined orbit, relative to the disk, is present in the system. Better

resolved observations of the disk, or observations of the disk halo such as with HST, will be useful to confirm the existence of the warp.

Category 4: Inconsistent with Eccentricity + Color Measurements

Category 4 includes debris disks that are inconsistent with an eccentric disk, meaning that their brightness asymmetries are not consistent with the direction of the major-axis offset. Additionally, these disks have multiwavelength observations which allow us to perform color measurements to see whether or not any asymmetries in the disk color are present. The three disks that fall in this category are HD 114082, HD 129590, and HD 157587.

The HD 114082 and HD 129589 disks are similar in that they both present significant brightness asymmetries in the $K1$ band (where the East side is brighter than the right), but not in the H band. Additionally, in both cases, the disk offsets derived from our geometrical fitting support an offset along major-axis in the opposite direction as would be expected to create the observed brightness asymmetries. Given this discrepancy, neither disk has strong disk color asymmetries with significance above 3σ, making it unclear what is causing the brightness asymmetry specifically in the $K1$ band for either disk. For the overall disk color, both disks exhibit a neutral to red disk color in H-$K1$, meaning the disk is brighter at longer wavelengths, and suggests that the minimum dust grain size in these systems are on the order of a few microns or larger. As discussed previously, the estimated minimum dust grain size for HD 114082 is found to be between $\sim$5-10 μm (Engler et al., 2022; Wahhaj et al., 2016), which is consistent with the near neutral disk color observed based on calculations from Boccaletti et al. (2003).

Unlike the previous two disks, the HD 157587 disk has a significant color asymmetry, most notably in J-$K1$, where the brighter East extension is relatively more blue than the West extension. This color asymmetry is only significant in J-$K1$, due to the fact that we only measure a significant brightness asymmetry in the J band, where H and $K1$ observations are consistent with being axisymmetric within 3σ. This could suggest that the smallest grains in the system may be perturbed, whereas the larger grains are less so. Such a phenomenon could be the result of an ISM interaction, although the proper motion of the system, after correcting for solar reflex motion, is pointing towards the perpendicular relative to the disk major-axis when we would expect it to be pointing more towards the West extension. Shorter

wavelength observations, such as with HST, would be useful to determine if there are any structures in the disk halo that could help distinguish the source of the color asymmetry in the HD 157587 disk.

Category 5: Inconsistent with Eccentricity + No Color Measurements

Category 5 contains disks that have measured major-axis offsets and/or brightness asymmetries, but the disk offset is in the opposite direction as expected to create the measured brightness asymmetry. Additionally, these disks do not have multiwavelength observations to show whether or not they have disk color asymmetries. This category includes the following disks: AU Mic, HD 30447, HD 131835, and HR 7012.

For the disks AU Mic, HD 30447, HD 131835, and HR 7012, all four have either tentative (in the case of HR 7012) or significant brightness asymmetries, although the measured offset is in the opposite direction from what would be expected for an eccentric disk. For AU Mic, the low S/N of the data and spatial scale of the disk make it unfeasible to measure an offset accurately. However, there is evidence that suggests AU Mic may have impacted by a recent catastrophic collision resulting in the fast moving ripples that have been observed (Chiang & Fung, 2017). HR 7012 is another disk that has likely experienced a recent catastrophic collision, as discussed in the previous sections. Surprisingly, with our GPI observations, we derive a disk offset that leads to a very large eccentricity, while there is also the possibility of a large brightness asymmetry, albeit it is still consistent with no asymmetry within 2σ. If this brightness asymmetry does exist, it would not be consistent with the direction of the derived offset, nor is it consistent with the expected brightness asymmetry. Given that previous observations with SPHERE show the disk to be axisymmetric, the asymmetries seen with GPI may be simply due to unremoved noise close to the FPM.

Both the HD 30447 and HD 131835 disks have significant brightness asymmetries, with a brighter East extension, but both also have derived offsets that suggest that the West extension is closer to the star. The HD 30447 disk is an interesting case, as the peak polarized intensity occurs close to the star in the East compared to the right, suggesting that the East extension could in fact be closer to the star. Given the low S/N of the H-band observations, we may not be able to accurately measure the major-axis offset of the disk. It is also possible that the measured offset is due to a geometrical asymmetry other than an eccentric disk. New HST observations show the

geometry of the disk halo to also be asymmetric, where the East extension extends farther radially compared to the West extension (Ren et al., 2023). A more in depth analysis of the HST observations, and possibly future higher resolution observations of the disk in the NIR will be useful to better constrain the disk geometry. The case for HD 131835 is similar. The GPI observations have fairly low S/N, making it more difficult to measure the disk geometry. Given the evidence for multiple rings and a broad parent disk, it is also possible that the disk geometry is more complicated than can be captured with our simple ring model. Again, higher resolution observations in scattered light will be useful in better constraining the full disk geometry.

Category 6: Most Axisymmetric

This final category simply consists of disks that are the most axisymmetric and do not have any strong evidence of harbouring asymmetries. The disks that fall into this category are HD 35841, HD 111161, HD 145560 and HD 191089. While there are small measured offsets for HD 111161 and HD 145560, these are insignificant taking into account the lower S/N of these two observations. The HD 35841 and HD 191089 disks also have measured offsets, but again, these offsets are very small ($\lesssim$1 au). Additionally none of these disks have significant brightness asymmetries, while the HD 35841 and HD 191089 disks also have no significant color asymmetries. Despite being near axisymmetric, three out of four disks have clear cavities within their inner radii, while the HD 35841 disk also appears to have an inner cavity in total-intensity (see Esposito et al. 2020), meaning that these disks may still be carved by planets, and are worth following up with instruments such as JWST that have the ability to find planets in these systems.

Summary of Planet-Disk Interactions

In this Section we briefly summarize which disks may be perturbed and/or shaped by planets based on our findings and results from previous studies.

Both Category 1 and 2 disks have disk morphologies consistent with planet-disk interactions. All nine disks are consistent with being eccentric, which can be caused by a planet on an eccentric orbit. Several of these disks also exhibit other morphological features that are consistent with planet-disk interactions. For example, both HD 110058 and HD 111520 have confirmed warped disks (Kasper et al., 2015; Crotts et al., 2022), which can be caused by a planet on an inclined orbit relative to the

disk. Several of these disks also have disk halos consistent with perturbation from an eccentric planet, in the case of the "Moth" and "Needle" like halos of HD 32297, HD 61005, HD 106906 and HD 111520. However, other mechanisms can cause these morphologies as well, such as an ISM interaction or a recent giant impact. There is also the question of whether or not any asymmetries, such as eccentricity, may be carried over from the protoplanetary disk phase, as debris disks are thought to be progenitors of high mass, structured protoplanetary disks (Michel et al., 2021). While disks in Category 1 can be solely explained by an eccentric disk, disks in Category 2 (HD 61005, HD 110058, HD 111520, HD 117214) need further investigation to understand their higher than expected surface brightness asymmetries and/or their disk color asymmetries.

Not every disk in our sample may be eccentric or highly asymmetric, but many disks in our sample still exhibit cavities within their inner radii, showing that the material in this region has been cleared by some mechanism. This includes disks from all categories, including HD 114082, HD 129590, HD 157587, CE Ant, HD 30447, HD 117214, HD 131835, HR 4796 A, HD 111161, HD 145560, and HD 191089, where CE Ant and HD 131835 also harbour multiple rings.. These disks make good candidates for searching for planets within their cavities, such as with JWST. Additionally, the HD 114082 disk is radially compact, suggesting that the disk may be sculpted by a planet orbiting outside of the disk as well. Two disks from the above list with other possible planet-induced features are CE Ant and HD 30447, where CE Ant harbours a spiral arm, tentatively detected in our GPI data, while HD 30447 has a needle-like halo as seen in HST observations presented in (Ren et al., 2023). Finally, two additional disks that have evidence of perturbation from a planet are β Pic and HD 115600. Both disks are fairly axisymmetric as observed with GPI, although β Pic is known to have multiple asymmetries on larger scales, which have been shown to be connected to the known planets in the system. Similar to β Pic, as well as HD 110058 and HD 111520, HD 115600 have a tentative warp towards its outer edges as seen with GPI, which if confirmed suggests perturbation from an unseen planet with an inclination relative to the disk.

In summary, the majority of disks show at least one sign of planet-disk interactions through their morphologies, such as inner gaps, eccentric disks, spiral arms and warps. A number of disks in our sample also have brightness asymmetries, some of which are not consistent with an eccentric disk, along with asymmetries in disk color, showing that other mechanisms may be shaping debris disks as well. Future observations

with new and upcoming instruments will hopefully have the potential to detect the disk-perturbing planets in these systems.

3.4 Conclusions

In this study we present a uniform, empirical analysis of 23 GPI debris disks in polarized intensity, using multiwavelength J-, H-, and $K1$-band observations. Through this analysis, we fully characterize each disk morphology through measuring the disk geometry, vertical/radial width, multiwavelength surface brightness, and disk color. We also derive any asymmetries present in the disk by measuring disk offsets along the major and minor axes, as well as asymmetries in the surface brightness and disk color. While we analyze each disk individually, we also come to the following broader conclusions;

- The majority of our disks present at least one asymmetry. For example, we find 16 out of 23 disks present a significant brightness asymmetry of at least 3σ between the East and West extensions in at least one band. Out of the disks with multiwavelength data, 3 out of 12 disks also present a significant disk color asymmetry between the East and West extensions between at least one pair of bands. Additionally, we confirm the warp for the HD 110058 disk, while finding a tentative warp for the HD 115600 disk.

- Comparing the surface brightness and disk color asymmetries with stellar temperature and age, we find no significant trends. We do, however, find a tentative trend between the overall disk color and stellar temperature, where the disk color becomes increasingly red/grey as the stellar temperature increases. We find this trend strongest in H-$K1$, where several disks around hotter stars are strongly blue in J-H and J-$K1$, breaking the trend. This can be explained by natural collisional evolution, where studies have found that bright debris disks around F and A spectral-type stars can naturally produce a high density of sub-micron sized dust grains.

- We find 4 disks to have significantly higher vertical aspect ratios compared to other debris disks at similar inclinations. This includes β Pic, HD 110058, HD 114082 and HR 7012. Comparing the aspect ratios of our sample with other disk/system properties, we find that a combination of stellar temperature

and disk radius are correlated with the vertical width, as the four disks mentioned above are all around higher temperature stars *and* are radially compact with $R_0 < 40$ au. While the estimation of R_0 is most uncertain for β Pic, planet/stellar companions may be responsible for the radially compact nature of HD 110058, HD 114082, and HR 7012. Additionally, we find a positive correlation between the vertical aspect ratio and the dust grain size power law, q, where the vertical aspect ratio appears to increase with q. While a high q-value can be a sign of a giant hypervelocity collision, a high q-value can also be the result of collisions between similar sized bodies in the strength regime. Further analysis is needed to better understand the relationship between q and the vertical aspect ratio.

- Categorizing each disk based off their derived asymmetries, we find the following: 5/23 disks are consistent with an eccentric disk, 4/23 disks are consistent with an eccentric disk, but need further explanation for their higher than expected brightness asymmetries and/or disk color asymmetries, 3/23 disks have geometrical/surface brightness asymmetries not necessarily associated with an eccentric disk, 8/23 disks need further followup to determine the source of their brightness asymmetries, and 4/23 are most consistent with being axisymmetric.

Disks that are consistent with an eccentric disk, or harbour another geometrical asymmetry such as a warp or spiral (about half of our sample), may be the result of planet-disk interactions. While not every disk in our sample is significantly asymmetric in terms of surface brightness and/or disk geometry, this does not necessarily mean there are no signs of sculpting by a planet. For example, at least 10 out of 23 disks also show clear gaps within their inner radii, suggesting that possibly one or multiple planets are present and clearing out the material in these regions. To summarize, almost every disk in our sample features at least one asymmetry, while the majority of disks also present an asymmetry or feature that is suggestive of perturbation of a planet companion. These disks provide great candidates to search for planets with current and upcoming instruments, such as JWST NIRCam, in order to better understand exoplanetary architectures and how they evolve over time.

Figure 3.15: **Top:** Signal to Noise maps for each disk with multiwavelength observations. The circles represent the size of the FPM in J, H, and $K1$ (0.09″, 0.12″ and 0.15″ respectively), and the crosses represent the location of the star. **Bottom:** Signal to Noise maps for the remaining disks with observations in the H band only. The circles represent the size of the FPM in H band (0.12″), and the crosses represent the location of the star.

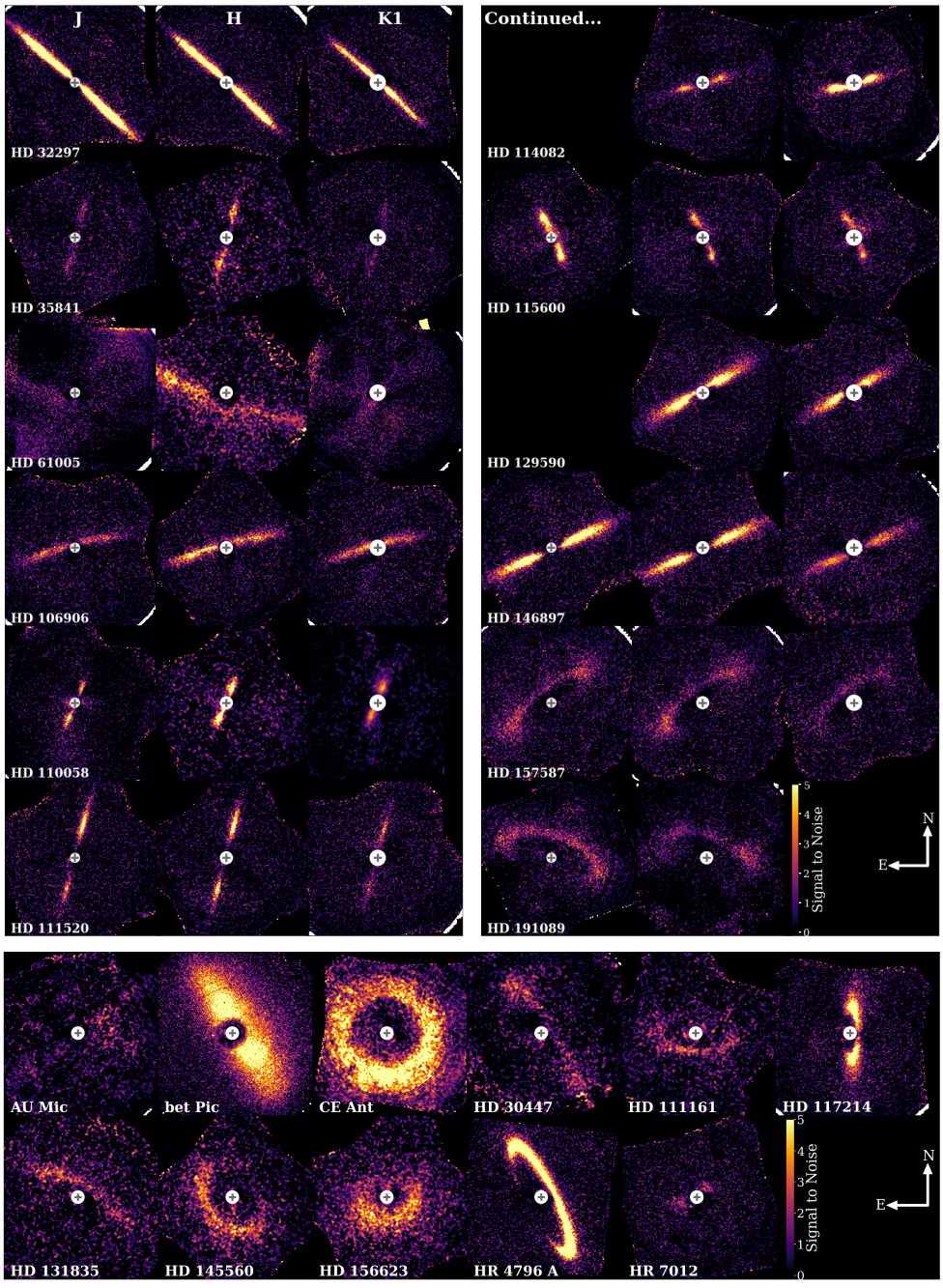

Figure 3.16: H-band observations rotated by their $PA - 90°$ and overlaid with their best fitting ring model (orange curves).

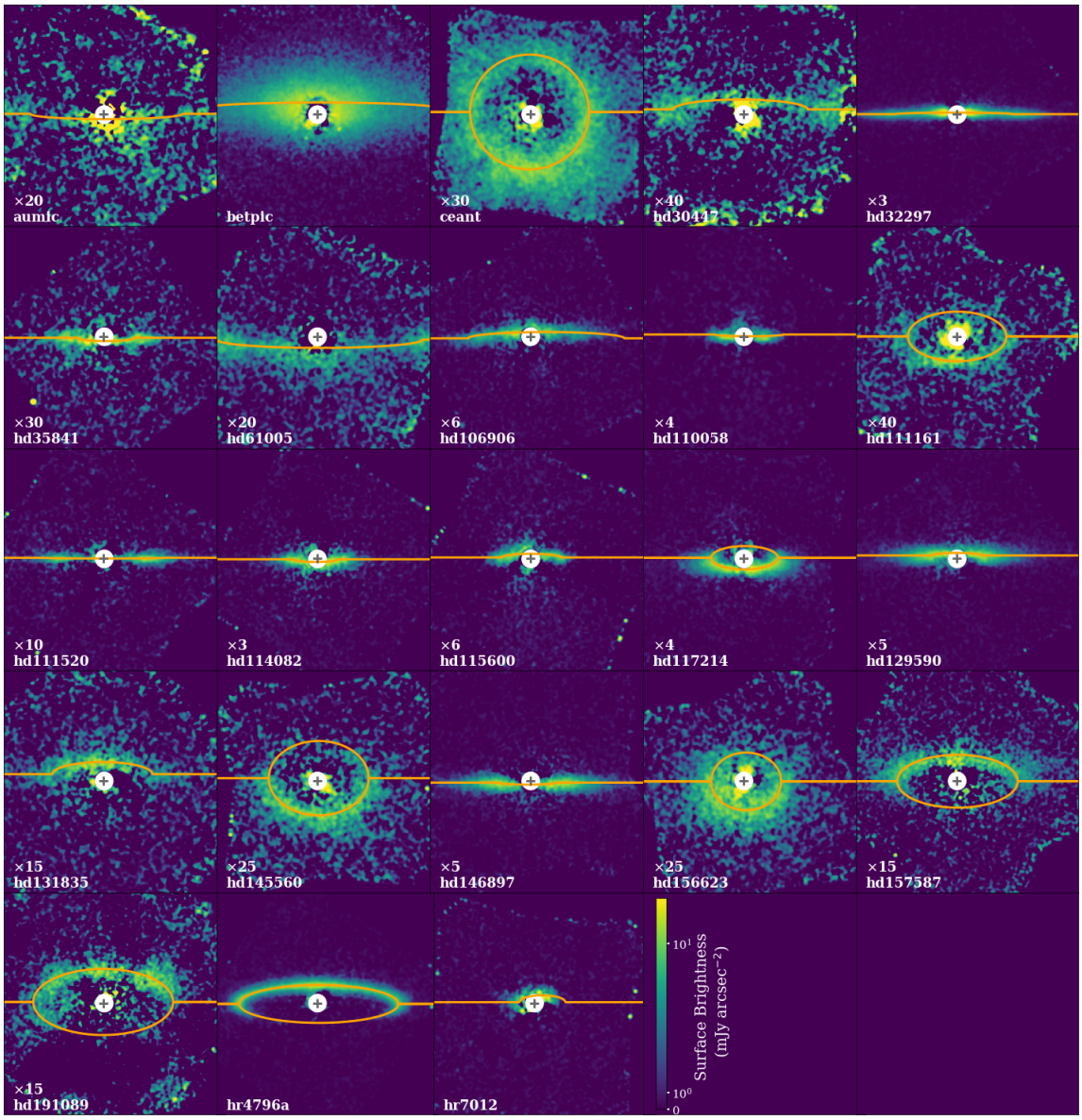

3.5 Additional Figures and Information

3.5.1 S/N Maps and Vertical/Radial Offset Profiles

We present here additional figures of the debris disks in our sample. Figure 3.15 shows S/N maps of each disk in the J, H and $K1$ bands. These are created by dividing the noise maps derived from U_ϕ from our Q_ϕ images (see Section 3.1. Every disk is scaled between a S/N of 0 to 5. Figure 3.16 shows the best fitting ring models overlaid on top of the H-band data. Each disk is rotated by its measured $PA - 90°$, so that the disk major-axis is horizontal in the image.

3.5.2 East vs. West Frame of Reference

Throughout this paper, we refer to the two extensions of each disk as the East and West sides/extensions. These definitions are based on a consistent frame of reference, rather than the original cardinal directions. To create the new frame of reference, we simply rotate each disk clockwise/counterclockwise so that the disk major-axis is horizontal in the image. The degrees rotated is equal to the disk $PA - 90°$. In Table 3.8, we list the angle each disk is rotated, as well as the change in cardinal directions from the original frame of reference to the new frame of reference.

3.5.3 Individual Disk Results

In the previous Sections, we describe the methods used in this study, as well as the results of these methods when applied to our sample of GPI disks. In this Section, we discuss the summary of our empirical analysis for each disk, and compare our results to those in the literature. We focus mainly on new and/or the most interesting results, while more minor results such as the inclination and PA are not highlighted unless they deviate significantly from previous results or in the cases where the disk is not well studied.

AU Mic

The AU Mic debris disk is one of only two disks in our sample that resides around an M-type star. Debris disks resolved around M-type stars in general are fairly rare given observational biases. AU Mic is a particularly interesting system, as the disk shows peculiar clumps of dust moving outwards from the star (Boccaletti et al., 2018), along

Table 3.8: Degrees each disk is rotated to create a consistent disk orientation and frame of reference between all 23 disks, i.e. disk emission left of the star = East side, disk emission right of the star = West side. Positive values represent clockwise rotation, while negative values represent counter-clockwise rotation. Column three shows the change in cardinal directions to East and West for both sides of each disk.

Disk	Degrees Rotated	Cardinal Change
AU Mic	36.7	SE $\rightarrow$ E, NW $\rightarrow$ W
β Pic	-57.8	NE $\rightarrow$ E, SW $\rightarrow$ W
CE Ant	1.02	E $\rightarrow$ E, W $\rightarrow$ W
HD 30447	-56.4	NE $\rightarrow$ E, SW $\rightarrow$ W
HD 32297	-42.4	NE $\rightarrow$ E, SW $\rightarrow$ W
HD 35841	77.5	SE $\rightarrow$ E, NW $\rightarrow$ W
HD 61005	-19.2	NE $\rightarrow$ E, SW $\rightarrow$ W
HD 106906	14.0	SE $\rightarrow$ E, NW $\rightarrow$ W
HD 110058	68.6	SE $\rightarrow$ E, NW $\rightarrow$ W
HD 111161	-6.7	E $\rightarrow$ E, W $\rightarrow$ W
HD 111520	75.7	SE $\rightarrow$ E, NW $\rightarrow$ W
HD 114082	15.0	SE $\rightarrow$ E, NW $\rightarrow$ W
HD 115600	-65.8	NE $\rightarrow$ E, SW $\rightarrow$ W
HD 117214	90.5	S $\rightarrow$ E, N $\rightarrow$ W
HD 129590	30.3	SE $\rightarrow$ E, NW $\rightarrow$ W
HD 131835	-29.2	NE $\rightarrow$ E, SW $\rightarrow$ W
HD 145560	-50.5	NE $\rightarrow$ E, SW $\rightarrow$ W
HD 146897	24.6	SE $\rightarrow$ E, NW $\rightarrow$ W
HD 156623	12.9	E $\rightarrow$ E, W $\rightarrow$ W
HD 157587	37.7	SE $\rightarrow$ E, NW $\rightarrow$ W
HD 191089	-18.2	NE $\rightarrow$ E, SW $\rightarrow$ W
HR 4796 A	-63.6	NE $\rightarrow$ E, SW $\rightarrow$ W
HR 7012	23.8	SE $\rightarrow$ E, NW $\rightarrow$ W

with two known planets recently discovered through the transit and radial velocity methods (Plavchan et al., 2020; Martioli et al., 2021).

The GPI observations for AU Mic are very low S/N, as can be seen in Figure 3.15, and the disk extends beyond GPI's FOV, making it difficult to obtain consistent values for the disk geometry. For example, we obtain a value of ∼86° for the inclination, when the literature reports an inclination between 88° and 90°. We also measure a small disk radius of ∼10 AU. While this value is consistent within the large uncertainties of previous inner radius measurements, the most recent ALMA data suggests an inner radius around 22 AU, more than twice our measured disk radii measurement (Vizgan et al., 2022). While it may simply be that we are unable to probe the true disk radius, given that the disk extends outside GPI's FOV, our derived radius could be a sign of a second disk component. Most recently, by using the code *Frankenstein*, which can deproject disks at any inclination to reveal their radial distribution, Terrill et al. (2023) find a second smaller peak in intensity at 10 au using ALMA observations. While this is a tentative detection, the same result has been found in multiple other studies in support of a second disk component around 10 au (Daley et al., 2019; Marino, 2021; Han et al., 2022).

In the H band, we find that the West side of the disk is about 1.4 times brighter than the East side. This brightness asymmetry can also be observed in the most recent SPHERE data (Langlois et al., 2021; Olofsson et al., 2022), in which the disk is better resolved. Currently, no literature reports any disk offsets or eccentricities, consistent with the almost zero offset detected with our ring fitting. However, with the low S/N and high inclination, it is very unlikely we would be able to constrain a disk offset along the major-axis. This does not necessarily mean that no offset exists, especially given that there is a clear brightness asymmetry; however, mm-observations with ALMA show an axisymmetric disk (Vizgan et al., 2022), suggesting that this brightness asymmetry and any possible disk offsets are only present in smaller grains. Whether this asymmetry is tied to planets in the system is unclear. The known planets in this system orbit very close to the star, making them dynamically decoupled from the disk, and efforts to search for additional planets farther out have yielded no candidates (Gallenne et al., 2022). A much more likely scenario would be that the distribution of dust grains in the disk is being altered. Although we do not have multiwavelength observations to test this, other studies have shown that the outward moving clumps of small dust in the system may be the result of a combination of stellar winds and a catastrophic collision (Chiang & Fung, 2017). This would explain why

the disk is highly asymmetric at shorter wavelengths, while being more axisymmetric at longer wavelengths.

β Pic

The β Pic debris disk is one of the most well-studied and well-known debris disks to date. Because the system is close (19.44 au), and the disk is particularly bright compared to other debris disks, β Pic was the first debris disk to ever be imaged (Smith & Terrile, 1984). The disk also hosts multiple interesting features including a warp, brightness asymmetry, radial asymmetry and a clump seen in ALMA observations to name a few (Heap et al., 2000; Kalas & Jewitt, 1995; Janson et al., 2021; Telesco et al., 2005). On top of this, the disk is one of only a handful of resolved disks with directly imaged planets, β Pic b and c (Lagrange et al., 2010, 2019), which can be directly linked to the disk's perturbed morphology (Chauvin et al., 2012).

While β Pic is known to have several asymmetries, the GPI observations show a fairly axisymmetric disk. We detect only a modest brightness asymmetry with a stronger West extension. Our vertical offset fitting also finds no significant offset along the major axis. For other aspects of the disk geometry, we find some discrepancies between our results and previous results in the literature. For one, our obtained inclination of 88.9° is several degrees higher than previous estimates of ∼85°. This difference may be the result of the β Pic disk being not radially narrow, or that the disk extends farther out than GPI's FOV, preventing us from fitting the entire vertical offset profile. In either case, β Pic is an example of limitations of our modelling technique, and likely requires a more complex model to capture the disk's complex morphology.

Although the surface brightness and disk geometry appear mostly axisymmetric, one interesting feature is β Pic's vertical width, where it has the highest aspect ratio of our entire sample. This is consistent with previous measurements, where β Pic has been found to have a relatively large vertical aspect ratio compared to other debris disks (Olofsson et al., 2022). The implications of β Pic's high aspect ratio is discussed in Section 3.3.4.

CE Ant

First imaged by Choquet et al. (2016), CE Ant, also known as TWA 7, is the lowest inclined disk in our sample, as well as the only one where the entire back side of the

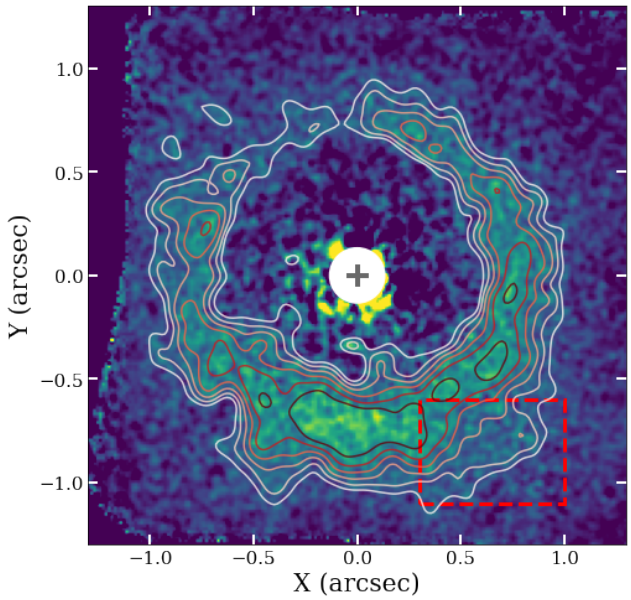

Figure 3.17: CE Ant (TWA 7) overlaid with surface brightness contours to help highlight the spiral arm first detected in the SPHERE observations (Olofsson et al., 2018). The red box defines the location of the spiral arm, which is only marginally detected in our GPI data. The white circle represents the size of the FPM, while the grey cross represents the location of the star.

disk is visible. It is also the second disk that is around an M-type star. The CE Ant disk is a very interesting case as it is one of only a few debris disks with observed multiple rings in scattered light and also exhibits a spiral arm (Olofsson et al., 2018; Ren et al., 2021): features that would otherwise be unobservable if the disk was higher inclined. Due to the FOV of GPI, we can only see the inner ring.

Because the entire disk is visible, we are able to fit the full disk geometry. While no eccentricity has been reported, we detect small offsets along both the major and minor axes of ∼0.86 au, leading to an eccentricity of 0.03. While this eccentricity is small, we do measure a significant brightness asymmetry, where the West side of the disk is ∼1.13 times brighter than the East side. This brightness asymmetry could be the result of an eccentric disk; however, given that the spiral arm is located on the West side, this may also be contributing to the surface brightness of the West extension. Although the spiral arm is not strongly detected in the GPI observations, likely due to being located towards the outer edge of the GPI's FOV, Figure 3.17 shows the location of the spiral arm which can be made out slightly using surface brightness contours.

While we detect a small eccentricity and modest brightness asymmetry, there are other reasons to believe that there are planets shaping the disk. For one, there is a stark inner clearing within ∼0.5″ (17 AU). Additionally the disk harbours multiple rings and a spiral arm, all of which are strong indications of one or more planets shaping the disk.

HD 30447

The GPI observations in this study, first published in Esposito et al. (2020), represents one of only two observations total of the HD 30447 debris disk. While these GPI observations are relatively low S/N compared to the rest of the sample, the disk is still better resolved in polarized intensity compared to previous HST observations (Soummer et al., 2014). From visual inspection, the disk appears to be highly inclined, with an inner clearing within $\sim$0.8″.

Measuring the disk geometry, we obtain a radius of 75.43 AU, an inclination of 81.47°, and a PA of 213.56°, consistent with measurements done in Esposito et al. (2020) within uncertainties. Interestingly, we find a clear disk offset along the major-axis of 6.53 au, bringing the star closer to the West side of the disk in the case of an eccentric disk. However, measuring the surface brightness between the East and West extensions, we find that East extension is 1.13 times brighter than the West extension, consistent with observations of the disk with HST (Soummer et al., 2014). If this surface brightness asymmetry is due to a pericenter glow (Wyatt et al., 1999; Pan et al., 2016), we would expect the offset along the major-axis in the opposite direction. When analyzing the surface brightness profile, the polarized intensity peaks between 0.75″ and 1.15″ from the star in the East extension, while the polarized intensity in the West extension peaks beyond 1.15″, suggesting the the East extension may indeed be closer to the star than the West extension. One explanation is that the derived offset could be the result of another geometrical asymmetry rather than an eccentric disk, or the data have too low S/N to properly constrain δ_x. Furthermore, more recent HST observations show the East side of the disk halo to be more radially extended than the West side (Ren et al., 2023), similar to the disk HD 111520 (discussed later in this Section), where the brighter and possibly closer side of the disk is more radially extended.

The HD 30447 debris disk appears to be perturbed in some manner; while the surface brightness suggests an eccentric disk with the East extension closer to the star, the disk geometry suggests the opposite. To learn more about the source of these asymmetries, multiwavelength and higher S/N observations are essential. A more in depth analysis of the disk halo as observed with HST, may also be helpful to understand the disk structure as a whole.

HD 32297

Like β Pic, the HD 32297 debris disk has been studied in great detail over the past two decades. Not only is it bright compared the majority of other disks in our sample, but it also has one of the strongest detections of gas emission (Donaldson et al., 2013; Greaves et al., 2016; MacGregor et al., 2018; Cataldi et al., 2020). In the optical, the disk halo can be seen, which extends to at least 1800 au (Schneider et al., 2014), and appears to have an interesting curved "moth"-like morphology. This morphology was originally thought to have been caused by an interaction with a dense portion of the interstellar medium (Debes et al., 2009), and is currently thought to be the result of planet-disk interactions (Lee & Chiang, 2016). Here we introduce the first observations of the disk in the J and $K1$ bands.

We compare our geometrical results with those from Duchêne et al. (2020), as they performed a similar ring model fitting to the vertical offset profile. We have, however, included two extra parameters, the PA and δ_y. While Duchêne et al. (2020) found no offset along the major axis, we find a significant offset of 4.6 au towards the East, bringing the West side of the disk closer to the star. To confirm this offset, we also fit a model to J-band observations, which has a similarly high S/N, and find that the vertical offset profile also exhibits a $\sim$4.6 au offset. Our results still lie within the 3σ upper limit on the eccentricity of 0.05 (Duchêne et al., 2020), as the derived offset leads to an eccentricity of 0.04.

Similar to past studies, we find no evidence of a significant brightness asymmetry in any of the three bands. We also find no evidence of an asymmetry in disk color, although the disk appears to be very blue in J-$K1$ and J-H, while being close to neutral in H-$K1$, as was similarly found in Bhowmik et al. (2019). This is likely caused by the drastic increase in surface brightness in the J band, compared to the H and $K1$ bands. In all, while the HD 32297 debris disk may have a slight offset along the major axis, the eccentricity of the disk is modest at most, and is otherwise axisymmetric.

HD 35841

The HD 35841 debris disk is a slightly more compact, highly inclined disk that has only been detected so far in the NIR and in the optical with HST (Soummer et al., 2014), although newer/higher resolution observations with HST have been presented in Ren et al. (2023). While an in depth study has been done already with the H band

data (Esposito et al., 2018), we present here the J- and $K1$-band data for the first time, allowing for a multiwavelength study.

For the disk geometry, we find a disk radius of 39.12 AU. Interestingly, this radius is within the estimated inner radius of 59.8 au based on radiative-transfer modelling (Esposito et al., 2018). Given the high inclination of 83° (slightly lower than the estimated inclination of 85° from Esposito et al. 2020), it may simply be that it is difficult to probe the inner radius. Therefore, it is possible that the minimum radius is actually closer to the star than what is determined with radiative transfer modelling. We also derive an offset along the major axis of ∼1 au towards the East extension, although, considering the S/N, this small offset is unlikely to be significant.

No significant brightness asymmetry is found, consistent with previous measurements (Esposito et al., 2018). Additionally, no disk color asymmetry is found between the East and West extensions. While Esposito et al. (2018) found a slight blue color between the H band and HST observations, between the J, H, and $K1$ bands, the disk presents a neutral color in polarized intensity. Overall, the HD 35841 debris disk is found to be axisymmetric.

HD 61005

HD 61005 is another well studied disk, with multiwavelength observations and an interesting morphology. In the optical, as observed with HST, the disk halo has a swept back morphology, giving it the nickname "the Moth" (Hines et al., 2007). This feature, similar to HD 32297, was originally thought to have been caused by an interaction with the ISM, although later simulations done by Lee & Chiang (2016) and Jones et al. (2023) show that this morphology can also be created by a planet-disk interaction and a recent giant impact. NIR observations with SPHERE and GPI also show a large brightness asymmetry, with the East side being twice as bright as the West side (Olofsson et al., 2016; Esposito et al., 2016). On the other hand, ALMA data show a millimeter belt that is fairly axisymmetric. Here we discuss the results from our multiwavelength GPI data.

Unfortunately, we do not detect the significant offset along the major axis detected with the SPHERE observations (Olofsson et al., 2016), which led to an estimated eccentricity of ∼0.1. Given that the SPHERE observations have a higher S/N compared to the GPI observations and that the disk extends beyond GPI's FOV, we may not have the sensitivity to detect this offset. We do, however, detect the brightness asym-

metry in all three bands, with the East extension being much brighter than the West extension. We find in the H band, which has the highest S/N out of the three bands, that the East side is $\sim$1.6 times brighter than the West side. This brightness asymmetry is much greater in the J and $K1$ bands, where the East side is 6.3 and 2.6 times brighter, respectively. However, its important to note that these two observations are relatively low S/N, and therefore these brightness asymmetry measurements may not be exact. In addition to a large surface brightness asymmetry, we also find a significant color asymmetry over 3σ in J-H and J-$K1$ between the two sides of the disk. All three measurements show a distinctly blue disk color, which is consistent with past measurements (Esposito et al., 2016).

Whether or not these asymmetries are associated with an interaction with the ISM, a planet-disk interaction, or another source has been highly debated. Both an interaction with the ISM and a planet on an eccentric disk could cause the moth-like wings seen in the disk halo (Debes et al., 2009; Esposito et al., 2016). An ISM interaction could also cause the disk color asymmetry, with the East side being more blue than the West side. A recent collision between two large objects may also cause the observed brightness asymmetry and tentative disk color asymmetry, however, ALMA observations do not show any significant clumps, and no gas disk is detected (Olofsson et al., 2016; MacGregor et al., 2018). In this case, planet-disk interactions or an ISM interaction are more likely scenarios, as a combination of the two could cause the majority of asymmetries seen, such as the moth-like halo, brightness asymmetry, eccentricity, and possibly a disk color asymmetry. While, the mm-observations appear to be axisymmetric, residuals in the best fitting models employed by MacGregor et al. (2018) suggest that the millimeter sized grains may indeed have some eccentricity, although this would require detection of the star to confirm.

HD 106906

The HD 106906 debris disk system is the only debris disk in our sample with a massive, directly imaged planet orbiting *outside* of the disk (11 M_{Jup}, 735$\pm$5 AU; Bailey et al. 2014; Daemgen et al. 2017). The disk itself appears perturbed, with a moderate brightness asymmetry seen in scattered light with GPI, SPHERE, and HST (Kalas et al., 2015; Lagrange et al., 2016), and most recently has been found to have a significant eccentricity (Crotts et al., 2021). Additionally, HST observations show that the outer disk halo is radially asymmetric, where the NW extension extends

significantly farther than the SE extension in a "needle"-like fashion (Kalas et al., 2015). Although the origin of the planet is still debated, what is clear is that the disk's asymmetries align with being perturbed by the outer planet on an eccentric orbit.

While our geometrical fitting agrees mostly with the analysis done in Crotts et al. (2021), we derive a slightly larger disk radius and δ_x of 107 au and 20 au compared to 104 au and 16 au, respectively. This may be due to the unique shape of HD 106906's disk spine as it has a distinct "S" shape. This "S" geometry can be caused by either an eccentric disk or other geometrical asymmetry such as a warp, however, given that there is no detected warp, this led to the conclusion that the disk is rather eccentric. In terms of our simple ring modelling, it is clear that the "S" shape of the disk geometry can be fit well with multiple different models; however, either way a large offset along the major axis is always required. Keeping a lower limit on the eccentricity of 0.16 as set by Crotts et al. (2021) still makes it one of the most eccentric disks in our sample.

We also confirm the brightness asymmetry in all three bands. This brightness asymmetry is very modest given the large eccentricity; however, as Crotts et al. (2021) shows, the SPF for an eccentric disk can offset the expected brightness asymmetry based solely on the radial separation of the disk from the star. In terms of the disk color we find the disk has a blue color that becomes increasingly grey at longer wavelengths, consistent with the findings in Crotts et al. (2021). Similarly, we do not find a significant color asymmetry.

HD 110058

The HD 110058 debris disk is one of the most asymmetric disks in our sample. Along with GPI, HD 110058 has been also imaged with HST, SPHERE, as well as with ALMA (Ren et al., 2023; Kasper et al., 2015; Stasevic et al., 2023; Hales et al., 2022). In scattered light, a definite warp has been detected towards the outer edges of the disk (Kasper et al., 2015; Stasevic et al., 2023), reminiscent of the warp detected in the outer regions of the HD 111520 debris disk (Crotts et al., 2022), and also similar to the warp featured in Beta Pic (Heap et al., 2000). While perturbation from a planet companion is a strong candidate for this warp, no planets yet have been detected.

While the disk's warp has only been seen so far in total intensity observations, we are also able to detect it in polarized intensity, which we highlight in Figure 3.18.

We find the warp to occur beyond 0.35″ or 40 AU, as well as find the South-East warp to have an angle of ∼15°, similar to what has been found in previous studies (Kasper et al., 2015). From our geometrical fitting, we find that the MCMC favors two slightly different models: a disk with a 5 au offset towards the East extension and a disk with an 8 au offset towards the West extension. While these are contrasting models, the model with the 8 au offset has a much higher log likelihood and therefore we use this offset to estimate the eccentricity of $\gtrsim$0.13. This is a significantly high eccentricity, and is in contradiction to the low eccentricity ($e < 0.035$) estimated in Kasper et al. (2015) based on SPHERE data. It is possible that this offset along the major-axis is a result of the asymmetric geometry due to the warp rather than the disk being eccentric.

When looking at the brightness asymmetry in all three bands, we find an interesting trend. While no significant brightness asymmetry is seen in the $K1$ band, there is a significant brightness asymmetry in the J and H bands. In the J band, the East extension is 1.7 times brighter than the West extension, however, in the H band, the East extension is only 1.2 times brighter than the West extension, meaning that the brightness asymmetry is most significant at shorter wavelengths. This may be a result of dust grain properties, as we also find a significant disk color asymmetry between the J and H bands, where the East extension is relatively more blue than the West extension. This may suggest that the dust grain properties (such as minimum size, composition and/or porosity) or the distribution of dust grains are in some way being altered. In general, the disk exhibits a strong red color between all three bands, suggesting a larger minimum dust grain size on the order of one to several microns, assuming a porosity of zero (Boccaletti et al., 2003). This is consistent with the 2 μm blowout size for the system.

In summary, the HD 110058 debris disk serves as a very interesting candidate for further investigation. The disk is clearly being perturbed by some mechanism. While a planet is a likely candidate for the observed warp and possible eccentricity, further work is required to understand if perturbation from a planet is enough to create a disk color asymmetry, or if another mechanism is needed.

HD 111161

The HD 111161 debris disk is one that has not yet been studied in great detail. From visual inspection, the disk appears to be a lower inclined ring that is highly forward

Figure 3.18: **Top:** Vertical offset profiles of HD 110058 and HD 115600, which show tentative warps in their vertical offset profiles. **Bottom:** HD 115600 overlaid with surface brightness contours to help highlight the warp detected in the vertical offset profile beyond 0.4″. The red solid line represents the vertical offset profile derived in Section 3.2.1 and plotted above. The red dashed line represents an extension of the warp to show the angle of the warp on both sides of the disk. The white circle represents the size of the FPM, while the grey cross represents the location of the star.

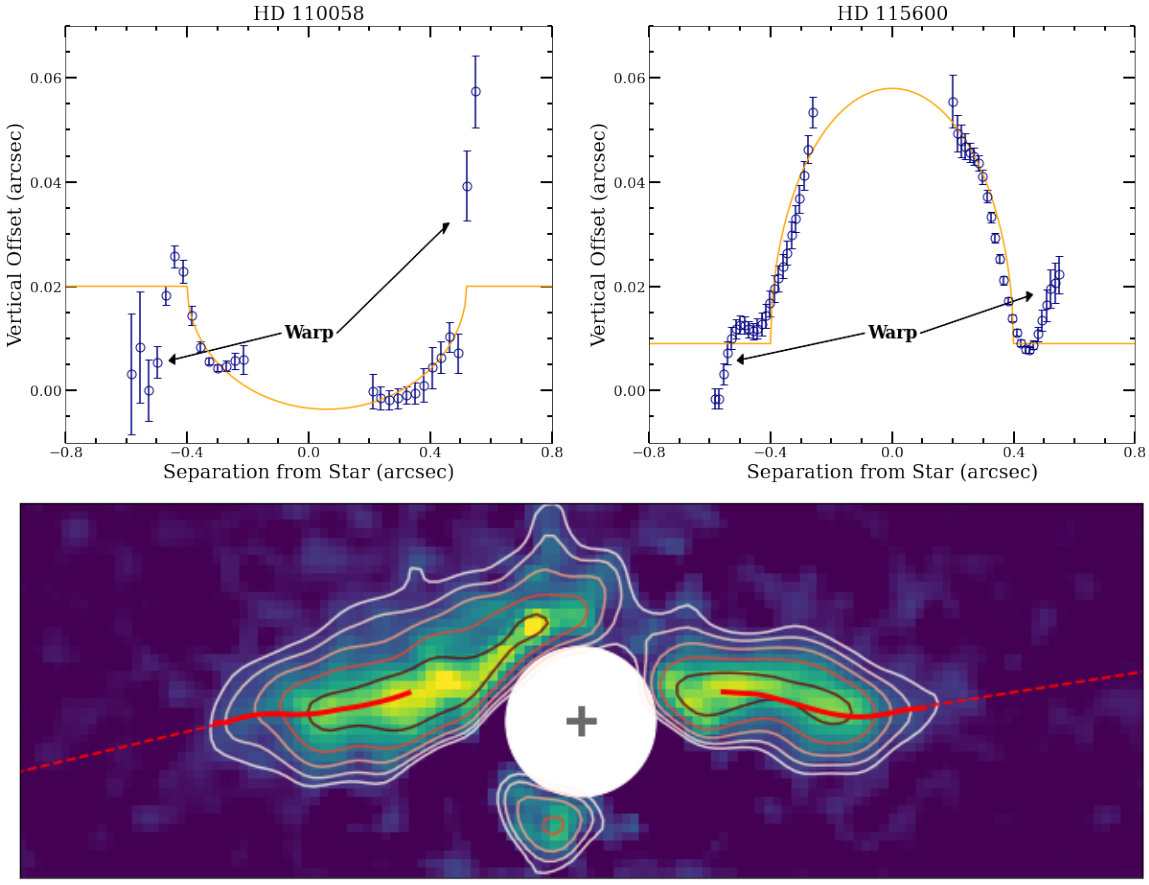

scattering, as only the front side of the disk is visible. There is also a cleared gap within the disk's inner radius.

Comparing our disk geometry results to previous measurements, we find a disk radius of ∼72.5 au, which is consistent with the estimated inner radius of $71.4^{+0.5}_{-1.05}$ au (Esposito et al., 2020). We find a PA of ∼83.3°, which is also similar with previous measurements done in Esposito et al. (2020) using radiative transfer modelling ($83.2^{\circ+0.5}_{-0.6}$), while our derived inclination is slightly lower (∼59.8° compared to $62.1^{\circ+0.3}_{-0.2}$). Our geometrical fitting does favor a slight disk offset along both the major and minor axes of 1.4 au and 0.66 au, however, these observations are relatively low S/N.

Estimating the brightness between the East and West extensions, we find no evidence of a significant brightness asymmetry within 3σ, which is consistent with small to no disk offset. Unfortunately, this disk only has H band data, meaning that we were unable to perform disk color measurements.

HD 111520

The HD 111520 debris disk is one that presents multiple different asymmetries. Previous studies have shown the disk to have a large brightness asymmetry, radial asymmetry, disk color asymmetry, as well as a warp at 1.7″ from the star and a bifurcation feature on the West side of the disk (Padgett & Stapelfeldt, 2015; Draper et al., 2016b; Crotts et al., 2022). While we are performing a similar analysis on the GPI J-, H- and $K1$-band polarimetric observations as Crotts et al. (2022), the analysis presented here allows us to compare the HD 111520 disk to the rest of the disks in our sample.

Comparing our geometrical fitting with the same fitting done in Crotts et al. (2022), we come to similar conclusions. While the disk radius is still difficult to constrain given the high inclination of the disk, we get a consistent result with a disk radius of 91.4 au or ∼0.84″. Again, similar to Crotts et al. (2022), we find that an offset along the major-axis is also difficult to constrain and is consistent with zero. Our derived inclination of 89.5° is slightly higher than what was measured previously for the H band, however, it still is consistent with the disk being less than 2 degrees from edge on.

Within our sample, the disk has one of the highest brightness asymmetries in all three bands, ranging from a right/East brightness ratio of ∼1.4:1 to 1.8:1. Similar to Crotts et al. (2022), we find the disk to present a strong blue color between all

three bands. While we do measure a disk color asymmetry, this asymmetry is only significant by 2σ.

HD 114082

HD 114082 is the most recent system to have a resolved debris disk and a known planet (Engler et al., 2022; Zakhozhay et al., 2022). Similar to AU Mic, the planet has been observed via the transit and radial velocity method, where the planet found has a mass of 8 M_{Jup}, orbits at a distance of 0.51 au, and has a possible large eccentricity of 0.4 (Zakhozhay et al., 2022). The disk lies much farther out from the star compared to the planet, and is fairly compact, similar to the HD 110058 disk.

With the higher S/N $K1$-band data, we find the disk to have a radius of ∼28.5 au, which is consistent with the inner radius estimated of $28.7^{+2.9}_{-3.7}$ (Wahhaj et al., 2016). Engler et al. 2022). We also derive a small offset of 3 au (0.03″) along the major axis, bringing the West side of the disk closer to the star, however this is roughly twice as large as the 2σ offset placed by Wahhaj et al. (2016). Additionally, no significant offsets are found using SPHERE observations (Engler et al., 2022).

For the surface brightness, we find no significant brightness asymmetry in the H band. However, we do find a small but significant brightness asymmetry in the K band, with the East side being 1.13 times brighter than the West side, in contrast to the derived offset from the geometrical fitting, suggesting that the measured offset may not be due to an eccentric disk. A similar finding was observed in the SPHERE data, where Engler et al. (2022) reports a brightness asymmetry in the K-band IRDIS observations, but not in the H-band IRDIS observations. While this brightness asymmetry is thought to be a result of istrumental noise, the fact that it is also observed with GPI suggests that this feature may be real. Along with the brightness asymmetry, a small color asymmetry is also observed in $H - K1$ where the East side is relatively more red than the West side, however, this asymmetry is only significant within 2σ.

While this system has a known planet, the planet is too close to the star to be dynamically coupled with the disk (0.5 au compared to 25 au). On the other hand, the disk has one of the highest vertical aspect ratios in our sample, similar to the HD 110058 debris disk which may indicate stirring from another companion closer to the disk.

HD 115600

Previous studies of the HD 115600 disk with GPI and SPHERE have shown the disk to be asymmetric with a moderate to high eccentricity, although this is mainly based on total intensity observations (Currie et al., 2015; Gibbs et al., 2019).

In polarized intensity we find no disk offset along the major-axis, suggesting that the disk is not eccentric. We do, however, detect a tentative warp in the disk geometry, where the the East extension bends downwards beyond 0.4″, while the West extension bends upwards beyond 0.4″ (see Figures 3.18). This is very similar to the HD 110058 debris disk, which hosts a similar warp, while not being necessarily eccentric. This may explain why the disk was found to be highly eccentric in Currie et al. (2015), who performs a similar geometrical analysis, as an asymmetric geometry, such as a warp, can translate into a significant offset that can be interpreted as an eccentric disk. Further observations, such as with HST, can help confirm the existence of this warp.

We find no surface brightness asymmetry between the East and West extensions in any of the three bands, supporting the findings of a non-eccentric disk. We also find no asymmetry in the disk color between the two sides of the disk. The overall disk color in J-$K1$ and J-H are strongly blue, with values between -0.6 and -1, while in H-$K1$ the disk color jumps to red, somewhat similar to the HD 32297 disk. This large jump in disk color, from strongly blue to red, is discussed in Section 3.3.3.

HD 117214

The HD 117214 debris disk has been described as axisymmetric, with no asymmetries currently reported in the literature. While the disk has not been found to be eccentric, we do find a very small offset along the major-axis of ∼0.19 au, but it is consistent with 0 au within 2σ. Overall, the disk geometry is in line with being axisymmetric, as has been observed in (Engler et al., 2020). Despite the axisymmetric disk geometry, we do find a significant brightness asymmetry where the West side is ∼1.15 times brighter than the East extension. This brightness asymmetry is unlikely to be due to a pericenter glow as we find no significant disk offsets. Multiwavelength observations in the future will be useful to help confirm this brightness asymmetry and better understand what mechanisms are prevalent in the disk.

HD 129590

The HD 129590 debris disk, is one of the few disks around a G-type star that has been found to harbor a detectable amount of gas (Kral et al., 2020). Along with low resolution ALMA observations, the disk has also been observed in the H and YJ bands with SPHERE IRDIS and IFS (Matthews et al., 2017). Here, we present the first $K1$-band observations, along side H-band polarimetric observations with GPI.

Analyzing the geometry, we find a disk radius of 45.5 au, which is smaller than the estimated R_0 of 66.9 au, and may be closer to the inner radius which is estimated to be <40 au (Matthews et al., 2017). We also find the inclination is much higher than the estimated inclination of ∼75° based on total intensity SPHERE data in Matthews et al. (2017). However, modelling done in Olofsson et al. (2022) find a more comparable inclination of 82°. The disk spine fitting does support a small offset along the major axis of ∼1.9 au, placing the star closer to the West extension, although such an offset has no precedent in the literature.

Comparing the surface brightness between the H and $K1$ bands, we find the disk to be brighter in the $K1$ band and find the disk to have a red color. While no significant brightness asymmetry is found in the H band between the East and West extensions, we do find that the East side of the disk is about 1.1 times brighter than the West side in the $K1$ band. This brightness asymmetry is contradictory to the offset measured in our geometrical fitting, and we additionally find no significant color asymmetry.

HD 131835

The HD 131835 (HIP 73145) debris disk is another disk in our sample with strong CO detections. This gas disk is co-located with the dust disk, and is found to likely arise from secondary origins (Kral et al., 2019; Smirnov-Pinchukov et al., 2022). The dust disk is moderately inclined and appears to have an inner gap within ∼75 au, with evidence for two inner/warmer rings (Hung et al., 2015a; Feldt et al., 2017). In this study, we reanalyze the GPI H-band observations first presented in Hung et al. (2015b).

Through the disk geometry, an offset of 4.6 au is detected along the major-axis, bringing the star closer to the West extension and leading to a minimum eccentricity of 0.05. However, such an offset/eccentricity is not reported for other observations, and Hung et al. (2015b) ruled out an eccentricity of >0.2 at 1σ. Therefore, if the

disk is indeed eccentric, it is not likely to be significantly greater than 0.05. The HD 131835 disk is also reported to be radially broad (Hung et al., 2015b), and has relatively low S/N in our GPI observations, meaning that our narrow ring model may not be the best method for deriving disk offsets. Additionally, the disk has been found to possibly consist of three concentric rings (Feldt et al., 2017), further complicating the overall disk geometry. See Section 3.5.4 at the end of the Appendix for further analysis related to multiple rings in the system.

In agreement with Hung et al. (2015b), we also find a brightness asymmetry with the East extension being brighter than the West, although we find this asymmetry to be larger at 1.7:1 compared to 1.3:1 when averaging the flux over our selected apertures. This brightness asymmetry appears only in the *GPI* polarized intensity data, as SPHERE observations do not show a similar brightness asymmetry (Feldt et al., 2017), however, this difference may be due to disk self-subtraction, introduced by the PSF subtraction process, as the SPHERE observations are in total intensity. Longer wavelength observations with ALMA also appear axisymmetric, although the disk is not well resolved (Feldt et al., 2017). Additionally, a brighter East extension contradicts the measured disk offset which places the star closer to the West extension, assuming the offset is due to eccentricity. Future, higher resolution imaging will be useful to confirm the observed brightness asymmetry.

HD 145560

The HD 145560 system harbors a lower inclined debris disk, which can be described as a narrow ring with an inner clearing within 68 au. As of now, the disk has only been imaged with GPI and with low-resolution ALMA observations, making it one of the less studied disks in our sample. We compare our results with another analysis done using the same GPI H-band data (Esposito et al., 2020; Hom et al., 2020).

While other studies used radiative transfer modelling to derive disk geometrical properties, we use our radial offset fitting. We derive a disk radius of 81.2 au, which is located near R_0 measured in Esposito et al. (2020) of 85.3 au. We also derive an inclination of 41.9° and a PA of 39.5°. Both these values are slightly smaller than the measurements derived from radiative transfer modelling (Esposito et al., 2020; Hom et al., 2020) of 43.9° and 41.5°, but are still consistent within 2σ uncertainties. Our model prefers a small offset along the major-axis of $\sim$0.86 au, leading to a small eccentricity of $>$0.01. However, we do derive a larger offset along the minor-axis of

3.3 au, which brings the estimated eccentricity up to ∼0.04. We otherwise find the disk to be axisymmetric, with no brightness asymmetry measured in the H band, which would be expected for the derived small offset along the major-axis.

HD 146897

The HD 146897 system, also well-known as HIP 79977, harbours a highly inclined debris disk that has also been observed with SPHERE and SCExAO on the Subaru telescope (Thalmann et al., 2013; Engler et al., 2017; Goebel et al., 2018).

In Engler et al. (2017), radiative-transfer modelling was used to determine properties of the HD 146897 disk, comparing two different models: One with a disk radius of 70 au, and one with a disk radius of 40 au. While the disk model with a radius of 70 au was found to be a better fit to the data, we derived a disk radius of ∼52 au which is more consistent with the measured R_0 of 53 au derived in Goebel et al. (2018). Moreover, we find a significant offset along the major-axis of 6.3 au, placing the star closer to the West extension. Considering a disk radius of 52 au, this offset leads to a disk eccentricity of at least 0.12, which is a significant eccentricity compared to the majority of our sample. While previous observations do not report any eccentricity, 0.12 is still consistent with the upper limit of the eccentricity as set by Thalmann et al. (2013) of e≤0.16.

Although Goebel et al. (2018) found the East extension to be brighter than the West extension in total intensity, our polarized intensity shows the West side to be moderately brighter than the East in the J and H bands with a brightness asymmetry of 1.08 to 1. The reasoning for this difference could be an artifact from disk self-subtraction with total intensity observations. Taking into account the derived disk offset along the major-axis, an eccentric disk with the West side closer to the star is more consistent with the measured brightness asymmetry. While a 1.08:1 brightness asymmetry is small considering an eccentricity of 0.12, one explanation could be similar to HD 106906, where the SPF partially cancels out the brightness asymmetry caused by a $1/r^2$ relationship.

With our multiwavelength observations, we find that the disk changes color when going from short to longer wavelengths. While a red disk color is measured in J-H, a neutral color is measured in J-$K1$ and a blue color in H-$K1$. the HD 146897 disk is the only one in our sample to exhibit this behavior in disk color. When comparing the disk color between the East and West side of the disk, we do not measure a significant

disk color asymmetry between any of the three bands.

This analysis reveals an interesting side of the HD 146897 debris disk. While previous studies depicts the disk as being fairly axisymmetric, our results suggest that the disk morphology may actually be more complicated. Fitting the vertical offset or disk spine suggests an eccentric disk, or at the very least, an asymmetrical disk geometry. Measuring the surface brightness also reveals conflicting information with previous observations, suggesting a brighter West side rather than a brighter East side, although this would be more consistent with our derived offset along the major-axis in the case of an eccentric disk.

HD 156623

HD 156623 is another debris disk system that is rich in gas; however, the high density of gas leads to the speculation that this disk may be a "hybrid", where the gas may be partially of primordial origin, i.e., a remnant of the protoplanetary disk phase (Kóspál et al., 2013). In this study, we are analyzing the first scattered light observations of the disk taken in the H band and first presented in Esposito et al. (2020).

We compare our empirical results for the disk geometry to the results from Esposito et al. (2020) who uses radiative-transfer modelling. We derive a disk radius of $\sim$52.6 au, which lies within the derived critical radius, r_c, of 64.4$\pm$1.8 au (Esposito et al., 2020), where r_c is the radius where the disk transitions from a dust density power law of α_{in} to α_{out}. While our inclination is consistent with previous measurements ($\sim$34.7° compared to $34.9^{\circ}{}^{+3.6}_{-9.5}$), our estimated PA is slightly higher (102.9° compared to $100.9^{\circ}{}^{+1.9}_{-2.2}$); however, these values are still consistent within 2σ uncertainties. A small disk offset is measured along the major-axis of 2.1 au, leading to an eccentricity of $\gtrsim$0.04 and bringing the East side of the disk closer to the star. An additional offset is measured along the minor-axis of 1.68 au, which when taken into account, increases the eccentricity to $\sim$0.08. However, these offsets may be exaggerated given that the disk appears radially broad, with no gap observed outside of the FPM, we therefore place an eccentricity of 0.08 as an upper limit.

Measuring the surface brightness reveals a moderate brightness asymmetry, where the East side of the disk is 1.11 times brighter than the West side. This is consistent with the small offset measured, which places the star closer to the East extension, possibly causing a slight pericenter glow (Wyatt et al., 1999). Further scattered light observations will be useful to help confirm these asymmetries.

Figure 3.19: HD 157587 observations in all three bands, overlaid with surface brightness contours to highlight the difference in the vertical width between the East and West extensions at each wavelength. The white circles represent the size of the FPM, while the grey crosses represent the location of the star.

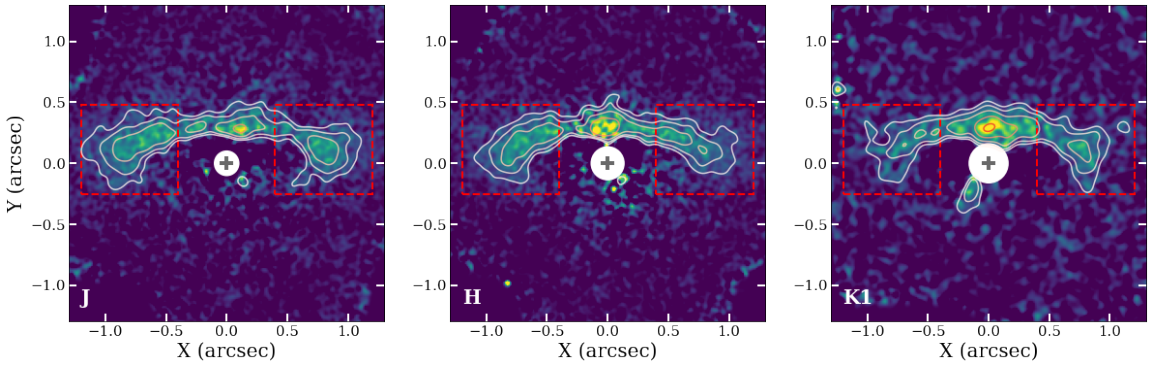

HD 157587

The HD 157587 debris disk is the oldest system in our sample with an estimated age of 165-835 Myr. So far, the disk has only been observed with GPI and HST, where only the H-band observations have been fully analyzed (Millar-Blanchaer et al., 2016). In this study we include the J- and $K1$-band observations, adding a multiwavelength and disk color analysis.

Through our geometrical fitting, we derive an inclination that is several degrees smaller than found in previous studies (64° compared to ∼68-72°; Millar-Blanchaer et al. (2016)). While Millar-Blanchaer et al. (2016) found evidence for an offset along the major-axis placing the East side of the disk closer to the star by ∼1.6±0.6 au, our ring model fitting does not find strong evidence for such an offset (Our results suggest a 0.65 au offset in the opposite direction). The reason for this inconsistency may be an asymmetric disk morphology not related to eccentricity. In the case of HD 157587, we find that the East side of the disk is vertically broader than the West side of the disk, where the weighted average FWHM for the East side is roughly 0.04″ (4 au) greater than the weighted average FWHM for the West side in the H band. This discrepancy may have led to an offset along the major-axis in the radial offset profile using our method. We also plot the image of HD 157587 in each band, overlaid with surface brightness contours, to visually show this difference in the vertical FWHM in Figure 3.19.

Similar to Millar-Blanchaer et al. (2016), we also measure a brightness asymmetry in the disk, with the East side being moderately brighter than the West side. Our

brightness asymmetry measurements in the H band of 1.13±0.05 is consistent to previous measurements of 1.15±0.02 (Millar-Blanchaer et al., 2016). Conducting the same measurements in the J and $K1$ bands, we find the brightness asymmetry to be even stronger in the J band of 1.22±0.03, whereas the $K1$ band does not show a significant brightness asymmetry within 2σ. This brightness asymmetry may partially be due to the difference in vertical width between the East and West extensions, as this feature is most prominent in the J and H bands, while less prominent in the $K1$ band (see Figure 3.19). If the brightness asymmetry is indeed due to an eccentric disk, it is most likely that the offset along the major-axis is towards the opposite direction than what is measured in this study.

While overall the disk presents a blue to neutral disk color, the East side of the disk is tentatively bluer in H-$K1$ and J-H, while being significantly bluer in J-$K1$. If there are asymmetries in the dust grain properties, this may provide an alternate explanation for the brightness asymmetry.

HD 191089

The HD 191089 debris disk consists of a dust ring from ∼26 to ∼78 au, and an extended halo out to 640±130 au as observed with HST (Ren et al., 2019). The disk has been observed at multiple wavelengths, from the optical with HST, to the sub-mm with ALMA (Soummer et al., 2014; Ren et al., 2019; Churcher et al., 2011; Kral et al., 2020). Along with the already published H-band observations (Ren et al., 2019; Esposito et al., 2020), we also include J-band observations in our analysis.

We derive a disk radius of ∼47 au, which is close to the derived R_0 from radiative transfer modelling of the GPI H-band observations (43.9±0.3 au; Ren et al. 2019), as well as the radius derived from mm observations (43.4 au; Kral et al. 2020). Similarly, we do not detect a significant offset along the major or minor axis, in agreement with the results from Ren et al. (2019), however, a small offset of 1 au is measured along the major-axis.

We find no significant brightness asymmetry present in either bands. Calculating the disk color shows that the disk presents a strong blue color in J-H, meaning that dust grains are more efficient at scattering light at shorter wavelengths. We find no disk color asymmetry between the two extensions, further supporting a fairly axisymmetric disk.

HR 4796 A

The HR 4796 A debris disk is one of the most well studied disks in our sample. The disk is a bright and a distinctly narrow ring, permitting the measurement of a complete SPF compared with other debris disks (e.g. Milli et al. 2017, 2019). Given that the disk is already well characterized, we use our polarized H-band GPI observations simply as a confirmation of the disk geometry and surface brightness.

We find a disk radius of ∼77.7 au, which is consistent with previous measurements using a similar geometrical fitting (e.g., Chen et al. 2020). While the disk is known to be eccentric, ranging from 0.01 to ∼0.08 depending on the observation and reduction method (Perrin et al., 2015; Milli et al., 2017, 2019; Olofsson et al., 2019, 2020; Chen et al., 2020), with our GPI polarized intensity observations, the derived offset along the major-axis and resulting eccentricity are on the smaller end with an offset of 0.58 au and eccentricity of $\gtrsim$0.01. Including the 1.56 au along the minor-axis leads to an estimated eccentricity of ∼0.02st, which is still on the low end of measured eccentricities for the HR 4796 A disk.

Measuring the surface brightness of the disk as a function of stellar separation, the surface brightness peaks close to the star, followed by a second peak at the disk ansae before decreasing towards the back side of the disk. Placing several square apertures along the East and West extensions, we confirm a modest brightness asymmetry, where the East extension is ∼1.17 times brighter than the West extension, most of which comes from near the East disk ansae.

HR 7012

The HR 7012 (also known as HD 172555) debris disk is one of the warmest and most radially compact disks in our sample, extending only ∼0.1″ past the FPM. The disk appears to be in a state of heavy bombardment, with strong traces of both SiO and CO (Lisse et al., 2008; Schneiderman et al., 2021), along with indirect and direct detections of exocomet transits (Kiefer et al., 2014, 2023). Here, we compare our analysis of the disk morphology using GPI H-band observations to previous analysis using SPHERE/ZIMPOL observations (Engler et al., 2018).

We derive a disk radius of 8.8 au, consistent with SPHERE/ZIMPOL measurements of R_0 within 1σ derived from a grid model (10.3±1.7 au) and within 2σ derived from a radiative-transfer model (11.3±1.7 au; Engler et al. 2018). This measurement is also consistent with the measured inner radius of 8±2 au (Engler et al., 2018).

Figure 3.20: **Top:** The FWHM profile as a function of stellar separation for the HD 131835 disk. **Bottom:** Vertical Offset profile for the HD 131835 disk, also shown in Figure 3.5. The inner two orange shaded regions show the locations of the disk gaps found in Feldt et al. (2017), with the addition of a possible additional gap outside the two already known gaps found in this work.

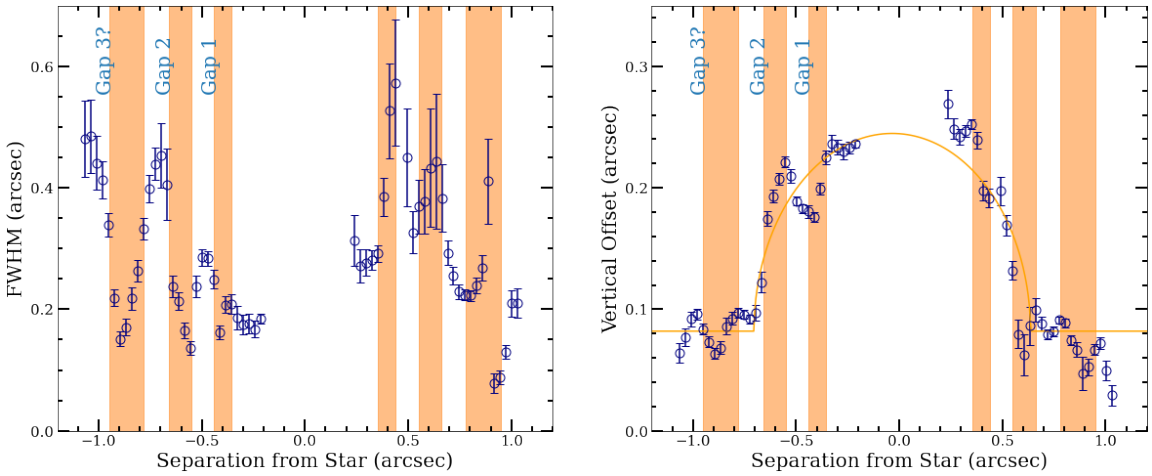

While Engler et al. (2018) find the disk to be axisymmetric, the GPI observations appear to tell a different story. Fitting the vertical offset profile shows a relatively large offset along the major-axis of 2.76 au, which would mean the disk is highly eccentric with e$\gtrsim$0.31. Given that the disk sits very close to the FPM, this asymmetric geometry may simply be due to residual noise close to the star.

This is supported by the surface brightness profile and brightness asymmetry, where the surface brightness profile decreases symmetrically from the star out to $\sim$0.4″ within 1σ uncertainties. Additionally, averaging the flux over rectangular apertures placed on the highest S/N regions of the disk yields no significant brightness asymmetry within 2σ. While the disk may not be as asymmetric as it would appear from the polarimetric GPI observations at first glance, the disk does have the 3rd highest vertical aspect ratio in our sample due to the disk being so compact. This may be the result of the stellar companion, CD-64 1208, located >2000 au from HR 7012 (Torres et al., 2006), which could cause the disk to become truncated depending on its orbit. However, given the large separation of the stellar companion, it would be difficult to confirm if this is the case.

3.5.4 HD 131835: Multiple Rings?

Using total-intensity SPHERE/IRDIS observations in the H band, Feldt et al. (2017) discovered that the HD 131835 disk consisted of several concentric rings, features which are often very difficult to detect in higher inclined disks ($i = 75 - 76°$). Using the H-band polarized intensity GPI observations, we look at the vertical structure to see whether or not these rings are still present in our data.

In Figure 3.20, we re-plot the vertical offset profile, along side the vertical FWHM as a function of stellar separation. We then plotted orange bars to represent the locations of the gaps found in Feldt et al. (2017), which were found at 46-57 au ($\sim$0.36″-0.44″) and 71-85 au ($\sim$0.55″-0.66″). Doing so we find that the locations of these gaps strongly co-align with dips in the vertical FWHM, as well as the vertical offset. In addition to the two inner gaps discovered in Feldt et al. (2017), we find a possible third outer gap located between $\sim$101 au and 123 au (0.78″-0.95″), where another dip in the vertical FWHM is observed. This dip in the vertical FWHM also coincides with a dip in the vertical offset at the same location on either side of the disk. This gap is outside the outer ring observed with SPHERE, although, as these are total intensity observations, it is possible that additional structure outside the outer ring was subtracted during the PSF subtraction process. While we cannot definitively say whether or not this is a physical gap, the fact that the location of the two inner gaps found in Feldt et al. (2017) align with dips in both the vertical FWHM and vertical offset, help to confirm that these structures are real.

In terms of other high inclined disks, whether or not the vertical FWHM and vertical offset profiles can be used as probes for multiple rings/gaps is unclear without further evidence. Wavy patterns in either profile could arise from other factors such as low S/N, and therefore may not be indicative of more complex structure. Further analysis is required to explore the connection between the vertical structure and evidence of rings/gaps, although this is outside the scope of our study.

Chapter 4

Further Characterization of the Highly Asymmetrical HD 111520 Disk

In Chapter 3, I performed a uniform empirical analysis on a large, multiwavelength sample of debris disks observed with GPI in polarized intensity. The goal of this analysis was to identify any disk asymmetries and/or structures that would suggest perturbation from a planet. While we find that a majority of disks harbour such an asymmetry or structure, additional work and possible followup is required to confirm whether these features are truly associated with planets. I therefore have selected one of the most asymmetric disks from the GPI sample, HD 111520, for further analysis, in order to obtain an even deeper understanding the disk's morphology and whether or not planet-disk interactions are at play. For reference, this work is published in the Astrophysical Journal under Crotts et al. (2022).

4.1 The HD 111520 System

HD 111520 (HIP 62657) is located 108.1±0.2 pc from the Sun (Gaia Collaboration et al., 2021) and is a member of the Lower Centaurus Crux (LCC) group within the Scorpius-Centaurus Association (de Zeeuw et al., 1999). As part of the GPIES campaign (Macintosh et al., 2018, 2014, 2008), which resolved 26 debris disks in polarized and total intensity (Esposito et al., 2020), one of the systems observed was HD 111520. The debris disk was detected in the H band and revealed a strongly asymmetric disk morphology from 0.3-1″, with a 2:1 brightness asymmetry and radial asymmetry measured between the two sides of the disk (Draper et al., 2016b). From Hubble Space Telescope (HST) observations, the system had previously been shown

Table 4.1: Summary of the data used in this paper. The H Spec data is the same data from Draper et al. (2016b), while the H Pol data (previously published in Esposito et al. 2020) was a subsequent longer observation (582 s vs. 2840 s integration time). Here, N = the number of frames, t_{int} = the total integration time in seconds, and ΔPA = the total parallactic angle rotation in degrees.

Band	Mode	Date	N	t_{int} (s)	ΔPA (°)	MASS Seeing (″)
J	Pol	2016 Mar 26	58	3480	39.1	0.82
J	Spec	2016 Mar 27	51	3060	29.5	0.45
H	Pol	2016 Mar 18	26	2840	28.3	0.48
H	Spec	2015 Jul 02	41	2446	34.8	0.28
K1	Pol	2016 Mar 28	36	2160	35.8	1.33
K1	Spec	2016 Mar 24	30	1800	19.2	0.59

to have an asymmetric, "needle"-like disk structure out to 6″ (∼650 AU) relative to the central star, along with an even larger 5:1 brightness asymmetry and a bifurcation feature in the Northern extension (Padgett & Stapelfeldt, 2015). Such a strong asymmetry could be the result of two main scenarios, either the dust grain properties are significantly different between the two extensions, which changes the dust scattering efficiency, or the planetesimal belt itself is being perturbed by dynamical activity, such as that which could result from an unseen planetary companion.

Since HD 111520 is such an unusual system, we use the multiwavelength data from our uniform analysis of the GPI debris disks, alongside multiwavelength total intensity and HST/STIS observations, to better characterize the disk morphology and further investigate its observed asymmetry. We conduct a similar analysis as in Chapter 3, measuring the disk structure in Section 4.3.1, as well as the surface brightness profiles of each band and disk color in Section 4.3.2. Additionally, in Section 4.3.3, we analyze the structure of the disk halo as observed with HST/STIS. We then discuss possible explanations for the disk's asymmetries based on the results of our empirical analysis in Section 4.4.

4.2 Observations and Data Reduction

The imaging of HD 111520 from GPI was collected over a range of nights, where observations were taken in both polarimetric and spectroscopic modes. A summary of the observations can be seen in Table 4.1. In general, the observations were scheduled to maximize field rotation as the source transited the meridian, with a total observing

sequence of around an hour (including overheads) with a series of 60 second exposures to optimize PSF subtraction. The H-band polarization mode data set, previously published in Esposito et al. (2020), is a longer integration time than the data presented in Draper et al. (2016b), therefore achieving a higher signal-to-noise ratio (S/N), comparable to the other bands.

Again, the data reduction process can be found described in Chapter 2, however, we describe the reduction process of the total intensity data here. Similar to data reduction in polarization mode, in the case of the spectroscopic mode, standard GPI pipeline data reduction practices are used (Perrin et al., 2014b). Each of the individual dispersed light frames were dark subtracted, had bad pixels masked, and were 'destriped' from microphonics (Ingraham et al., 2014). Wavelength calibrations are done using Ar lamp exposures in each respective band (Wolff et al., 2014). Calibration sources are measured prior to the observing sequence, minimizing flexure offsets. For the J and H bands a standard box aperture method is used to extract the flux into a wavelength calibrated data cube (Maire et al., 2014a). In the $K1$ band, the satellite spots had weaker flux compared to the background, which interferes with the calibrations necessary after cube extraction. The microlens PSF extraction method was then used to extract the data from the detector (Draper et al., 2014; Ingraham et al., 2014). The S/N improved enough for the pipeline to find the satellite spots in subsequent steps in at least the central wavelength slice of each $K1$-band IFS cube. Sky-subtraction at the 2D detector was attempted but this step appeared to introduce more noise. The sky subtraction was therefore left to PSF subtraction at later steps using pyKLIP (Wang et al., 2015). For bad spaxel mitigation, a bad pixel identifier and smoothing was applied similar to Draper et al. (2016b). The satellite spots were then identified by centering on a high pass filtered image of the data. A best guess position for a slice with high S/N was identified by eye once for the whole sequence to aid the spot location algorithm. The unfiltered images then had their satellite spots extracted to measure the stellar spectrum convolved with the instruments response function in wavelength and time. The spectrum of each cube was calibrated by comparing the measured flux with the 2MASS magnitude for each respective band. A color correction was applied by comparing the measured spectrum to a real, atlas template spectrum (Pickles, 1998) for a star of HD 111520's spectral type (F5V). These two factors essentially measure the flux conversion factors for each cube so that the satellite spots have the same absolute flux and spectra as an F5V star. This calibrates the data in the cube to physically relevant units of Janskys. This algorithm

was tested on a known white dwarf spectrum in Maire et al. (2014b) and found to be within a 5% flux error with on sky observations. The reduced data cubes are then run through the program, pyKLIP, which utilizes ADI and subtracts the stellar PSF to remove additional flux from the star. For a more in-depth description of this process, we refer to Draper et al. (2016b).

The final images resolving the disk on both polarized and total intensity can be seen in Figure 4.1. Additionally, we also include the S/N of our polarized intensity data, which are generated by dividing the Q_ϕ images by noise maps derived from the U_ϕ images. To create these noise maps, as mentioned previously in Chapter 3 we use U_ϕ to calculate the standard deviation at each radius in 1-pixel wide stellocentric annuli. Here, we are assuming that U_ϕ contains no disk signal, which would be expected for an optically thin debris disk causing single scattering.

To better understand the prior HST results, we reprocessed the archival STIS data from GO-12998 (PI Padgett). HD 111520 was acquired behind the WEDGEA1.0 mask position and imaged in two consecutive orbits with two different roll angles separated by 32°. Each orbit accumulated five 419s integrations. PSF subtraction was accomplished by differencing the two calibrated and registered _sx2.fits images from each other. The two PSF-subtracted images were rotated to north and the data were averaged.

4.3 Observational Analysis

To better understand the disk morphology and asymmetry, we perform an empirical analysis on our multi-wavelength GPI data. This includes measuring the vertical structure through the disk FWHM and the vertical offset from the star (i.e., the location of the disk spine), as well as measuring the surface brightness in each band. Characterizing the disk morphology allows us to probe the cause of the observed asymmetries, as different disk perturbers affect the disk differently. For example, interaction with a planet companion may cause structures in the disk geometry such as warps and eccentricities, whereas an interaction with the ISM or a giant impact may cause an asymmetry in the dust grain properties creating an asymmetrical disk color. These results will be further discussed in the context of possible disk perturbers in Section 4.4.

Figure 4.1: **Top:** The total intensity (TI) detections of HD 111520, produced by pyKLIP. **Middle:** Polarized intensity (PI) of HD 111520. The polarized intensity is taken from the rotated stokes frame (Q_ϕ) to isolate the astrophysical emission. **Bottom:** S/N of the polarized intensity detections measured by dividing noise maps from the Q_ϕ data (see Section 4.2). The disk is consistently dimmer on the SE (left) extension of the disk compared to the NW (right) extension of the disk. The circles represent the size of the focal plane mask (0.09″, 0.12″, 0.15″ for J, H, and $K1$ respectively), and the crosses represent the location of the star. For all data, East is left and North is up.

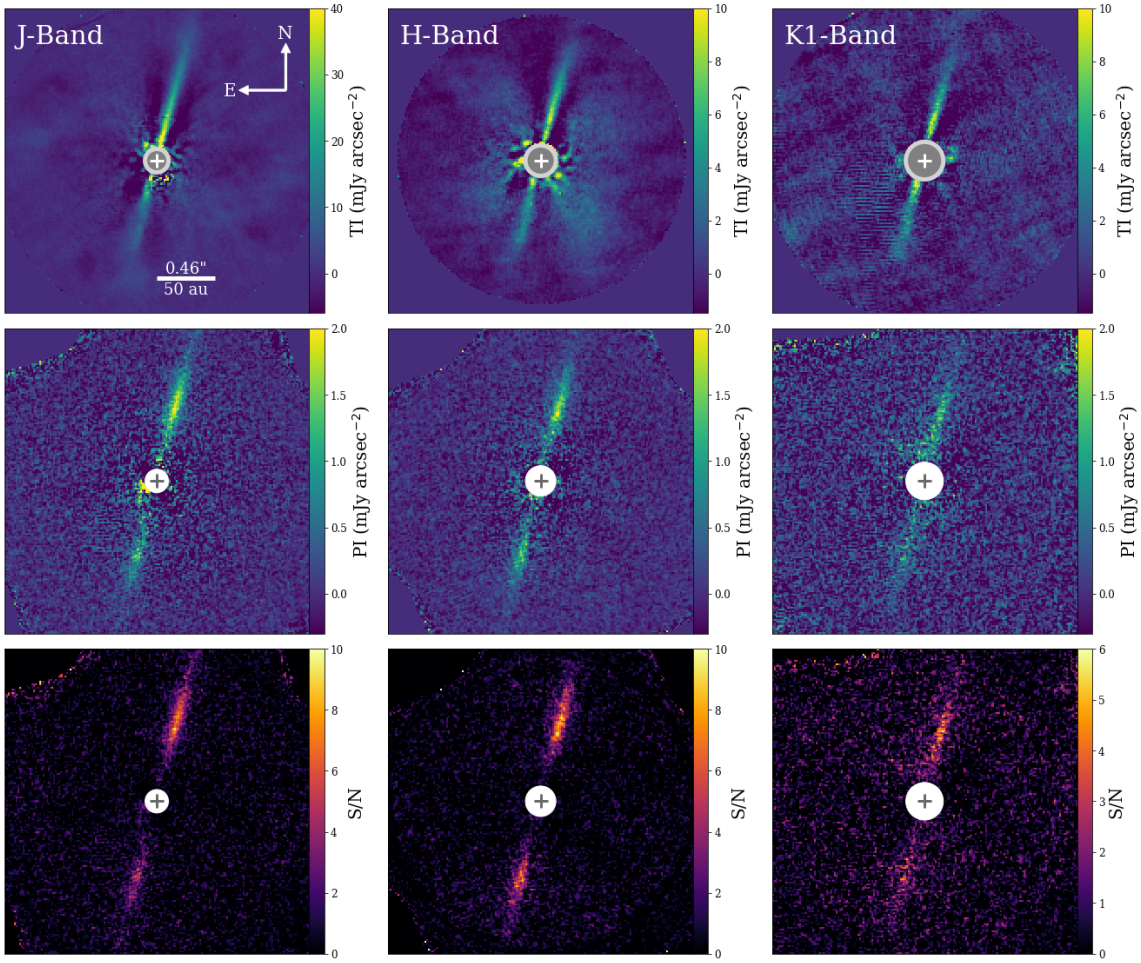

4.3.1 Vertical Structure

To measure the vertical structure, we fit a 1-D Gaussian profile to the vertical surface brightness profile at a series of radii from the star. As the disk structure should not vary significantly within our small wavelength range, we choose to focus this analysis mainly on the H band, as it has the best S/N, but also perform the analysis on the J and $K1$ band in order to compare. Additionally, we utilize the polarized intensity data, as we believe it most accurately represents the true disk structure, without the biases introduced by ADI-based PSF subtraction employed for the total intensity data.

We first prepared the data by rotating our data by 75° clockwise, similarly done in Draper et al. (2016b). The data are then binned into 2×2 pixel bins, and additional smoothing using a Gaussian with σ=2 pixels (0.028") is applied. This is done to increase the S/N and ensure a good fit to the data. Once the Gaussian profile is fit to vertical surface brightness slices along the entire disk using a non-linear least squares fit, the mean value and full-width-half-max (FWHM), along with 1σ uncertainties of each Gaussian fit are extracted. The mean value (i.e., the center of the Gaussian) represents the disk spine, or more specifically, the vertical offset from a horizontal line passing through the star, whereas the FWHM represents the approximate vertical width of the disk. The resulting FWHM and vertical offset profiles for all three bands can be seen in Figure 4.2. We are able to detect the emission in the H band out to $\sim 1''$ on either side of the disk. While the $K1$ band is also detected symmetrically (although only out to $0.8''$ given the lower S/N), the J band does show a radial asymmetry where the SE extension is detected out to $\sim 1''$, and the NW extension is detected to $\sim 1.1''$, which corresponds to a difference of 11 AU.

Taking the weighted mean of the H-band FWHM profile, we find the disk to have an approximate FWHM of $0.18''$. This is much greater than the GPI's instrumental H-band PSF FWHM of $0.05''$, showing that the disk is well resolved. However, this instrumental PSF and any smoothing/binning of the data must be taken into account in order to obtain an intrinsic measurement for the FWHM. This is done by subtracting in quadrature the FWHM of the instrumental PSF, as well as the FWHM of any smoothing applied, from the measured FWHM. Doing so, we obtain an intrinsic FWHM of $0.12 \pm 0.1''$ for the J and H band, and $0.14 \pm 0.1''$ for the $K1$ band (13-15 AU), which leads to a aspect ratio of $\sim$0.28 at 50 AU. This aspect ratio is intermediate between similar measurements at 50 AU for other near edge-on debris

Table 4.2: Measured properties of the vertical profile for each band. This includes the weighted intrinsic FWHM, along with the best fit inclined ring model parameters.

Band	FWHM ($''$)	R_d ($''$)	δ_x ($''$)	δ_y ($''$)	i ($^\circ$)	PA ($^\circ$)
J	0.12±0.01	$0.74^{+0.01}_{-0.01}$	$0.19^{+0.01}_{-0.01}$	$-0.009^{+0.001}_{-0.001}$	$89.43^{+0.03}_{-0.03}$	$165.06^{+0.01}_{-0.01}$
H	0.12±0.01	$0.83^{+0.01}_{-0.01}$	$-0.04^{+0.01}_{-0.01}$	$-0.002^{+0.001}_{-0.001}$	$88.71^{+0.08}_{-0.06}$	$165.67^{+0.03}_{-0.03}$
K1	0.14±0.01	$0.87^{+0.07}_{-0.04}$	$0.06^{+0.07}_{-0.04}$	$0.004^{+0.003}_{-0.003}$	$87.95^{+0.23}_{-0.23}$	$166.12^{+0.15}_{-0.18}$

disks such as HD 32297 (0.17, Duchêne et al. 2020) and HD 106906 (0.31, Crotts et al. 2021), although these comparisons are purely from empirical estimates and not from a proper disk model. A positive trend can be seen in the NW extension in all three bands, showing that the vertical width increases with radial distance on this side, while the SE extension is flat past $0.6''$. This differs slightly from Draper et al. (2016b), which only shows a positive trend in the NW extension past $0.7''$. Additionally, an enhancement in the vertical width can be seen in the SE at a separation of $\sim 0.5''$, strongest in the H and $K1$ bands, but also visible in the J band. A similar feature was observed in Draper et al. (2016b), although we find this enhancement to be $0.1''$ farther from the star. Given that the previous measurements were done with the total intensity H-band data, which are likely affected by PSF subtraction, our results using the polarized intensity are likely better to represent the true disk vertical width.

The vertical offset along the disk is small, with the largest offset being less than $0.03''$, due to the disk being highly inclined. However, a clear offset can be seen in each band in Figure 4.2, showing that the disk inclination is not exactly 90°. In all three bands, the majority of data points are negative, indicating that the front side of the disk lies to the west, contrary to what is observed in Draper et al. (2016b). We are also able to clearly detect a vertical offset in the SE extension, whereas the previous measurements in Draper et al. (2016b) were unable to do so, showing the improvement that our polarized data have in measuring the vertical profile of the disk.

To further constrain the disk geometry, we fit the vertical offset or disk spine with a narrow, inclined ring model, similarly used in Duchêne et al. (2020). We perform the fitting for all three bands, which will allow us to determine which parameters can be well constrained and which ones cannot. For the fitting procedure, MCMC via the python package *emcee* (Foreman-Mackey et al., 2013) is utilized. Ring models are first generated from the equation of an ellipse with a given disk radii (R_d), x and y disk offset (δ_x, offset along the major axis, and δ_y, offset along the minor axis.),

Figure 4.2: **Left:** The vertical width (FWHM) profile of HD 111520 as a function of separation from the star in each band. The grey horizontal dashed line represents the measured weighted FWHM, while the red line represents the intrinsic FWHM as measured in the H band. The dark blue line represents the FWHM of the GPI H-band PSF. **Right:** The vertical offset profile as a function of the separation from the star in each band. The dashed grey line represents the best fitting narrow ring model for the H band. For both profiles, we exclude measurements within $0.3''$ and greater than $1''$ (with exception of the J band) due to low signal-to-noise.

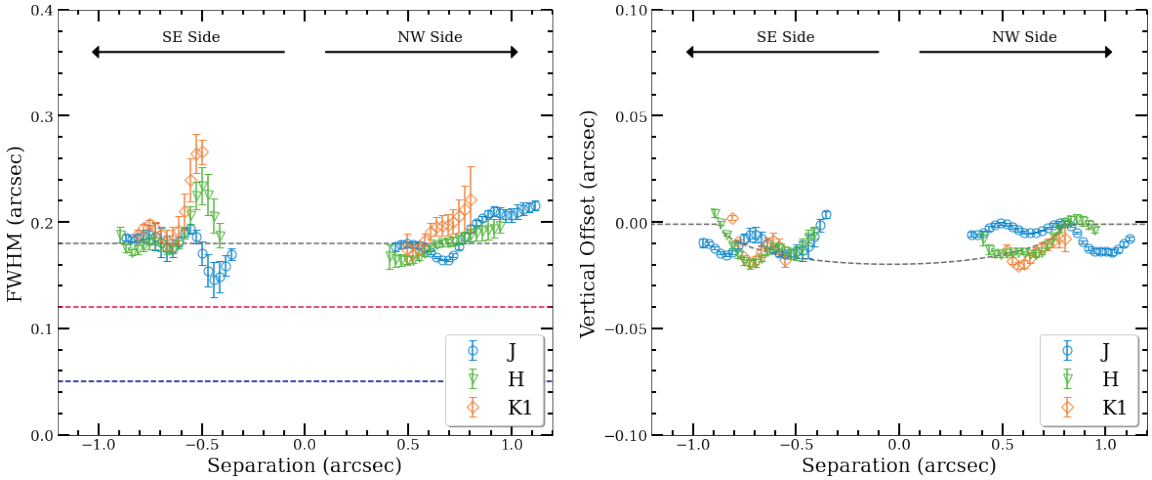

disk inclination (i), and position angle (PA) measured from East of North through rotating the data. Note that for the disk offsets, a negative value means a disk offset towards the left or down, while a positive value means a disk offset towards the right or up. These models are then compared to the data points using a χ^2 function. The results from this fitting procedure for all three bands can be found in Table 4.2.

Through this modelling, there are three parameters that we can better constrain: the inclination, PA and δ_y. As expected, we find HD 111520's debris disk to have a very high inclination, no more than 2.7° away from completely edge-on given 3σ uncertainties of the PA in the $K1$ band. Our measurement of the PA is also consistent with that measured in Draper et al. (2016b), where we find it to lie between 165° and 166°. We find no significant offset along the minor-axis (δ_y), with an offset of $\lesssim 0.01''$. Taking into consideration the uncertainty in the position of star, which is 0.05 pixels (or ∼0.7 mas) for GPI (Wang et al., 2014b), makes this small offset negligible. Unfortunately, due to the high inclination of the disk, the disk radii, R_d, and offset along the major-axis, δ_x, are too difficult to constrain from this type of modelling, and varies significantly between bands.

A possible warp is identified in Draper et al. (2016b), where the SE extension was

found to not align perfectly with the NW extension. However, such a warp is not seen in our vertical offset profiles. As a confirmation, we also check the vertical offset profiles for all three bands of the Spec data. Doing so, we find that this potential warp is also not present, showing that the warp feature is likely an artifact and a result of PSF subtraction in the H-band Spec data. This again shows that our higher S/N data greatly improves our measurements of the vertical profile and helps better constrain the disk's morphology and orientation.

4.3.2 Surface Brightness

Previous analysis of GPI observations for HD 111520 report a 2:1 brightness asymmetry in the H band (Draper et al., 2016b). We measured the surface brightness of our multi-wavelength data to better constrain the brightness asymmetry across all three bands, as well as to measure the disk color. Here, the vertical offset profile is used to approximate the peak surface brightness location along the disk. The surface brightness is integrated along 2 by 12 pixel bins at a series of radii from the star, where 12 pixels is similar to the measured FWHM of the disk. For the polarized intensity, 1σ uncertainties are measured using noise maps derived from the U_ϕ data in each band. In contrast, 1σ uncertainties for the total intensity are measured using the standard deviation of similar sized bins located at the same radial distance but outside the disk. We do not take into account the additional uncertainty in our total intensity data due to self subtraction, as we are mainly interested in the brightness asymmetry between the two extensions, but note that this uncertainty exists. Figure 4.3 shows the final surface brightness as a function of separation from the star for all three bands in both polarized and total intensity. Only data points with a S/N$\geqslant$3, are plotted.

By eye, a stark difference between the polarized and total intensity surface brightness profiles can be seen. While the total intensity appears to peak either within or near the focal plane mask, and then consistently decreases with distance, the polarized intensity instead peaks at a farther separation on either side. This difference can be easily explained by the scattering phase function of the disk, where the total phase function should peak at small scattering angles due to strong forward scattering (Milli et al., 2017), while the polarized phase function should peak at larger scattering angles (Engler et al., 2017; Milli et al., 2019). Interestingly, the peak polarized intensity differs between the NW and SE extensions consistently between the three

Figure 4.3: **Left:** The disk emission in polarized intensity as a function of separation from the star. The two vertical grey dashed lines represent the estimated location of the peak polarization on either side of the disk. **Right:** The disk emission in total intensity as a function of separation from the star. Disk orientation is the same as in Figure 4.2.

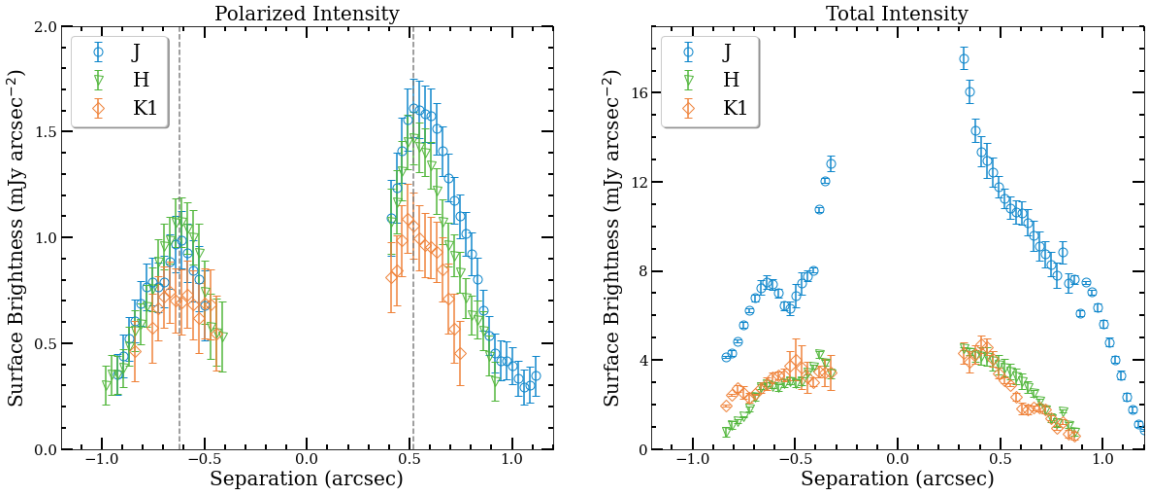

bands, where the NW extension peaks closer at $\sim 0.52''$ from the star compared to the SE extension which peaks at a separation of $\sim 0.62''$ from the star (corresponding to a difference of ∼11 AU). This suggests an eccentric disk with the NW extension located closer to the star compared to the SE extension.

Additionally, a clear brightness asymmetry can be seen in both polarized and total intensity. To probe the significance of this asymmetry, we compare the flux between the NW and SE extensions in all three bands. This is done by integrating the disk flux through two rectangular apertures (sized 30 by 15 pixels) placed on the NW and SE extensions at $0.35''$ to $0.8''$ from the star, and then comparing the total integrated flux between the two sides. Uncertainties for the polarized intensity are measured by integrating the flux of the noise maps over the same aperture, while for the total intensity the uncertainty is measured by taking the standard deviation of the same sized aperture located at the same radius but placed outside the disk. The NW/SE integrated flux ratio for each band, Pol and Spec, can be found in Table 4.3. Our results show a similar trend between the polarized and total intensity with a large brightness asymmetry, most prominent in the J band, of ∼1.8:1, although not as large as the 2:1 asymmetry reported in Draper et al. (2016b). What is more surprising is the apparent wavelength dependency of the brightness asymmetry, where the asymmetry seen in the H and $K1$ bands is significantly lower at only ∼1.5:1. We

Table 4.3: Measured brightness asymmetry between the NW and SE extensions (NW/SE) with 1σ uncertainties.

Mode	J	H	K1
Pol	1.77 ± 0.07	1.48 ± 0.05	1.45 ± 0.08
Spec	1.83 ± 0.01	1.44 ± 0.01	0.98 ± 0.01

Table 4.4: Measured disk color using polarized and total intensity, with 1σ uncertainties.

Bands	NW Extension (mag)	SE extension (mag)
J-H (pol)	-0.34 ± 0.03	-0.13 ± 0.05
J-K1 (pol)	-0.77 ± 0.04	-0.49 ± 0.06
H-K1 (pol)	-0.44 ± 0.04	-0.36 ± 0.06
J-H (spec)	-1.59 ± 0.01	-1.17 ± 0.01
J-K1 (spec)	-1.77 ± 0.01	-1.16 ± 0.01
H-K1 (spec)	-0.18 ± 0.01	-0.01 ± 0.01

also find no brightness asymmetry at all in the $K1$-band total intensity, although this may be partially due to self-subtraction. Thus, the observed brightness asymmetry is strongest at shorter wavelengths and decreases as wavelength increases.

Through the surface brightness in each band, we can also extract the disk's color which can provide some information about its dust grain properties. This is because disk color is highly dependent on the scattering properties of dust grains which are affected by composition, porosity, and grain size. For example, a blue disk color at NIR wavelengths can be caused by sub-micron sized grains or very porous grains (Boccaletti et al., 2003). While it is difficult to disentangle these dust grain properties from the disk color alone, we would expect that the disk color should be the same across the disk given symmetrical dust grain properties. To measure the disk color, we use the same integrated flux used for measuring the brightness asymmetry. We then compare the integrated flux on both sides between each band, which are converted to magnitudes. Finally, given that these are scattered light observations, the stellar magnitude must be taken into account in order to measure the disk color. In this last step, the difference in magnitude of the star between each band is subtracted from the difference in disk magnitude between each band (ex. $J-H = (J-H)_{disk} - (J-H)_{star}$). For the stellar magnitudes, we use the 2MASS J, H, and K magnitudes (8.00 ± 0.02 mag, 7.83 ± 0.06 mag, and 7.72 ± 0.02 mag respectively; Cutri et al. 2003).

The derived disk colors can be found in Table 4.4. We include measurements

for both polarized and total intensity for comparison, but note again that the total intensity data likely suffer from severe self subtraction, and therefore provide less reliable measurements compared to the polarized intensity. These values show that the disk has a blue color at NIR wavelengths. However, what is even more interesting, is that the NW extension appears to be bluer than the SE extension in $J - H$ and $J - K1$, while the difference in color is still present but decreases significantly with $H-K1$ in both total and polarized intensity. This, along with the stronger asymmetry in the J band, suggests we are probing different dust grain properties at shorter wavelengths, a possibility which will be discussed further in Section 4.4.

4.3.3 HST Observations

While this paper is mainly focused on the micron sized dust grains of the debris disk around HD 111520 as observed with GPI, we also take a deeper look into observations with HST STIS. HST data are sensitive to the smallest dust grains set on highly eccentric parabolic orbits by radiation pressure that form the most extended component of debris disks, also known as the disk halo (Hughes et al., 2018). These observations can be seen plotted in Figure 4.4, with the GPI data in Spec H band plotted in the center. Like the dust grains observed with GPI, the disk halo also features strong asymmetries. This includes an even larger brightness asymmetry of 5:1, a radial asymmetry between the two sides, as well as a bifurcation or 'fork' feature observed in the NW extension (Padgett & Stapelfeldt, 2015; Draper et al., 2016b). To probe the disk halo structure further, we measure the vertical offset of the HST STIS image in a similar manner as in Section 4.3.1, however, for the fork structure, we instead fit a double Gaussian profile instead of a single Gaussian profile. These results can be seen in Figure 4.5 along side the GPI vertical offset profile in the polarized H band for comparison.

What we find is that the disk halo appears to be warped, where beyond radial separations of $\sim 1.7''$, the vertical offset of the disk halo turns from being relatively flat and aligned with the GPI-imaged inner disk, to becoming sloped. While the SE extension warps downwards, the NW extension slopes upwards by roughly the same angle ($\sim 3.8°$). We are also able to resolve the vertical offset of the fork down to $\sim 2.5''$ and out to $6''$. The warp in the NW appears to align with the upper fork, while on the other hand, the GPI data appears to be aligned with the bottom fork. While there is a small uncertainty in the disk PA for both the GPI and HST STIS

Figure 4.4: HD 111520 as seen by HST STIS (0.59 μm) and GPI (1.65 μm), both rotated by 75.7° clockwise. The HST image is viewed in log scale. The southern extension is significantly dimmer than the northern extension, with brightness asymmetries of 1.5:1-1.8:1 within GPI's FOV and 5:1 in HST's FOV (Padgett & Stapelfeldt, 2015). From GPI to HST scales, it is clear that there is a large-scale change in the disk. The South to North extension of the disk appears to have an asymmetrical geometry, with a possible bifurcation, or 'fork', seen on the Northern side (Padgett & Stapelfeldt, 2015). The central arrow represents the direction of the proper motion for the system.

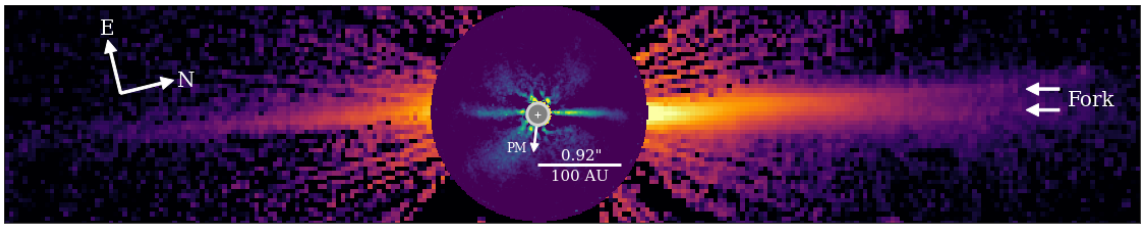

instruments of $\sim 0.1°$ each, this uncertainty does not change the alignment between the GPI data and the lower fork seen in the disk halo.

These results help clarify the disk morphology and show that the disk is being perturbed at large radial distances from the star. A planet companion as the potential cause for the warped structure and asymmetries of the disk halo will be addressed in Section 4.4.

4.4 Discussion

Through the analysis of HD 111520's disk structure, surface brightness and disk color at multiple wavelengths, we have measured the disk's geometry, brightness asymmetry and placed constraints on the dust grain properties. We find that the brightness and radial asymmetry is strongest in the J band and that the disk color of the NW extension is relatively bluer than the SE extension in $J-H$ and $J-K1$, while becoming more comparably blue in $H-K1$. This shows a possible wavelength dependence on all of the disk's observed asymmetries. As the disk color heavily depends on the dust grain properties, a difference between the color of the two extensions suggests we are probing different dust grain properties, either with the minimum dust grain size, composition, porosity, or a combination of these. The brightness asymmetry may also be explained by the disk eccentricity or an asymmetry in the dust mass distribution. In this section, we explore different scenarios by which the asymmetries and features seen in HD 111520 could have been formed given our results from the analysis of the

Figure 4.5: Vertical offset profiles of the GPI and HST data for HD 111520. Both images are rotated by 75.7° clockwise. The dark blue data points represents the GPI vertical offset in pol H band, the light blue data points represents the HST vertical offset, while the orange data points represent the vertical offset of the bifurcation or 'fork' feature observed with HST in the NW extension. The diagonal grey dashed lines are plotted to show the slopes of the SE and NW extensions of the disk halo seen with HST, while the horizontal grey dashed line shows the alignment of the GPI data. The vertical shaded regions at 1.7″ show where the the disk halo changes from being relatively flat to sloped.

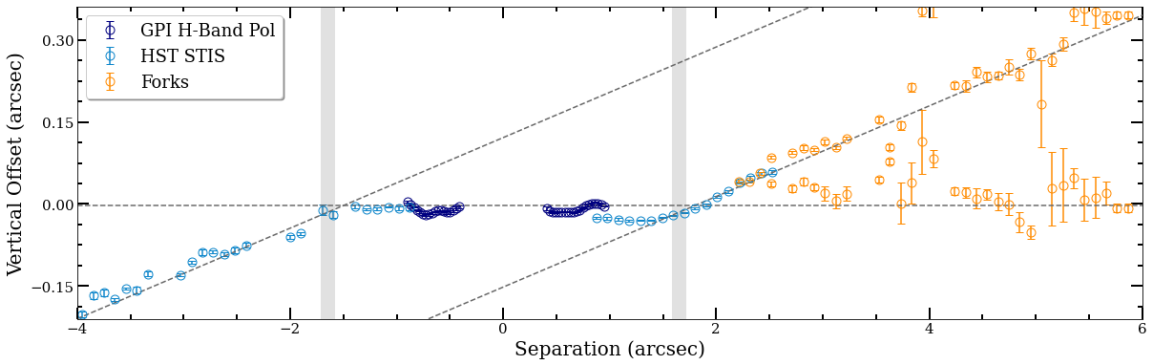

GPI data, as well as the morphology of the disk halo observed with HST.

4.4.1 Disk Eccentricity

While it is difficult to derive information about a possible disk offset along the major axis through the vertical structure, given the high inclination, there is another clue that points towards the disk being eccentric. This includes the polarized intensity surface brightness profile, where we measure the brightness in the NW extension to peak closer to the star compared to the SE extension. In the case where there is no disk eccentricity, we would expect that the surface brightness would peak in the same location on either side. If the disk instead has some eccentricity, this would cause one side of the disk to be closer to the star, bringing the peak surface brightness of that side inwards and creating a pericenter glow (Wyatt et al., 1999; Pan et al., 2016). For HD 111520, this would mean that the NW extension lies closer to the star than the SE extension. If this is the case, this could at least partially explain the brightness asymmetry seen, as the NW extension would be receiving a higher amount of stellar light.

Given the separations of the two polarized peaks ($\sim 0.52''/0.62''$), we can place constraints on the possible eccentricity of the disk. Assuming that the argument of

periapsis and the peak polarized intensity are both along the projected major axis, this leads to estimated eccentricity of 0.09. If the argument of periapsis is not along the projected major axis, the true eccentricity would be even larger making 0.09 a lower limit, however, this lower limit may be slightly overestimated if the peak polarized intensity is not along the projected major axis. Even so, such an estimated eccentricity is significant, and only observed in a handful of debris disks. One exciting aspect of these measurements is that an eccentric disk may point towards a hidden planetary companion, as planets on eccentric orbits have been shown to induce eccentric disks through dynamical simulations (Lee & Chiang, 2016; Lin & Chiang, 2019), as well as observations (e.g. Fomalhaut; Kalas et al. 2005, MacGregor et al. 2017). However, further analysis is required to see if an eccentric disk can fully explain the brightness and structural asymmetries observed.

As the surface brightness is related to $1/r^2$, with r being the radial separation from the star, we can also estimate what the brightness asymmetry should be given the different locations in the projected peak surface brightness. Taking the ratio of $1/r^2$ between the two sides, we find that a brightness asymmetry of $\sim$1.3:1 would be expected at a distance of between $0.5''$ and $0.6''$ from the star, assuming that the projected peak polarized intensity is occurring at the disk ansae. If in fact the projected peak polarized intensity is occurring elsewhere along the projected major axis, the expected brightness asymmetry would be even less. This is considerably lower than the 1.5:1 to 1.8:1 brightness asymmetry observed in the polarized intensity at these distances, meaning that while an eccentric disk may partially explain the observed brightness asymmetry, there must be another mechanism at play. This is further supported by the fact that, in the J band, the NW extension is much more extended than the SE extension, which should not be the case for an eccentric disk with a stellar offset towards the NW. Additionally, an eccentric disk alone would not explain the differences in brightness asymmetries we observe between bands, as well as the relatively bluer disk color observed in the NW extension. These inconsistencies again show that we need another phenomenon to help explain the disk's asymmetries.

4.4.2 ISM interaction

Another possible explanation for the observed asymmetries is an interaction with the ISM. By passing through a dense ISM cloud, this can cause small dust grains in particular to be pushed towards the side of the disk opposite the direction of motion

(Debes et al., 2009). This redistribution of small grains from one side of the disk to the other can cause one disk extension to become relatively brighter and more extended at shorter wavelengths, both of which we observe for HD 111520 with GPI. Similar features can be seen with HST, where the NW extension is brighter and more extended than the SE extension, as shown in Figure 4.4. If the NW extension is populated with smaller grains compared to the SE extension, this would also explain the much bluer disk color in the NW extension observed in J-H and J-$K1$. However, for this to occur, the proper motion of the star must align in the correct direction. In the case of HD 111520, to create a NW extension that is brighter and bluer than the SE extension through an ISM interaction, the proper motion of the system must also be pointing towards the SE direction. The current measurements for HD 111520's proper motion are -35.3 mas/yr in RA and -16.7 mas/yr in Dec (Gaia Collaboration et al., 2021). Based on these measurements, this would mean that the proper motion is pointing towards the SW direction rather than the SE (see Figure 4.4), essentially ruling out an ISM interaction as the cause of the disk's color, radial and brightness asymmetries.

4.4.3 Giant Impact

Another possible explanation of the features of HD 111520's debris disk would be a giant impact of two large bodies within the disk. Such an impact would generate an avalanche of small dust grains that would start out in a clump at the collision site, and would be redistributed throughout the disk over time. This scenario is consistent with the large brightness asymmetry observed and the difference in disk color, assuming that the impact occurred in the NW extension. A giant impact would have had to occur recently, on the order of a few thousand orbits (1 Myr at 50 AU), in order for the pinched collision point to still be present, causing the observed asymmetries (Jackson et al., 2014). Because all particles are forced to pass through the collision point, this allows for further collisions and generation of small dust grains. After the collision point is smeared out, the asymmetry in the generated dust grains would start to become washed out due to collisional diffusion and blown out due to radiation pressure, returning the disk to an axisymmetric state over time. There are a few issues with this scenario, however. One issue is that typically the side opposite of the impact would be more radially extended (Jackson et al., 2014), whereas for HD 111520 we observe the opposite, although it is important to note that radiation pressure would

also be playing a role in blowing out the small grains and we may not be sensitive to dust grains on the radially extended side, given the expected lower surface brightness. Another issue is that verification of this hypothesis is unfortunately not possible with GPI data alone.

Further evidence would include analyzing the dust mass distribution, which can be obtained through mm observations, as the majority of the observable disk mass lies within mm-sized dust grains and these grains are less susceptible to radiative forces in the disk. If the dust mass distribution in the mm-sized dust grains is also asymmetric, this would support a giant impact scenario and would help explain the very large surface brightness asymmetry. Higher resolution CO observations would also be extremely useful in this case, as a large impact may release a large amount of CO gas. If a concentration of CO is observed in the NW extension, this would help confirm the possibility of a giant impact as it has for the β Pic debris disk (Dent et al., 2014). While a marginally-resolved continuum observation of the HD 111520 disk has been made with ALMA at 1240μm (Lieman-Sifry et al., 2016), establishing an asymmetric dust mass distribution requires the disk to be well resolved. Along with the continuum, low resolution CO observations were also taken but no CO was detected. It is worth noting that there are several disks that are asymmetric in scattered light with symmetric mm-sized grains (HR 4796, HD 61005; Olofsson et al. 2019; Buenzli et al. 2010; MacGregor et al. 2018), however, such observations would still provide important information about the overall disk morphology. If there is an asymmetry in the mm-sized grains, then a local enhancement due to a large impact is likely, while symmetric mm-sized grains would support the need for an alternative mechanism to explain the asymmetries present in the scattered light in addition to an eccentric disk. Thus, high resolution ALMA observations of the mm continuum emission will be necessary in order to support or refute the hypothesis of a recent giant impact.

4.4.4 Disk Halo

In Section 4.3.3, our analysis of the HST observations revealed that the disk halo is warped past $\sim 1.7''$ on either side of the disk by 3.8°. Additionally, the fork structure in the NW extension is resolvable from 2.5″-6″. While the upper part of the fork is aligns with the warp of 3.8° in the NW extension, the lower fork is aligned with the inner part of the disk as observed with GPI. This alignment can rule out certain

scenarios for the cause of the fork structure, such as self shadowing from a higher dust mass in the NW extension as suggested in (Draper et al., 2016b), which would require the larger grains to be aligned between the two forks.

One possible explanation for the fork's existence is that somewhere in the system exists an undetected planetary companion with a mutual inclination relative to the disk's. Such a planet has been shown to cause an "X" shape in the disk morphology in the dust density distribution, which may be observed as a fork like structure on either one or both sides of the disk depending on the viewing angle (Pearce & Wyatt, 2014). However, this mainly applies to larger grains while smaller grains are also affected by radiation pressure, which may lead to a diminished effect. Such a planet may also cause the disk to become warped, such as the case with the inner disk of β Pic (Mouillet et al., 1997; Dawson et al., 2011; Apai et al., 2015). In the case of HD 111520, the warp observed would suggest a planet inclined at $\sim 3.8°$ relative to the disk, orbiting at a distance greater than $1.7''$ ($\sim$184 AU) where the warp is observed. While dynamical modelling would be needed to place better constraints on a planet perturber, the complex structure of the disk halo does show that a planet companion at large separations likely exists in this system.

4.5 Conclusion

Using deep, multi-wavelength GPI data of HD 111520's debris disk in both polarized and total intensity, we have been able to measure the disk's vertical structure, surface brightness profiles, and disk color.

- We find that the disk has an intrinsic FWHM $0.12''$-$0.15''$ between the J, H and $K1$ bands. The profile also exhibits a positive trend between the FWHM and radial distance in the NW extension, while in the SE extension a FWHM enhancement is observed at $\sim 0.5''$ which then flattens out past $0.6''$.

- Measuring the vertical offset along the disk, we find that the west side is the front side of the disk. The measured disk spine also lies within $0.03''$ of the star location, showing the disk to have an inclination close to (but not quite) 90°. This is confirmed through modeling the vertical offset profile, where we derive an inclination roughly between 87°-89° and a PA of 165°-166° from the best fitting models. We also derive disk offsets of δ_x and δ_y, however, the disk

is too highly inclined to place a good constraint on the disk offset along the major-axis. No disk offset is found along the minor-axis.

- Through characterization of the disk structure, we find a radial asymmetry exists, with a NW side that is more extended than the SE. However, this radial asymmetry is only present in the J band, while not present in the H and $K1$ bands.

- By measuring the surface brightness in all three bands, we find that the polarized intensity and total intensity have two very different profiles. Additionally, the polarized intensity peaks closer to the star in the NW extension compared to the SE extension, suggesting that the disk has an eccentricity of $\gtrsim$0.09. Although given an offset of $\sim$11 AU along the projected major axis, this eccentricity would not be sufficient enough to be the sole cause of the disk's brightness asymmetry.

- Comparing the surface brightness on either side shows a 1.5:1-1.8:1 brightness asymmetry, slightly less than what is observed in Draper et al. (2016b). This asymmetry appears strongest in the J band and decreases with wavelength.

- Similarly, measuring the disk color between each band in polarized intensity shows that the NW extension is relatively bluer than the SE extension in $J-H$ and $J-K1$, while this trend is not as strong in the $H-K1$ color.

- Through measuring the vertical offset of the disk halo as seen with HST, we find that the small grains at large separations ($> 1.7''$) are highly warped on either side. We also are able to measure the fork down to $\sim 2.5''$, where the GPI data appears to align with the lower fork.

Given the possibility of an eccentric disk, as well as the warped morphology of the disk halo, this suggests that there may be at least one planet perturber in this system, although dynamical modelling is needed to test this scenario. On the other hand, one way in which we can explain the large brightness asymmetry, as well as the difference in disk color between the two extensions, is if the two extensions contain differing dust grain properties, such as smaller grains in the NW extension. This can be caused by two scenarios: 1. An interaction with the ISM, or 2. a giant impact. While an ISM interaction would provide a straight-forward explanation, the proper motion is not in the correct direction to account for the asymmetries between the NW and SE extensions. On the other hand, a recent giant impact between two large

bodies may also be the source for the surface brightness and disk color asymmetries; however, further observations/evidence are needed to probe this scenario further. Specifically, a sub-arcsecond resolution image of the dust mass distribution and CO through higher resolution ALMA observations is essential.

HD 111520 serves as a very interesting and unique system to study, with such a large brightness asymmetry compared with other debris disks, as well as a complicated overall disk morphology. By studying the disk in greater detail, we can gain a greater understanding of the ways in which dynamical perturbations and collisions can affect disk morphologies, as well as how these types of debris disk systems evolve.

Chapter 5

N-Body Simulations of the HD 111520 Disk: Hunting for the Warp Driving Planet

As described in Chapter 1, debris disks are formed through the collisions of rocky bodies such as asteroids and comets. To sustain debris disks over millions of years, such collisions must be consistently occurring in order to supplement the planetesimal belt with sub-micron to milli-meter sized dust grains. This requires that the planetesimals in the disk are stirred so that their orbits are perturbed. Debris disks can be stirred by several mechanisms such as planets, stellar flybys and self-stirring by the planetesimals themselves. Previous studies have shown that most debris disks would have to be unrealistically massive to sufficiently stir the disk (e.g. Mustill & Wyatt 2009; Pearce et al. 2022; Krivov & Wyatt 2021), and stellar flybys are not very common. Planets on the other hand are extremely common and have the ability to sufficiently stir the disk (Wyatt, 2008). Therefore, it is possible that the mere existence of a debris disk indicates an underlying exoplanet system.

Many of the debris disks that have been spatially resolved in scattered light and emission have shown a variety of morphologies and asymmetric structure such as warps, spirals, eccentric disks, clumps, brightness asymmetries, etc. Such features can also be explained by planets. Despite this, only a few spatially resolved disks also have known planets, such as AU Mic, β Pic and HD 106906 (Plavchan et al., 2020; Martioli et al., 2021; Lagrange et al., 2010, 2019; Bailey et al., 2014). In many cases, the known planets have been directly linked to the morphologies of their disk, such as the warp in the β Pic disk caused by β Pic b (Chauvin et al., 2012), and the eccentric disk of HD 106906 caused by HD 106906 b (Nesvold et al., 2017). This

strengthens the argument that planets are often the cause of debris disk structures and asymmetries. We can therefore use their morphologies to estimate the probable masses and orbits of unseen planets in these systems.

In the previous Chapter, we confirmed using HST/STIS and GPI observations that the debris disk around HD 111520 is highly asymmetric and has a complex morphology. As a reminder, the STIS data traces the disk halo, consisting of sub-micron sized dust grains on eccentric orbits, while the GPI data traces the micron-sized dust grains located in the main planetesimal belt (located ∼50-110 au from the star). The disk presents one of the largest brightness asymmetries of any debris disk, where the northwest (NW) side is 2 times brighter than the southeast (SE) side seen with GPI, and 5 times brighter seen with STIS (Draper et al., 2016b; Crotts et al., 2022). The disk also harbours a radial extent asymmetry where both STIS and GPI observations show the NW side of the disk to be more radially extended than the SE side. Tracing the disk spine of the halo additionally reveals a ∼4° warp from the midplane on either side of the disk, alongside a bifurcation or "fork"-like structure in the NW where the disk midplane appears to split into two (Crotts et al., 2022). While the upper fork aligns with the 4° warp, the bottom fork aligns with the micron sized grains observed with GPI.

These structures and asymmetries strongly suggest the presence of an unseen planet. For example, the warp and fork is reminiscent of the warp and second disk component seen in β Pic, which again can be directly connected to the planet, β Pic b, which is inclined relative to the disk (Chauvin et al., 2012). The radial extent and surface brightness asymmetry can also be explained by an eccentric disk induced by a planet on an eccentric orbit, such as in the case of the HD 106906 disk (Nesvold et al., 2017). Additionally, other explanations have not been able to replicate the overall HD 111520 disk morphology. A recent massive collision between two rocky bodies is another way to create a fork, warp, eccentric disk and brightness asymmetry as found in Jones et al. (2023). However, in order to create the warp and radial extent asymmetry in the right direction, the collision would need to take place on the SE side of the disk, creating a brightness asymmetry opposite of what is observed, such that the SE side is brighter rather than the NW. This begs the question whether or not planets may be a better explanation for the overall disk morphology.

We attempt to answer this question here by using the n-body simulation code REBOUND (Rein & Liu, 2012). N-body simulation codes provide a useful tool for modelling asymmetric disks, as well as providing constraints on the responsible planet.

Figure 5.1: Initial orbital configurations and positions of the planets and disk for a planet with $a = 250$ au (**left**) and $a = 40$ au (**right**). The initial setup is shown both edge on (**top**) and face on (**bottom**). In both cases, the planet's argument of pericenter is viewed at 270°.

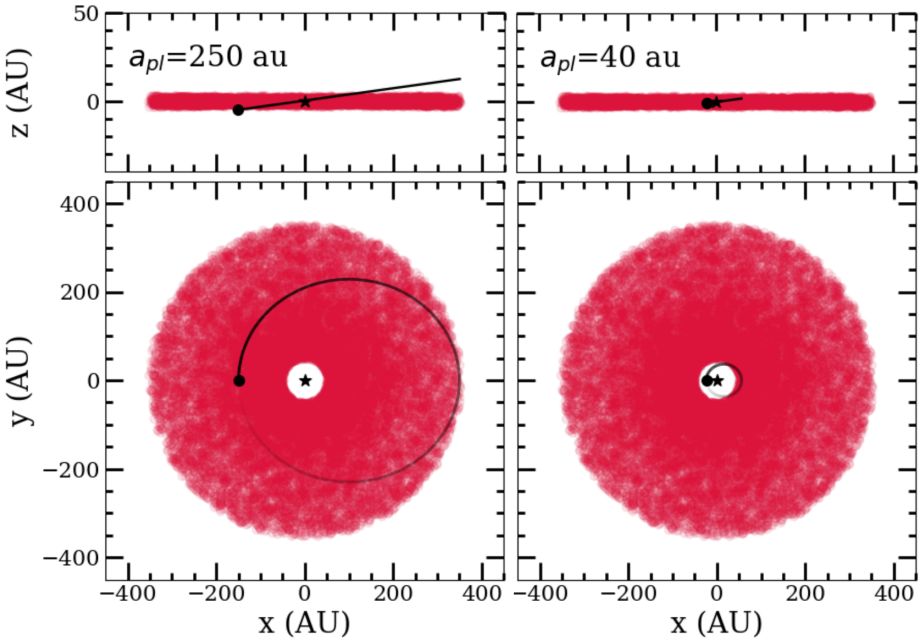

For example, in the case of the HD 106906 disk, using REBOUND, Nesvold et al. (2017) was able to provide constraints on the orbit of HD 106906 b, where they found that the planet would need to be on an eccentric and inclined orbit with $i < 10°$. Later constraints placed on the planet's orbit based on observations were found to be consistent with the results from these n-body simulations (Nguyen et al., 2021). In this paper, we use REBOUND to simulate the complex morphology of the HD 111520 disk via planet-disk interactions. Our goal is to provide information on whether or not a planet(s) may be responsible for the disk structures, and if so, also provide constraints on the mass and orbit of the planet. These constraints will be useful for determining the feasibility of detection with current and future instruments such as NIRCam on the James Webb Space Telescope (JWST) and GPI 2.0. Our model and simulation are described in Section 5.1 and our results are discussed in Section 5.2. We then further explore potential planet properties in Section 5.3 and discuss the implications of our results in Section 5.4. This work is submitted to the Astrophysical Journal.

5.1 Model

We use the n-body simulation code, REBOUND, to create models of the disk with the goal of constraining the planet mass and orbit responsible for the observed morphology. We start by looking at two scenarios: 1) A 1 M_{jup} planet orbiting outside the warp location (a = 250), and 2) A 1 M_{jup} planet orbiting within the disk inner edge (a = 40 au). We choose these two scenarios as a planet outside (e.g. HD 106906) and within the disk inner edge (e.g. β Pic) can both perturb the disk through secular perturbations. 250 and 40 au are chosen specifically, as 250 au is near the warp location (∼180 au, Crotts et al. 2022) and 40 au is near the estimated disk inner edge (∼50 au, Draper et al. 2016b). We also start with a 1 M_{jup} planet as this is below the current upper mass constraint of 3 M_{jup} set by GPI (Nielsen et al., 2019), but may be within reach of detection by select instruments such as JWST/NIRCam and GPI 2.0. In both scenarios the planet is on an eccentric (e = 0.4) and inclined (i = 2°) orbit relative to the disk as a starting point. The reasoning for these choices is to attempt to replicate the disk's radial extent asymmetry and the 4° warp from the midplane that is observed, as secular perturbations from an eccentric and inclined planet can force planetesimals onto similarly eccentric and inclined orbits (e.g. Mouillet et al. 1997; Heap et al. 2000; Wyatt 2008). This results in a disk that as is offset from the star (creating a radial extent asymmetry), and can create a warp near the planet location. Additionally, studies have shown that the resulting inclination of the disk $\approx 2i_{pl}$ (Dawson et al., 2011), hence why we choose $i_{pl} = 2°$.

5.1.1 Simulation Setup

We start both simulations by adding a 1 solar-mass star, a Jupiter-mass planet, and disk particles. While the stellar mass for HD 111520 is 1.26 $M_{\odot}$, we use 1 solar-mass to keep units simplified as REBOUND uses units where the gravitational constant, G, equals 1. The planet starts at their pericenter, which we set to be on the left side of the star, i.e the argument of pericenter, ω_{pl}, is defined to be 270°. We define ω in the same ways as REBOUND, where ω=0 is in the direction of the observer.

We add 20,000 massless disk particles between 50 and 350 au from the star with random longitude of ascending node (Ω_p), longitude of pericenter, and true anomaly (f_p) between 0 and 2π. We consider these particles "parent" particles. We start with a dynamically cold disk where disk particles have a small inclination dispersion of ±0.01 radians (0.58°), as well as a small eccentricity dispersion of ±0.01. Each

Figure 5.2: **Top:** Composite image of the HD 111520 disk optical HST/STIS data on large scales and the GPI H-band data within the HST coronagraph mask. This figure is modified from Crotts et al. (2022). **Middle:** Synthetic scattered light image of the HD 111520 disk with 1 planet orbiting outside the warp ($a = 250$ au) **Bottom:** Synthetic scattered light image of the HD 111520 disk with 1 planet orbiting inside the disk inner edge ($a = 40$ au). For both models, the surface brightness is in the same log scale, and surface brightness units are arbitrary. Additionally, the disk is inclined by 89°. The white dashed lines trace the "fork"-like structure and warp induced by the planet, and is the same in all three figures.

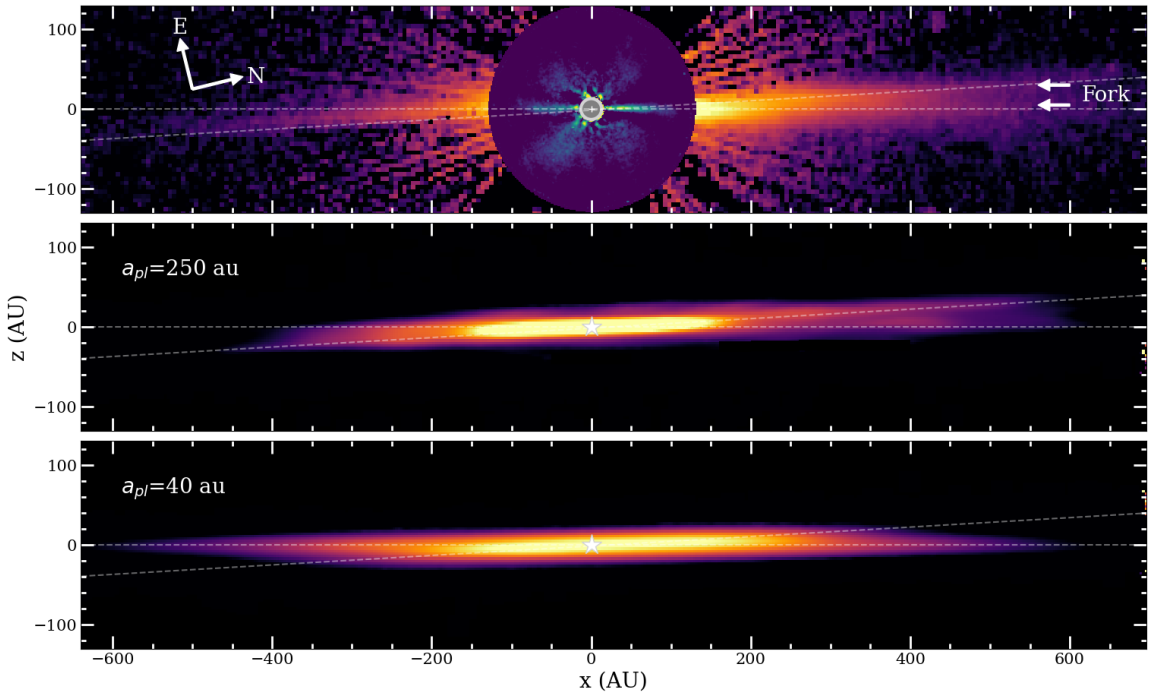

particle is also assigned a β value, where β is the ratio between the force of radiation pressure from the star (Burns et al., 1979) and the force of gravity ($\beta = F_{rad}/F_{grav}$). Radiation pressure is an important force for debris disks, as dust particles with a β greater than 0.5 will be blown out of the system. The β value is randomly selected from a distribution between 0.001 and 0.4 with a power law of 3/2 (equivalent to a dust grain size distribution power law of -7/2, Dohnanyi 1969), i.e. $dN/d\beta \propto \beta^{3/2}$, meaning that the size distribution is dominated by the smallest particles. Using equation 18 from Wyatt et al. (1999) and assuming compact astrosilicate grains with a dust particle density of 3.3 g/cm^3 (Draine, 2003), our chosen distribution of β values correspond to a particle size of $\sim$3 μm to 970 μm (0.97 millimeters). The initial configuration of our models can be seen in Figure 5.1.

Once all particles are added, the simulation is then integrated over 15 Myr, the estimated age of the system (Pecaut & Mamajek, 2016), using the Wisdom-Holman integrator, WHFast. Using REBOUNDx (Tamayo et al., 2020), radiation pressure is also turned on during this integration period.

5.1.2 Synthetic Scattered Light Images

To create synthetic scattered light images of our simulations, we follow a similar procedure to other disk simulation papers such as Nesvold et al. (2017) and Moore et al. (2023). This procedure involves populating the disk with more particles based on the orbit of the parent particles and then applying a scattering phase function (SPF) to simulate the surface brightness of the disk in scattered light.

In order to populate the disk with more particles, we first need to select the parent particles on which the new particles orbit will be based on. Since we do not track collisions in the disk, we instead randomly select 500 bound parent particles in the densest regions of the disk (i.e. $e_p < 1$ and close to the midplane where collisions are more likely to occur) with a range of true anomalies between 0 and 2π. We then generate 20 orbits for each parent particle based on their β value and orbital properties. Again, β for the new dust particles is assigned from a distribution with a power law of 3/2. In this case, the max β allowed is determined by the orbit of the parent particle as shown by the following equation (Burns et al., 1979; Wyatt et al., 1999):

$$\beta_{max} = \frac{1 - e_p}{2(1 + e_p \cos f_p)} \tag{5.1}$$

Here, e_p is the eccentricity of the parent particle, while f_p is the true anomaly of the parent particle. Once β is selected for each orbit, the rest of the orbital parameters are calculated including the semi-major axis (a), the eccentricity (e) and argument of pericenter (ω). Similarly, these parameters are calculated based on the parent orbit using the following equations (Burns et al., 1979; Wyatt et al., 1999):

$$a = \frac{a_p(1-e_p^2)(1-\beta)}{1-e_p^2-2\beta(1+e_p\cos f_p)} \tag{5.2}$$

$$e = \frac{\sqrt{e_p^2+2\beta e_p\cos f_p+\beta^2}}{1-\beta} \tag{5.3}$$

$$\omega = \omega_p + \tan^{-1}\left(\frac{\beta\sin f_p}{e_p+\beta\cos f_p}\right) \tag{5.4}$$

Here a_p and ω_p are the semi-major axis and argument of pericenter of the parent particle. Besides these parameters, we set the new particle inclination and longitude of ascending note to that of the parent particle ($i = i_p$ and $\Omega = \Omega_p$). We then generate 20 disk particles for each of the 20 generated orbits with randomly selected mean anomalies (M) between 0 and 2π for a total of 400 disk particles per parent particle.

Once the disk particles are generated, we then apply a Henyey-Greenstein (HG; Henyey & Greenstein 1941) SPF to measure the surface brightness of the disk. We first calculate the scattering angle which is defined as the angle between the incident light ray from the star and the scattered light ray from the disk particle in the direction of the observer. The scattering angle is calculated as $\cos^{-1}(z/d)$, where z is the position of the particle in the z direction and d is the total distance of the particle from the star. The scattering angle is then passed through the HG function which is defined below:

$$\phi(g,\theta) = \frac{1}{4\pi}\frac{1-g^2}{(1+g^2-2g\cos\theta)^{3/2}} \tag{5.5}$$

Where θ is the scattering angle and g is the asymmetry parameter. We use a 2-parameter HG function (g_1 and g_2) as it more accurately represents the SPF of Saturn's rings compared to a single HG function. This SPF has also been found to be similar to the SPF of many debris disks including HD 111520 (Hughes et al. 2018; Hom et al. 2024). Based on the SPF measurements done by Hedman & Stark (2015)

Figure 5.3: **Left:** Density map of the 250pl model face on **Right:** Density map of the 40pl model face on. The red points mark the final position of the planet for both models.

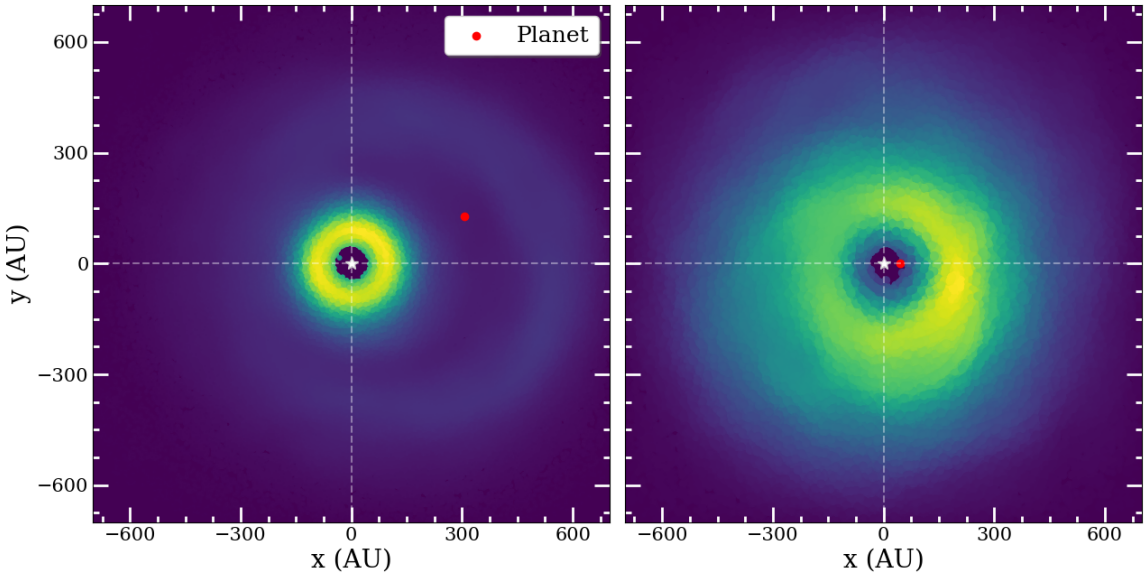

of Saturn's D68 ring, we choose $g_1 = 0.995$ and $g_2 = 0.325$ with weights $w_1 = 0.779$ and $w_2 = 0.221$, respectively. The final HG function is the sum of two weighted HG functions calculated with g_1 and g_2 (i.e. $\phi(g, \theta) = w_1\phi(g_1, \theta) + w_2\phi(g_2, \theta)$). The final surface brightness is measured as $\phi(g, \theta)/\beta^2 d^2$, where $1/\beta^2$ accounts for the geometric cross section for each disk particle. For our models, we do not consider multiple scattering of photons with the safe assumption that debris disks are optically thin.

Keeping ω_{pl} at 270°, the model is rotated about the x-axis to have an inclination of 89° based on empirical measurements of the disk (Crotts et al., 2022). The disk particles are then projected onto a 1400 au by 1400 au grid, which we bin into 450, 4 au by 4 au, bins. As a final step, we smooth the image with a Gaussian kernel with $\sigma = 1$ pixel. The final models for both simulations can be seen in Figure 5.2.

5.2 Results

We have created two synthetic scattered light models based on REBOUND simulations of a disk with a 1 Jupiter-mass planet with a semi-major axis of 250 au and 40 au, placing the planet slightly outside the warp and within the disk inner edge. Both planets are on eccentric, inclined orbits relative to the disk. For simplification, from

here on forward, we refer to the two models as the 250pl and 40pl models.

Figure 5.4: Synthetic scattered light image of the HD 111520 disk with 1 planet orbiting outside the warp ($a = 250$ au). The disk is rotated counter-clockwise by 45° intervals starting from $\omega_d = 270°$ all the way to $\omega_d = 225°$ **Left:** Representation of the disk as observed in the optical with HST/STIS **Right:** Representation of the disk as observed in the NIR with GPI. The rectangle in the top left figure represents the field of view of the NIR models.

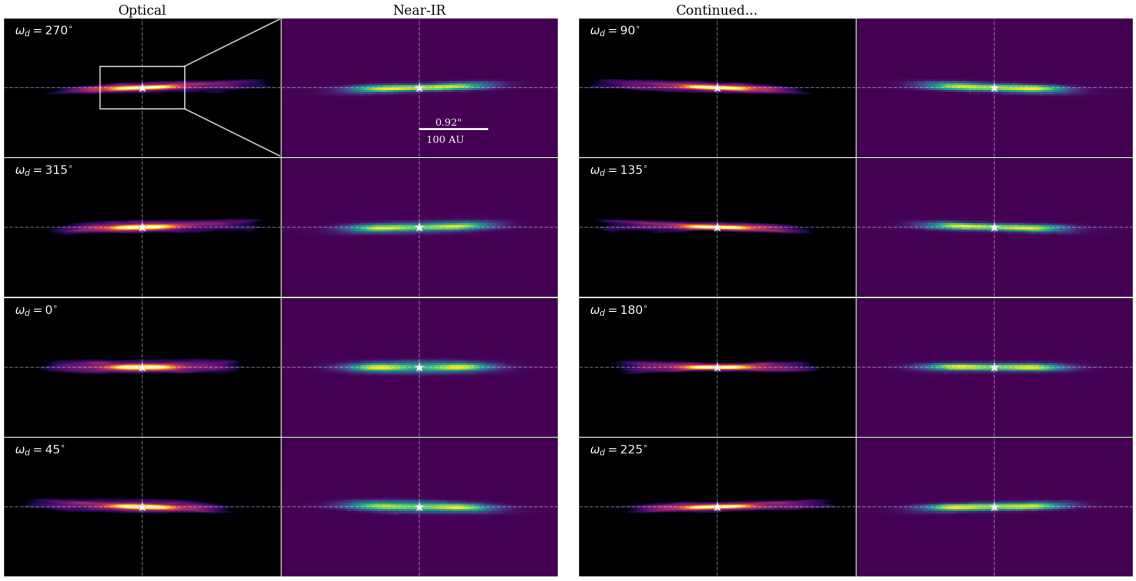

5.2.1 Planet Outside Warp vs. Inside Disk Inner Edge

First, to understand what is happening in our simulations, Figure 5.3 shows the relative density of both disk models which are orientated face-on. For the 250pl model, because the planet begins embedded in the disk, the planet effectively carves a gap in the disk due to the chaotic unstable zone surrounding the planet (Wisdom, 1980). This separates the disk into an inner and outer ring (which we refer to simply as the "inner ring" and "outer ring"), where the inner ring is significantly more densely populated than the outer ring. While the planet induces a visible eccentricity on the outer ring ($e \approx 0.3$), the inner ring remains relatively circular ($e \approx 0.03$) and appears axisymmetric. It is not entirely clear what the reason is for the significant difference in eccentricity between the inner and outer rings, although studies have shown that the chaotic zone external to the planet is much wider compared to the chaotic zone internal to the planet (Morrison & Malhotra, 2015), potentially leading to a greater effect on the outer ring from the planet compared to the inner ring. For the 40pl

Figure 5.5: Synthetic scattered light image of the HD 111520 disk with 1 planet orbiting within the disk inner edge ($a = 40$ au). The disk is rotated counter-clockwise by 45° intervals again starting from $\omega_d = 270°$ to $\omega_d = 225°$ **Left:** Representation of the disk as observed in the optical with HST/STIS **Right:** Representation of the disk as observed in the NIR with GPI. The rectangle in the top left figure represents the field of view of the NIR models.

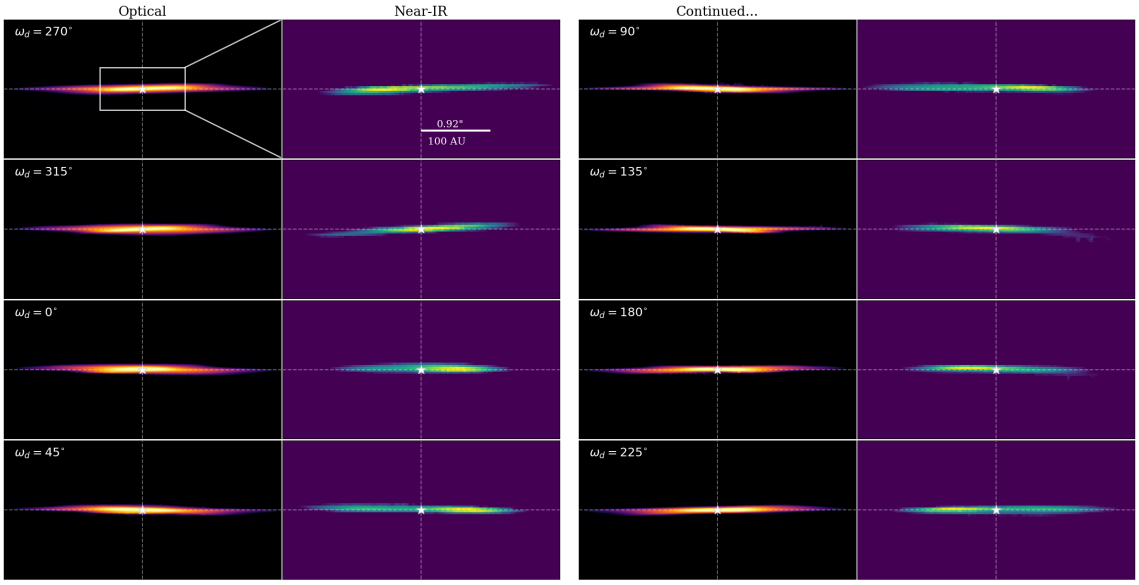

model, the planet begins within the disk inner edge and therefore does not carve a gap, although it does induce an eccentricity on the surrounding disk. The side of the disk near the planet's pericenter is closer to the star, while an over-density can be seen at the disk's apocenter. This is due to the fact that dust grains spend more time at apocenter, causing a pileup of particles at that location. Past 300 au, the 40pl model is fairly symmetric.

Comparing our inclined, synthetic scattered light models to HST/STIS observations of the disk halo, both scenarios are able to reproduce certain observed features including a warp due to the relative inclination of the planet to the disk. The angle of the warp in both cases is measured to be ∼3.3°, which is smaller than the observed 4°, meaning that the relative inclination of the planet is likely to be close to, but slightly greater than 2°. Both models also are able to produce a "fork"-like bifurcated structure. The source of the fork feature is due to the planet exciting the inclination of nearby disk particles, causing these disk particles to oscillate about the planet's inclined orbit by $\sim 2i_{pl}$ and create a second plane of the disk that extends from the warp location. The rest of the disk particles not affected by the planet

remain aligned with the disk midplane creating the second half of the fork.

At first glance, the 250pl model is a better representation of the HD 111520 disk compared to the 40pl model. For example, the top and bottom sections of the fork in the 250pl model extend to the same distance on the right side of the disk, while only the bottom fork is strongly seen on the left side, similar to the HST/STIS observations. The top part of the fork is still present on the left side, however, it is not as extended or bright as the bottom fork which is aligned with the warp induced by the planet. In the 40pl model, the fork is not strongly seen, and the top and bottom sections of the fork do not extend to the same distance on either side. In fact, the part of the fork that aligns with the planet inclination and warp, does not extend past 300 au. In addition to the mismatch of the fork, the 40pl model also does not exhibit the radial extent asymmetry observed. Both sides of the disk, which are aligned with the midplane, appear to extend similarly out to ∼650 au, likely due to the planet not being able to induce any eccentricity at these distances. The same cannot be said about the 250pl model, where the planet has strong influence on the outer ring causing a clear radial extent asymmetry, where the right side extends out to ∼600 au and the left side extends only to ∼400 au. Neither model appears to have a strong brightness asymmetry, although the 40pl model exhibits a modest pericenter glow on the left side of the disk caused by the planet's eccentric orbit. However, this is opposite of what is observed in the HD 111520 disk.

Based on these two models, the 250pl model does a better job of recreating the majority of the observed disk features including the fork, warp, and radial extent asymmetry. The only feature that it is not able to reproduce is the strong brightness asymmetry. However, this is based solely on one orientation of the disk, i.e when the argument of pericenter of the disk (ω_d) and the planet are 270°. Changing ω of the system by rotating the model counter-clockwise, may reveal a model that better matches the observed disk. Additionally, we can compare what our models might look like in the near infrared (NIR) with the GPI observations. To do this, we take a closer look at the disk within 200 au, where the micron sized particles of the disk are located as observed by GPI. We then isolate the slighter larger disk particles with $\beta < 0.2$, which are more concentrated close to the star in our models (see Section 5.6), in order to simulate the difference in dust grain sizes between the STIS and GPI observations. Similar to before, the model is inclined by 89°, binned into 4 by 4 au bins, and smoothed with a Gaussian kernel.

Figures 5.4 and 5.5 show our two models rotated counter-clockwise by 45° intervals

starting with the initial ω_d of 270°. Additionally, we keep the disk inclination at 89°. The left hand column for both figures show all the disk particles, which are highly dominated by the smallest particles, plotted within 650 au representing the disk as seen in the optical with STIS. The right hand column shows only the particles with $\beta < 0.2$ (r $\lesssim$ 5 μm), which are more concentrated in the inner regions of the disk, representing the disk as seen in the NIR with GPI. We find that the 40pl model cannot recreate the majority of disk features regardless of its orientation. While a radial and brightness asymmetry are present in the larger grains at certain orientations, the brightness asymmetry is still inconsistent, i.e. the side of the disk that is less radially extended is brighter. While this is expected for an eccentric disk, it is the opposite side of what is observed in the HD 111520 disk where the more radially extended side is the brighter side. In the optical, the 40pl model also continues to not harbour a radial extent asymmetry or a similar fork structure. Due to these consistencies, we eliminate the 40pl model as a possible scenario for the HD 111520 system.

Taking a look at the 250pl models in 5.4, we determine that the disk and planet ω are likely to be somewhere between ∼225° and ∼315°. In these models, the disk retains a similar radial extent asymmetry and fork-like structure as observed in the optical. However, despite changing the orientation, no brightness asymmetry is observed. This is also true for the disk in the NIR, where no brightness or radial asymmetry are present, likely due to the fact that the inner ring stays symmetric as seen in Figure 5.3. Therefore, while a planet on an eccentric, inclined orbit outside the warp location can easily create a similar warp, radial asymmetry and fork-like structure, another explanation is needed for the strong brightness asymmetry observed.

5.2.2 2 Planet Scenario

Although the 250pl model is able to replicate very well the disk structure observed in the optical, the NIR model does not present a radial or brightness asymmetry. On the other hand, the 40pl is able to create a radial and brightness asymmetry, although the brightness asymmetry is on the wrong side as observed. We therefore combine these two models in attempt to replicate the structure seen in the disk halo as well as the brightness and radial asymmetry seen in the NIR. To do this, we keep exactly the same planet as in the 250pl model, and add an additional planet inside the disk inner edge similar to the 40pl model. We keep the inner planet at a semi-major axis of 40 au, but decrease the mass to Saturn size and decrease the eccentricity to 0.3

Figure 5.6: Initial (**left**) and final (**right**) orbits (black ellipses) and positions of the planets (black dots) relative to the disk (colored dots) for our 2 planet model. The two planets start at their pericenters with $\omega_{pl} = 270°$ for the outer planet and $\omega_{pl} = 90°$ for the inner planet. After 15 Myr, the outer planet is near its apocenter with $\omega_{pl} \approx 290°$, while the inner planet is slightly past its pericenter with $\omega_{pl} \approx 180°$.

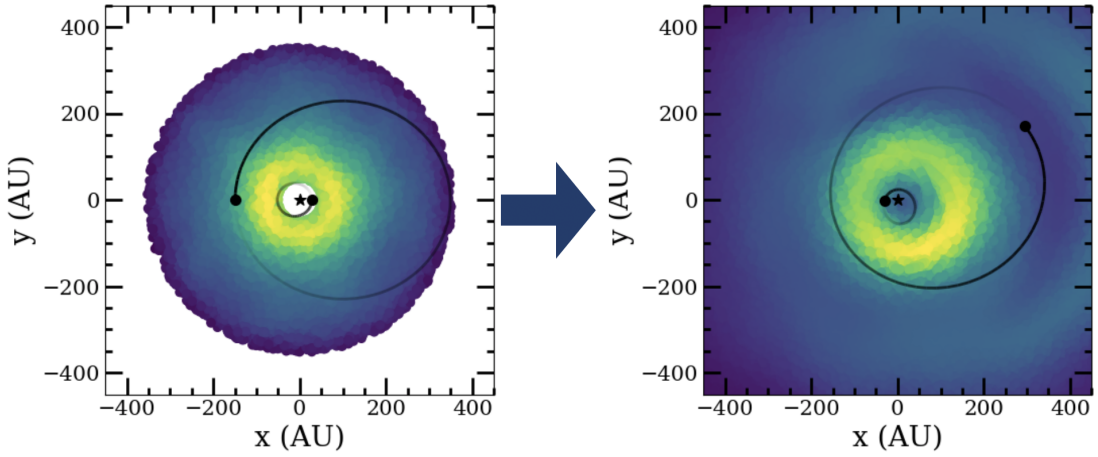

as a starting point. We also keep its orbit co-planar to the disk and define ω_{pl} to be 90° so that the inner planet's pericenter is on the right side relative to the observer. Our reasoning for these changes is to hopefully create a pericenter glow on the right side of the disk as observed without significantly warping the inner ring. The initial planet orbits and locations, as well as the location of the disk, can be seen in Figure 5.6.

With our setup described above, we find that the resulting model is similar to the 250pl model, however, we are still not able to reproduce the radial or brightness asymmetry when inclining the disk without rotating ω_d. This is surprising as the inner planet should induce some eccentricity on the inner ring. Taking a closer look reveals that due to secular perturbations from the outer planet, the argument of pericenter of the inner planet has shifted counter-clockwise from 90° to almost 180° by the end of the 15 Myr. Such a change may be due to the fact that anti-aligned planetary systems (where $\Delta\omega = 180°$) can be unstable, especially for planets with high eccentricities that are not in mean-motion resonances (e.g. Zhou & Sun 2003). The ω_{pl} of the outer planet also shifts, but not as significantly from 270° to ∼290°. No major changes in ω_{pl} are seen in the previous single planet models.

Because ω_{pl} of the inner planet is close to 180° meaning that the pericenter is facing away from the observer and therefore no brightness asymmetry would be observed without rotating the disk's ω relative to the observer. We therefore rotate the model

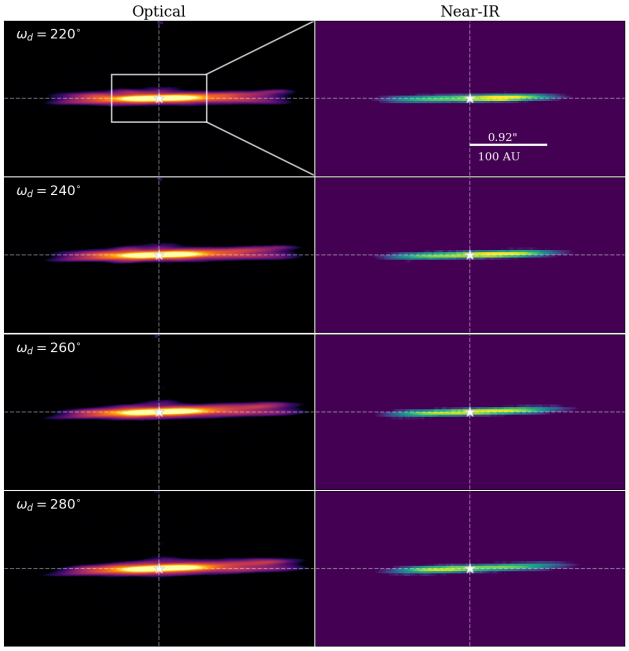

Figure 5.7: Synthetic scattered light image of the HD 111520 disk with 2 planets orbiting outside and inside the warp ($a = 250$ and $a = 40$ au, respectfully). The disk is rotated counter-clockwise by 20° intervals from $\omega_d = 220°$ to $\omega_d = 280°$ **Left:** Representation of the disk as observed in the optical with HST/STIS **Right:** Representation of the disk as observed in the NIR with GPI. The rectangle in the top left figure represents the field of view of the NIR models.

between 220° and 280° so that the fork and radial extent asymmetry are still visible and the pericenter of the inner planet is closer to the right side of the disk. As seen in Figure 5.7, we find that we are able to create a brightness asymmetry in the NW side with a $\omega_d < 260°$, which also becomes apparent the closer we get to $\omega_d = 220°$. However, at the same time, we begin to slowly lose the radial extent asymmetry, and the upper fork on the SE side starts to become more visible. Figure 5.8 shows our model with $\omega_d = 250°$, which is in between the middle two models shown in Figure 5.7. We choose to focus on this model as it still retains the fork, warp and radial asymmetry, but also harbours a brightness asymmetry similar to observations.

While our 2 planet model is able to replicate the majority of morphological features observed in the HD 111520 disk, there are still several caveats. In order to create the brightness asymmetry, the disk needed to be rotated so that $\omega_d < 260°$ in order for the inner planet's pericenter to be closer to the NW side. This causes the upper fork on the SE side to become more visible, whereas it is not seen in observations, meaning that ω_d and ω_{pl} of the outer planet needs to be closer to 270° when no brightness asymmetry is observed. Secondly, even when $\omega_d < 260°$, the brightness asymmetry is not as significant as observed. For example, using our $\omega_d = 250°$ model shown in Figure 5.8, we measure the surface brightness over rectangular apertures, similar to what is done in previous studies (Crotts et al., 2022, 2024). We find that the NW side is only 1.14 times brighter than the SE side in the NIR model, whereas the optical

Figure 5.8: Synthetic scattered light image of the HD 111520 disk with 2 planets orbiting outside and inside the warp. The disk is rotated count-clockwise so that $\omega_d = 250°$. The full disk is shown on larger scales, simulating STIS observations, while the larger disk particles are shown in the center, simulating GPI observations. The disk still exhibits the fork, warp and radial asymmetry, however, the inner planet has also created a brightness asymmetry on the NW side. The white dashed lines trace the "fork"-like structure and warp induced by the outer planet.

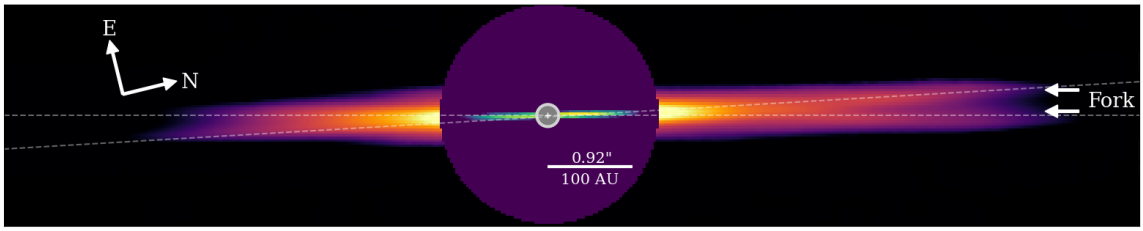

model shows no brightness asymmetry at the chosen aperture location (between 100 and 300 au, outside the HST coronagraphic mask). This is significantly lower than the 2 to 1 brightness asymmetry seen in GPI and the 5 to 1 brightness asymmetry seen with STIS. Even when rotating the disk so that ω_{pl} of the inner planet is at 90°, when we would expect the largest brightness asymmetry, only yields a 1.2:1 brightness asymmetry, again not close to the 2:1 asymmetry observed.

It is important to note that our results of the 2 planet scenario are merely based on one configuration. It is possible with different orbital configurations and planet masses/eccentricities that we could achieve a larger brightness asymmetry more similar to observations, although this is outside the scope of our study. For now, we show that a planet near the warp location is able to create a similar fork, warp and radial asymmetry, while an additional inner planet is able to create a brightness asymmetry with a brighter NW side. While our model is not perfect, so far, no other model has been able to replicate all of these features, making the HD 111520 system the perfect hunting ground for new directly imaged planets.

5.3 Further Constrains on the Outer Planet Properties

We presented three planet-disk models in attempt to explain the unique and complicated morphology of the HD 111520 debris disk. We find that 1 M_{jup} planet on an inclined and eccentric orbit with a semi-major axis of 250 au is better at recreating

the disk morphology compared to the same planet with a semi-major axis of 40 au, i.e. within the disk inner edge. We also find that at least one other planet is required to create a brightness asymmetry, although it is unclear whether this scenario is able to create a brightness asymmetry as extreme as observed. Despite this, our models show that planets can effectively create a similar complex morphology seen in the HD 111520 disk, and that planets may be responsible for other disks showing similar asymmetries and structures. Additionally, these models allow us to constrain the potential planet mass and orbit, which is important for understanding the feasibility of detection by current and future instruments.

From our models, we know that the orbit of the outer planet is likely inclined by close to 2° relative to the disk in order to produce the warp and fork, as well as likely eccentric in order to produce the radial asymmetry seen. We also know that a 1 M_{jup} planet with a semi-major axis of 250 au is sufficient to replicate the disk halo structure. However, to understand the feasibility of detecting this planet, it is important to further constrain its potential mass and location. In the next few Sections we take our 250pl model and vary the planet mass and semi-major axis with the goal of better constraining these properties.

5.3.1 Outer Planet Mass

Although it is possible that there are one or more planets within the disk inner edge causing the brightness asymmetry observed, here we focus solely on the outer planet. While the brightness asymmetry is difficult to recreate without testing multiple different orbital configurations and planet masses, the outer planet is consistently able to reproduce the structure of the disk halo including the warp, fork and radial asymmetry. We therefore test the mass of the outer planet to see whether or not planet masses below or above 1 M_{jup} can also create a similar disk morphology. The current planet mass limit set by GPI is $\sim$3 M_{jup} for separation $>$ 10 au (Nielsen et al., 2019).

For simplicity and consistency, we use our 250pl model with the single planet orbiting with a semi-major axis of 250 au. We keep the planet orbit exactly the same, only changing the planet mass. We test several different planet masses outside of 1 M_{jup} including 2 M_{jup}, 0.5 M_{jup} and 1 Saturn mass ($\sim$0.3 M_{jup}). Each simulation is run exactly the same as before and the synthetic scattered light images are also produced the same way. Again, we focus mainly on whether or not the planet can produce the warp, fork and radial asymmetry as observed in the HD 111520 disk halo,

ignoring the presence or absence of a brightness asymmetry.

The resulting models can be found in Figure 5.9, where similar to previous figures, the model is orientated with $\omega_d = 270°$. The center of the disk for each model is masked in order to solely focus on the outer structures of the disk. We find that the 2 M_{jup} model is very similar to the 1 M_{jup} where the upper and lower fork on the right side of the disk, as orientated in 5.9, radially extend to the same distance. Transitioning to lower planet masses, a clear trend emerges. Comparing the different models, the lower fork on the NW side that is aligned with the midplane appears to change, becoming more dim in the 0.5 M_{jup} and 1 Saturn mass models. This result is unexpected and counter-intuitive, as one might expect the upper fork, which is directly influenced by the planet, to be the one affected. One possible explanation, is that the lower fork in the NW is correlated with the amount of disk particles the planet is able to clear within the gap, given that the lower mass planets are unable to carve as deep of a gap within the same time span. Indeed, when comparing the number of disk particles in the gap versus the outer ring on the extended side of the disk near the midplane (z <20 au) for the 1 and 0.5 Jupiter mass planet models, we find that there are ∼1.5 times more particles in the outer ring compared to the gap for the 1 Jupiter mass planet model, where the opposite is true for the 0.5 Jupiter mass planet model (see Figure 5.14). Additionally, there are overall ∼1.5 times more particles near in the midplane in the outer ring of the 1 Jupiter mass planet model compared to the 0.5 Jupiter mass planet model. Similar analysis of the upper fork on the radially extended side of the disk reveals no significant difference in the number of particles between the two models. In summary, the planet mass does not significantly change the number of disk particles excited onto inclined orbits, but does affect the number of disk particles pushed out from the gap into the outer ring near the disk midplane.

In order to compare which model best represents the data, we attempt to quantify the difference in brightness between the top and bottom fork on the NW side. We first measure the actual difference in brightness and uncertainty between the top and bottom fork using the HST/STIS observations. Similar to measuring the brightness asymmetry between the NW and SE sides of the disk, we place two rectangular apertures centered on the top and bottom fork between 450 and 550 au from the star, close to the edge of where the fork is still visible in the data, with a height of 14 au. Once the apertures are placed, the flux is integrated over the aperture and summed. We then divide the summed flux of the bottom fork by the top fork. To measure the

Figure 5.9: Synthetic scattered light images of the HD 111520 disk with 1 planet orbiting outside the warp with varying masses: 2 M_{jup} (**top**), 0.5 M_{jup} (**middle**) and 0.3 M_{jup} or 1 Saturn mass (**bottom**). The star represents the location of the HD 111520 star, and the center of the disk is masked to highlight the outer structure including the fork. As the planet mass decreases, the fork that is aligned with the midplane slowly starts to disappear on the NW side.

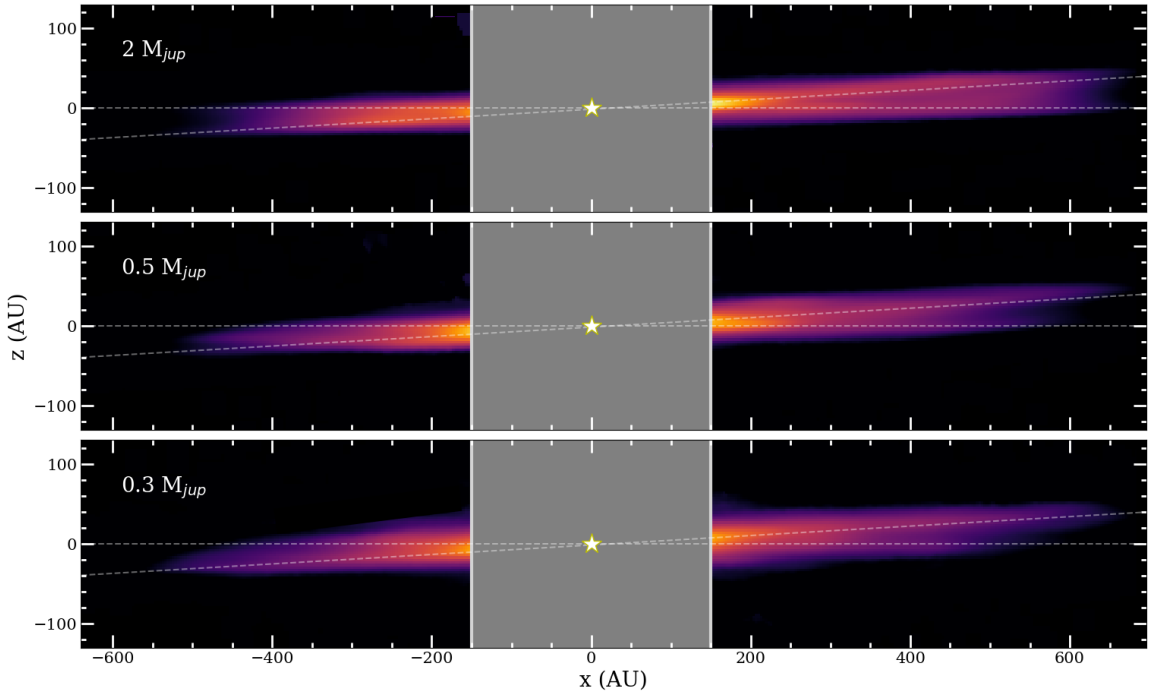

uncertainty, we use the same two rectangular apertures and place them well above and below the disk emission, but at the same separation from the star (450 to 550 au). Again the flux is integrated over the aperture and summed, where the uncertainties in flux are then propagated to measure the uncertainty in the difference in flux between the top and bottom fork. Using this procedure, we find that the upper fork is roughly 1.02±0.28 times brighter than the bottom fork at this distance, meaning that both the upper and lower fork are of similar brightness at these distances.

We conduct the same analysis for our various planet mass models, including the 1 M_{jup}, using the same rectangular apertures. From 2 M_{jup} to 0.3 M_{jup}, the brightness of the lower fork compared to the upper fork consistently decreases. For the 2 and 1 M_{jup} planet models we find the upper fork to be marginally brighter than the lower fork, where the upper fork is 1.24 and 1.13 times brighter than the lower fork, respectfully. From here the brightness asymmetry increases to 1.70 for the 0.5 M_{jup} and 2.7 for the 0.3 M_{jup} planet models. Based on these values, the 1 and 2 M_{jup}

models are the most consistent with observations within 1σ uncertainties, while the models with a 0.5 Jupiter mass and 1 Saturn mass planet produce a lower fork that is much too dim. Given these measurements, we therefore put a lower mass limit on the outer planet of $\sim$1 M_{jup}.

5.3.2 Outer Planet Semi-Major Axis

Observations of the disk halo with STIS show that the disk is initially aligned with the midplane, before warping by 4° from the midplane at $\sim$180 au from the star, while the fork feature becomes prominent beyond $\sim$245 au (Crotts et al., 2022). We therefore test where these structures are seen in our REBOUND models, and compare how they change with the planet semi-major axis. Keeping the same model setup as in the previous Section with a constant planet mass of 1 M_{jup}, we only change the planet semi-major axis (a_{pl}). We compare the final disk model when a_{pl}=150, 200 au, 250 au, and 300 au. We note that we are not trying to perfectly replicate the disk, but rather place some constraints on the possible orbit of the outer planet.

To determine the location of these structures, we use a similar method to Crotts et al. (2022) by fitting a Gaussian profile to the disk surface brightness along vertical slices of the disk at varying radial separations, i.e. measuring the vertical offset of the disk from the star. We focus primarily on the NW side of the disk (the radially more extended side) where the fork structure is detected. Between 0 and 240 au from the star, we fit a single Gaussian profile to our synthetic scattered light models, while we also fit a double Gaussian profile beyond 150 au to capture the location of the fork. Figure 5.10 shows the measured vertical offset for the 250 au planet model as an example.

When a_{pl} = 150 au, i.e. the planet is orbiting inside the warp location, we find that the inner ring almost disperses completely, leaving only the disk component outside the orbit of the planet which is at large separations from the star. This is inconsistent with observations with GPI, where the inner disk radius is estimate to be $\sim$50 au. Additionally, the lack of an inner ring results in similar issues as the 40pl model, where due to the planet's pericenter on the left (SE) side of the disk, a pericenter glow is observed in scattered light on the left side instead of the right side as observed. The fork also becomes less defined compared to the other models, making it difficult to fit a double Gaussian profile. We therefore completely rule out a scenario where the planet is orbiting within the warp location.

Figure 5.10: Vertical offset profile for the 1 M_{jup} planet model. The dark blue data points represent the vertical offset measured using a single Gaussian, while the orange data points represent the vertical offset profile measured using a double Gaussian to highlight the fork structure. The grey vertical line represents the relative location where the upper fork converges with the lower fork (∼175 au). The dashed horizontal grey line highlights an offset of 0.

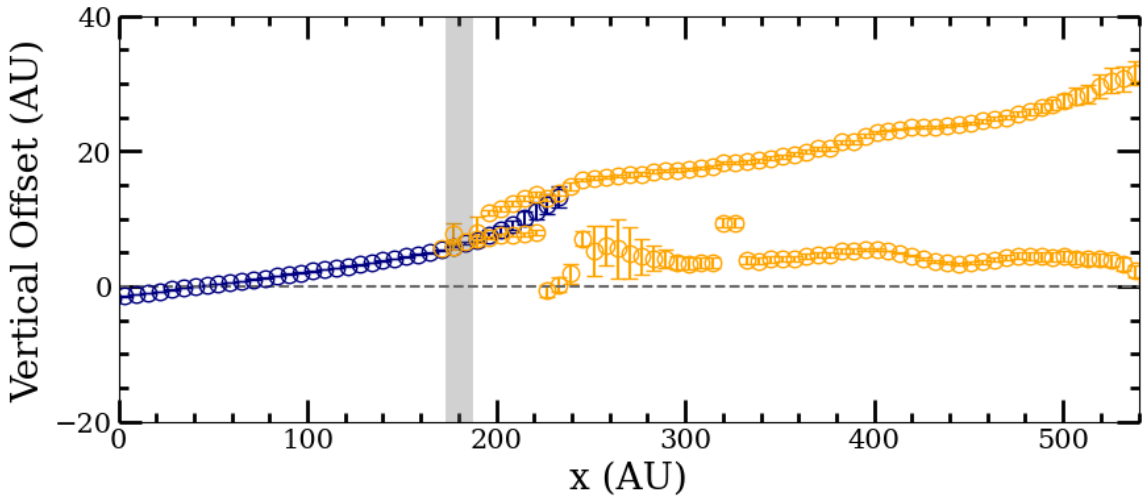

Figure 5.11: **Top:** Dust density images of our disk model seen face on, using a 1 M_{jup} planet with various semi-major axes (from left to right: a_{pl} = 150 au, 200 au, 250 au, and 300 au). The white dashed line in each plot highlights the location of the peak density of the inner ring for the 200, 250, and 300 au models, while the orange shaded line highlights the location where the upper and lower fork converge on right side for the same three models (∼180 au). The density is scaled to have similar brightness between each frame. **Bottom:** Particle density of the inner rings for the 300 au (blue), 250 au (cyan), and 200 au (magenta) models plotted as a function of distance from the star along the x-axis. The dashed vertical lines represent the radius of the peak density of the inner ring for the model with the corresponding color.

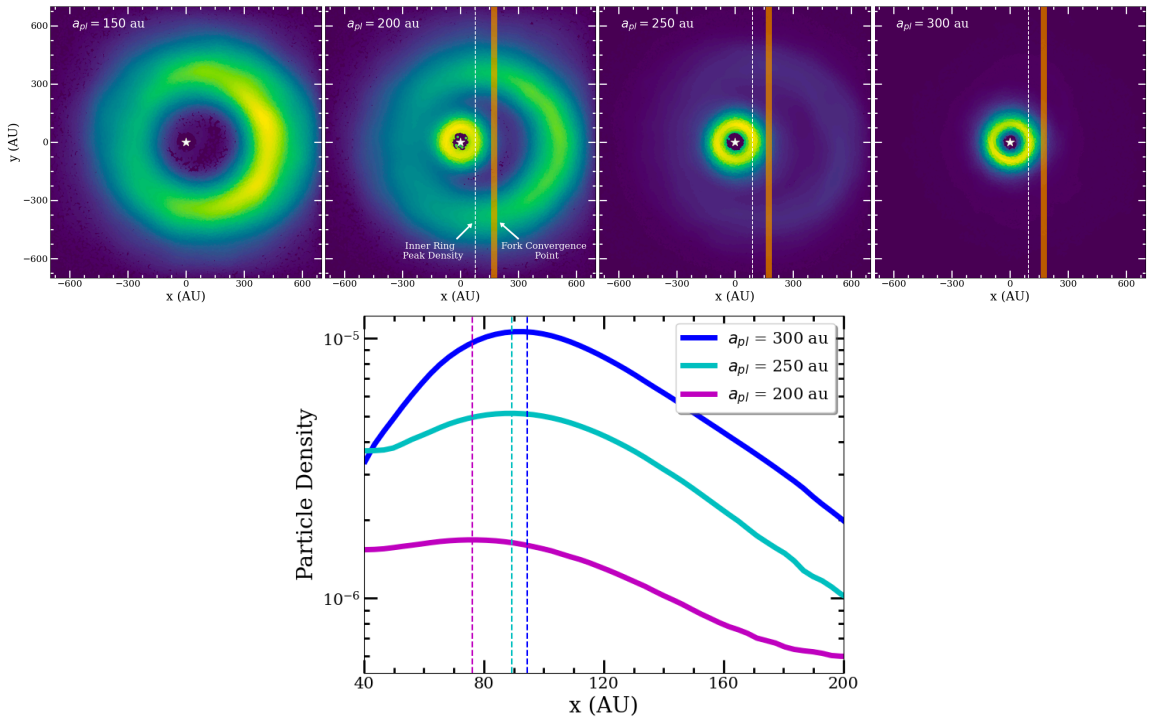

For the remaining three models, comparing the location where the upper and lower fork converge, we find that in all cases, the fork begins at roughly the same location (∼180±5 au) regardless of the planet semi-major axis. The convergence of the upper and lower fork in all three cases also appear to coincide with the outer edges of the inner ring, suggesting that the location of the inner ring may determine how far we can observationally probe the fork structure as seen edge-on in scattered light, given that the inner ring is much brighter than the fork. To investigate this correlation further, we look more closely at how the semi-major axis affects the inner ring by measuring its radial density profile.

Figure 5.11 shows the resulting density of the disk for each model with the disk

is oriented face on, alongside the radial density distribution of the inner ring for each model vs. distance from the star along the x-axis. We find that there are three properties of the inner ring that change with planet semi-major axis: The ring's density; location of the peak density; and its FWHM. Going from a smaller semi-major axis to a larger semi-major axis, the inner ring becomes more dense as less disk particles in this region are swept out by the planet, while the outer ring becomes relatively less dense. At the same time, the radius of the peak density of the inner ring increases slightly from ∼76 au to ∼95 au, while the FWHM of the inner ring decreases from ∼114 au to ∼90 au. This can be seen on Figure 5.11, where the peak density of the inner ring appears to move outward with a_{pl}, while also decreasing in width. One explanation for these correlations is that as a_{pl} decreases, the inner ring becomes more truncated as the chaotic zone around the planet moves in, also resulting in the removal of more disk particles closer to the star. This would explain why the peak density of the inner ring moves in, and why there are less particles in the inner ring as the planet's orbit decreases. The increase in the FWHM as a_{pl} decreases may be due to increased stirring of particles in the inner ring, where a wider disk indicates a higher level of stirring due to an increased distribution of particle eccentricities (Mustill & Wyatt, 2009). Due to the relationship between the inner ring location and FWHM with increasing a_{pl}, the outside of the inner ring remains at relatively the same radial distance from the star. This means that the fork, as viewed in scattered light from edge on, becomes distinct at the same location for all three models.

Regardless of the differences between the three models, for all cases, the fork structure begins closer to the star than observed with STIS by ∼60 au. However, it is unclear if this difference is real or due to our model setup or optical affects making it difficult to probe the fork fully in the observations. In either case, the main importance is that the fork in our models (a_{pl}=200, 250 and 300 au) is present at the location seen in the data (>245 au) while not compromising the rest of the disk morphology. We therefore place a lower limit on the planet semi-major axis at approximately 200 au.

5.4 Discussion

In the previous Section, we are able to use the disk morphology to place some constraints on the planet mass and semi-major axis, based on how varying these parameters affects different disk structures. Here, we discuss the implications of our results,

and what they might mean for planet detectability, as well as the evolution of the system as a whole.

5.4.1 Alternative Explanations

With our n-body simulation setup, we demonstrate that the HD 111520 debris disk morphology can be mostly reproduced with a single Jupiter mass planet on an eccentric, inclined and wide orbit. However, one feature of the HD 111520 disk we are not able to replicate is the extreme brightness asymmetry observed in both the optical and NIR. While the addition of an inner planet with the right orbital configuration is able to create a brightness asymmetry without significantly altering the rest of the disk morphology, the resulting brightness asymmetry is not as strong as observed and is not observed in the disk halo. An extremely eccentric planet may be required to create a 2 to 1 brightness asymmetry, but such a planet is not supported by the data. For example, Crotts et al. (2024) found that the eccentricity measured from the GPI data, either through the disk geometry or the 11 au difference in the peak polarized intensity as measured in Crotts et al. (2022), would not be able to reproduce as strong of a brightness asymmetry. It is therefore possible that another mechanism is required.

One alternative scenario is a recent giant collision between two rocky bodies, which is discussed briefly in Crotts et al. (2022) and also explored in depth by Jones et al. (2023). Although Jones et al. (2023) find that a giant collision scenario is also able to reproduce a fork, radial and brightness asymmetry, their model has similar issues with our model, in that it is not able to properly reproduce the brightness asymmetry. This discrepancy is due to the fact that in order for the NW side to be bifurcated and more radially extended, the collision needs to take place on the SE side. However, this then leads to a brighter SE side, which is the opposite of what is seen in observations. Instead, it is possible both mechanisms are required to produce the structure of the disk while also producing the extreme brightness asymmetry. If the collision point location is instead located on the NW side, this may be able to explain the extreme brightness asymmetry, as well as the difference in disk color measured Crotts et al. (2022) where the NW side is significantly more blue than the SE side at shorter wavelengths indicating a larger concentration of small dust grains (e.g. (Boccaletti et al., 2003)). Future work would be required to test whether or not this is a plausible theory for HD 111520, although a similar scenario can be found

through the β Pic disk, which harbours both a warp driving planet and a suspected recent giant collision (Dent et al., 2014). Given the similarities between HD 111520 and β Pic, the HD 111520 disk makes a good candidate for JWST/MIRI observations to search for similar structures in the disk emission such as the famous "cat tail" seen in β Pic which is thought to be one result of the giant collision (Rebollido et al., 2024).

5.4.2 Outer Planet Detectability

If there is indeed a planet orbiting at wide separations in the HD 111520 system, the question then becomes whether or not we can detect such a planet with the constraints placed on the mass and orbit. Based on the resulting disk morphology, we placed a lower limit of $\sim$200 au (1.9″) for the planet's semi-major axis. At this distance, the planet is not detectable through methods such as transit or radial velocity which require the planet to be much closer to the star. Because HD 111520 is a young system (15 Myr) and the planet is at a wide separation, direct imaging would be the best method for detection as the planet would still be warm from formation. In this case, a high-contrast imaging instrument in the optical/NIR with a wide field of view (FOV) would be required.

Four such instruments consist of (but not limited to) the STIS instrument on HST, GPI, the Spectro-Polarimetric High-contrast Exoplanet REsearch (SPHERE) on the Very Large Telescope, and the NIRCam instrument on JWST. In the case of HST/STIS, GPI, and VLT/SPHERE, all three instruments have already imaged the disk and have not detected any planets (Padgett & Stapelfeldt, 2015; Nielsen et al., 2019; Xie et al., 2022). In the case of HST/STIS, the disk halo almost completely covers the planet's orbit, alongside the fact that planets are not hot enough to emit significantly in the optical, meaning that the NIR would be more ideal for detection. The lack of detection with GPI is likely due to its small FOV (2.8″ by 2.8″) while lack of detection with SPHERE is likely due to the mass of the planet, where even young 1-2 M_{jup} planets tend to have a lower temperature compared to their more massive multi-Jupiter sized counterparts, therefore requiring a very deep contrast which is difficult for most current instruments to achieve. JWST/NIRCam therefore provides the best chance to observe this planet, as the instrument has a large FOV (10″ by 10″) and can achieve deeper contrasts than other high-contrast imagers.

To calculate whether or not we can observe the proposed outer planet with NIR-

Cam, we compute planet mass sensitivity curves for the F444W filter (λ_c = 4.44 microns). We choose the F444W filter as it has been shown to be the most sensitive filter for detecting planets (Carter et al., 2023). We also assume the use of both reference differential imaging (RDI) and angular differential imaging (ADI), as RDI+ADI has been shown to reach the most sensitivity compared to ADI alone. We initially use the code panCAKE (Carter et al., 2021) to create 5σ contrast curves, and find that between 200 au and 300 au ($\sim$1.9$''$-2.8$''$) we are able to achieve a contrast of between 1e-6 and 2e-6. Inputting these contrasts into a planet evolutionary code (ATMO; Phillips et al. 2020), we find for a 15 Myr system, NIRCam is able to reach a planet mass of 1 M_{jup} with a $\sim$75% probability of detection at the given separations.

Our calculations show that JWST/NIRCam in the F444W filter can detect lower mass planets than the lower limit established between 200 and 300 au by our simulations. Even so, there may still be some concerns with the planet's detectability. One being the interference from the disk. Because we are considering NIR observations, the disk should not have a significant impact as the micron sized grains are more radially compact than the sub-micron sized grains as seen in the optical with HST. Additionally, because the planet's orbit is close to edge on, this means that it may be located at small separations from the star within NIRCam's inner working angle ($\lesssim$60 au) irrespective of where the planet is in its orbit. While this is definitely possible, because the planet is likely eccentric given the radial extent asymmetry observed in the disk, it is statistically more likely to be near apocenter as it would spend the majority of time here (P $\approx$ 3523 years for a 1 M_{jup} planet with a_p=250 au). Therefore, JWST provides an excellent opportunity to detect the warp driving planet predicted by our models.

5.4.3 Implications on Planet Formation and Evolution

In addition to assessing the planet's observability, the constraints placed on the planet's mass and orbit also provides information on its formation and evolution. Given that the planet is highly aligned with the disk (again, $\Delta i \approx 2^\circ$), it is most likely that the planet formed within the disk. One of the main questions that arises then is how did the planet end up on such a wide and eccentric orbit? One possibility is that the planet formed via disk fragmentation (Toomre, 1964; Goldreich & Lynden-Bell, 1965), as this formation method is able to form wide orbit sub-stellar companions with a wide range of eccentricities. However, with a planet mass of $\sim$1

M_{jup}, formation through gravitational instability is less likely to be the case as this method is preferred for formation of more massive companions such as brown dwarfs (e.g. Kratter & Lodato 2016; Forgan & Rice 2013). Additionally, while sub-stellar companions formed via disk fragmentation may start out aligned with the disk, studies show that over time these companions are likely to become misaligned due to interactions with other companions in the system (Stamatellos & Whitworth, 2009). This is supported by the fact that brown dwarfs have been observed to have a high likelihood of misalignment from the star and a wide range of eccentricities (Bowler et al., 2020, 2023; Nagpal et al., 2023). On the other hand, the same studies also found that wide-orbit, directly imaged planets are much more likely to be aligned with their star and have a lower range of eccentricities.

Another possibility is that the planet formed via core accretion, a mechanism that prefers the formation of smaller planets compared to disk fragmentation (Goldreich et al., 2004). While this mechanism is more likely to result in a 1 M_{jup} planet that is coplanar, one issue with this scenario is that it does not explain the planet's wide and eccentric orbit. For example, planets observed between 10 and 100 au through the GPIES campaign tend to have orbits closer to 10 au compared with the observed brown dwarfs (Nielsen et al., 2019). In this case, another mechanism is required to explain the high eccentricity and large semi-major axis. A possible explanation is that the planet at some point was scattered outward onto a high eccentricity orbit through dynamical interactions with another object. A similar scenario is theorized for the planet-disk system, HD 106906, where the directly imaged planet is thought to have scattered to its current position ($\sim$730 au from the star; Bailey et al. 2014) due to interactions with the close central binary (Rodet et al., 2019). In the case of HD 111520, while the system does have a stellar companion, it is widely separated ($\sim$17000 au) with a PA of 78° (Mason et al., 2012) meaning that it is unlikely to be the culprit of scattering. Instead, the planets orbit may point towards scattering with another planet in the system, a process which is thought to be common for giant exoplanets (e.g. Chatterjee et al. 2008; Bitsch et al. 2020). Therefore, the constrained orbit and mass of the outer planet in our models may further suggest the presence of an inner planet in the HD 111520 system.

5.5 Conclusion

In this study, we model the highly asymmetric debris disk around HD 111520 using the n-body simulation code REBOUND, with the goal of determining what kind of planet(s) can reproduce the disk morphology, if any. We find that $\sim$1 M_{jup} planet on a wide and eccentric orbit that is also inclined by $\sim$2° relative to the disk, is able to produce a warp, "fork"-like structure, and radial asymmetry. We compare two models where a_p=40 au and 250 au, and find that the planet with a_p=250 is much better at replicating the overall disk morphology and is likely to have an argument of pericenter close to 270°. While an inner planet may be required to create a brightness asymmetry between the NW and SE sides, we are unable to replicate the strength of the brightness asymmetry observed, suggesting that another mechanism (in addition to the outer planet) may be needed, such as a giant collision similar to the β Pic disk.

In an attempt to further constrain the properties of the planet, we vary the outer planet's mass and semi-major access to see how this affected the morphology of the disk. We find that as the planet mass decreases, the brightness of the lower fork on the NW side also decreases. Comparing the brightness between the upper and lower fork of our models compared to HST/STIS observations, we find that for planet masses below $\sim$0.5 M_{jup}, the lower fork becomes too dim relative to the upper fork within 1σ uncertainties. We also find that for $a_p \lesssim 200$ au, the inner ring becomes almost entirely cleared, creating a disk morphology inconsistent with observations. We therefore place lower limits on the planet mass and semi-major axis at $\sim$0.5 M_{jup} and $\sim$200 au, assuming that the planet eccentricity is $\approx$0.4. These constrained parameters, alongside its mutual inclination with the disk, would suggest that the planet was formed within the disk and was scattered, likely by another planet, to its current location.

The HD 111520 debris disk is a unique system, and provides an excellent opportunity to study disk-planet interactions. We demonstrate how the complex morphology of the disk can be used to infer an unseen planet, as well as constrain certain planet properties such as the mass and orbit. This work also demonstrates how disk structures such as warps and "forks" may be the best signposts for planets compared to other disk asymmetries such as brightness asymmetries. Finally, HD 111520 makes a great candidate for future observations with JWST NIRCam to search for our warp-driving planet and thereby add another system to the small list of directly imaged disk and planet systems.

Figure 5.12: Radial density distribution of massless disk particles with different β values in our 250pl model. **Left:** Distribution of particles with $\beta < 0.1$. **Middle:** Distribution of particles with $0.1 < \beta < 0.3$. **Right:** Distribution of particles with $\beta > 0.3$. For all three frames the density is scaled the same in log space,

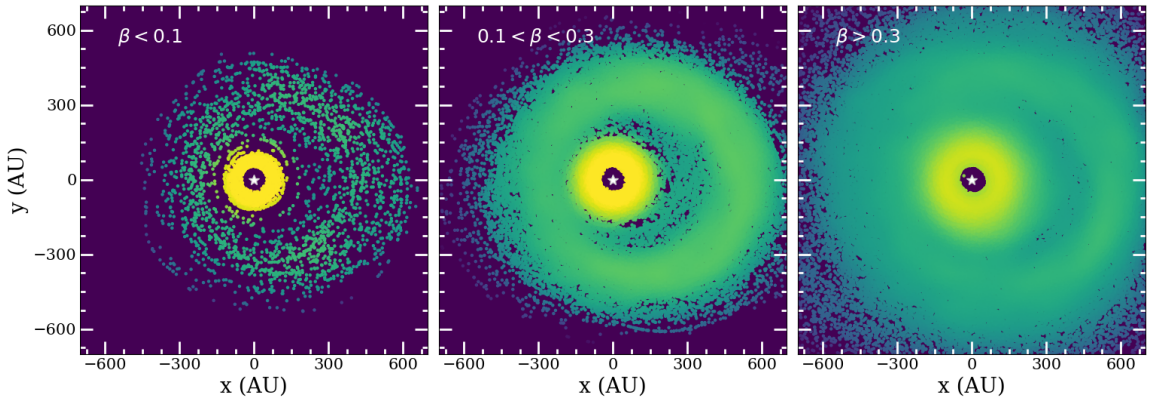

5.6 Additional Figures

5.6.1 Radial Distribution vs. β

In Figures 5.12 and 5.13, we show the radial density distribution of the massless disk particles with different β values in both our 250pl and 40pl models. In both cases, the larger disk particles with smaller β values are more concentrated closer to the star, while the smaller particles with larger β values are more spread out as expected. For the 250pl model, which has an inner and outer ring component, the largest disk particles are most concentrated in the inner ring, while significantly less particles occupy the outer ring. As β increases, the majority of disk particles are still concentrated in the inner ring, although a significant number of these small disk particles also populate the outer ring as well.

5.6.2 Radial Distribution vs. Planet Mass

in Figure 5.14, we show the radial distribution of disk particles within 20 au of the disk midplane for the 1 and 0.5 Jupiter planet mass models. For the 1 Jupiter mass model, we find that the gap is relatively more cleared of disk particles, where more particles are pushed out into the outer ring. Oppositely, we find that less disk particles are cleared from the gap, and consequently, less disk particles occupy the outer ring.

Figure 5.13: Radial density distribution of massless disk particles with different β values in our 40pl model. **Left:** Distribution of particles with $\beta < 0.1$. **Middle:** Distribution of particles with $0.1 < \beta < 0.3$. **Right:** Distribution of particles with $\beta > 0.3$. Again, for all three frames the density is scaled the same in log space.

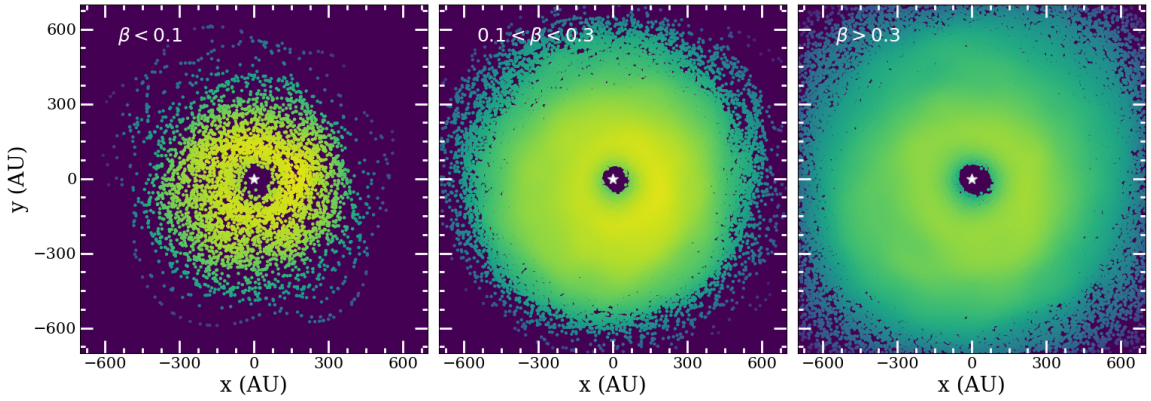

Figure 5.14: Radial density distribution of massless disk particles within 20 au of the disk midplane for our single 1 Jupiter mass model **left** and our single 0.5 Jupiter mass model **right**. The white dashed box highlights the location where the radial distribution of the disk particles differs between the two models. In both frames the density is scaled the same in log space.

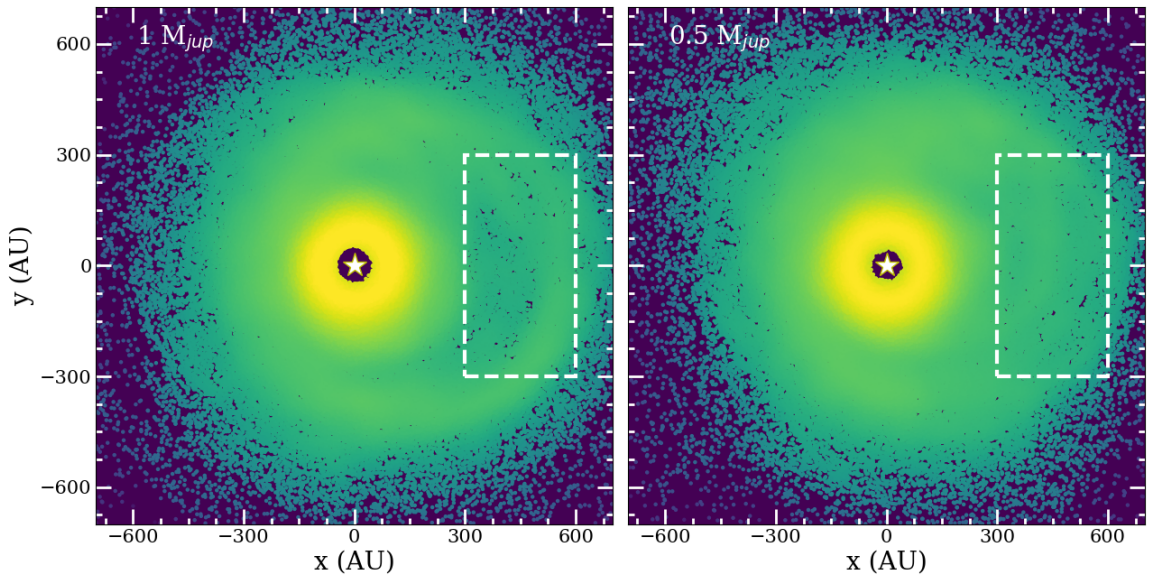

Chapter 6

Conclusions

Through my thesis, I studied the diversity of debris disk morphologies using GPI polarized intensity observations, and used these morphologies to determine the possibility of hidden planet perturbers. I presented a uniform, empirical analysis of 23 debris disks observed through GPIES, and took a deeper look at one of the most asymmetric disks, HD 111520. Finally, I performed N-body simulations with REBOUND in order to simulate the HD 111520 disk and constrain the properties of potential planets in the system. In this Chapter, I briefly summarize the findings of Chapters 3-5.

6.1 A Uniform, Empirical Analysis of GPI Debris Disks

Using GPI polarized intensity observations in multiple wavelengths, I presented a uniform analysis of the morphology of each disk to find asymmetries suggestive of perturbations, particularly those due to planet-disk interactions. Through this analysis, I measured the multi-wavelength surface brightness, the disk color and geometry, where the disk geometry permits identification of any asymmetries such as warps or disk offsets from the central star. I find that nineteen of the disks in this sample exhibit asymmetries in surface brightness, disk color, disk geometry, or a combination of the three, suggesting that for this sample, perturbations, as seen in scattered light, are common.

Out of the 23 disks, 5 are consistent with an eccentric disk, meaning that the disk offset measured in the geometry is consistent with the measured surface brightness asymmetry. An additional 4 disks are also consistent with an eccentric disk, but have

much larger brightness asymmetries than expected, meaning that another mechanism may be required. In either case, an eccentric disk may be a sign of an eccentric planet perturber. 3/23 disks have other interesting features such as a clump, spiral arm, and tentative warp, where the latter two are structures associated with planet-disk interactions. Another 3/23 disks have significant brightness asymmetries not consistent with an eccentric disks, and additionally have significant disk color asymmetries suggesting altered dust grains. 4/23 disks have significant brightness asymmetries or disk offsets that are not consistent with an eccentric disk, but no available color measurements. Finally, 4 disks are consistent with being axisymmetric, although all 4 have inner cavities meaning that a sculpting planet may still be present. To summarize, the majority of disks structures associated with sculpting by one or more planets, and provide great candidates for planet searches with upcoming instruments.

In addition to characterizing the morphologies for all 23 disks in our sample, I also explore correlations among stellar temperatures, ages, disk properties, and observed perturbations. I find significant trends between the vertical aspect ratio with the stellar temperature and disk radial extent, where the disks in our sample with the highest vertical aspect ratios are all around hotter stars with small R_0 values. I also find a tentative trend between the vertical aspect ratio and the dust grain size distribution power-law, q, where q increases with vertical aspect ratio. Finally, I confirm a trend between the disk color and stellar effective temperature, where the disk becomes increasingly red/neutral with increasing temperature. Such results have important implications on the evolution of debris disk systems around stars of various spectral types.

6.2 A Deep Dive into the Highly Asymmetrical Debris Disk Around HD 111520

Through an empirical analysis of GPI debris disks, I found that the majority of disks presented an asymmetry of some kind. In Chapter 4, I take a closer look at one of the most asymmetric disks from our sample, HD 111520. In this study, I reuse the GPI polarized intensity observations in J, H, & $K1$, but additionally include the total intensity observations in the same bands, as well as HST/STIS observations in the optical. A deeper empirical analysis is conducted in order to better understand the disk morphology and its highly asymmetrical nature. I confirm that the disk features

a large brightness and radial asymmetry, most prominent at shorter wavelengths. I also find that the radial location of the peak polarized intensity differs on either side of the star by 11 AU, suggesting that the disk may be eccentric, although, such an eccentricity does not fully explain the large brightness and radial asymmetry observed.

Most interestingly, observations of the disk halo with HST show the disk to be warped at larger separations, with a bifurcation feature in the NW, further suggesting that there may be a planet in this system creating an asymmetrical disk structure. Measuring the disk color shows that the brighter extension is bluer compared to the dimmer extension, suggesting that the two sides have different dust grain properties. This finding, along with the large brightness asymmetry, are consistent with the hypothesis that a giant impact occurred between two large bodies in the NW side of the disk, although confirming this based on NIR observations alone is not feasible. Follow-up imaging with ALMA to resolve the asymmetry in the dust mass distribution would be essential in order to confirm this scenario.

To summarize, the HD 111520 debris disk has several asymmetrical features and structures, including a warp, "fork", radial extent asymmetry, as well as a brightness and disk color asymmetry. While the warp, fork, and radial extent asymmetry strongly suggest the presence of a disk perturbing planet, the strong brightness and color asymmetry may require an additional mechanism, such as a recent giant collision.

6.3 Simulating the HD 111520 Debris Disk with REBOUND

Given the signs of an unseen planet in the HD 111520 system based on the conducted in Chapter 4, I attempt to simulate the complicated disk morphology using the code REBOUND. The goal of these simulations is to determine the feasibility of disk-planet interactions, as well as to constrain the possible mass and orbit of the planet responsible for the observed structures. I find that a $\sim$1 M_{jup}, eccentric planet that is inclined relative to the disk and is orbiting *outside* the warp location, is able to reproduce the majority of disk features including the warp, fork and radial extent asymmetry. Assuming an eccentricity of $\sim$0.4, I am able to place some constraints on the planet mass and orbit, where the planet is required to be at least 1 M_{jup} and have a semi-major axis of $\gtrsim$200 au in order to properly replicate the disk morphology.

To create the surface brightness asymmetry, a second eccentric,coplanar planet is required within the disk inner edge (50 au) in order to cause a pericenter glow on the NW side. However, with the planet configurations used I am unable to produce the 2 to 1 brightness asymmetry observed, suggesting that a second mechanism may be required as has been suggested from our analysis of the disk in Chapter 4. Again, a recent giant collision may be necessary to reproduce the brightness and color asymmetry observed. Our work demonstrates how debris disk morphologies alone can be used to learn more about the architecture and evolution of a system as a whole, and can provide planet constraints to determine potential targets for current/future instruments such as JWST/NIRCam and GPI 2.0.

6.4 The Road Ahead

In this work, I demonstrate how debris disks can be used as probes for small, wide-orbit planets that are difficult to detect with current high-contrast instruments. Additionally, the morphologies of these debris disks can be used to estimate the planet's mass and orbit, such as in the case of the HD 111520 system, which is useful for understanding the feasibility of detection with any instrument. Once the planet's mass and orbit in a particular system are constrained, the next step would be to confirm this planet is real through observations. While, as mentioned previously, such planets are difficult to detect, there are new/future facilities and instruments that show promising capabilities to reach higher contrasts than ever before.

For example, I show in Chapter 5 that the planet inferred from the HD 111520 disk morphology, which has an expected mass of $\sim$1 M_{jup}, is within reach of JWST/NIRCam. In comparison, other high-contrast instruments such as GPI were only able to reach a sensitivity down to $\sim$3 M_{jup}. Detecting this predicted HD 111520 planet with JWST/NIRCam would further help confirm our understanding of how planets interact with their debris disks, and would allow us to more confidently infer planets from debris disks with similar morphologies. Even in the case of a non-detection, this would still provide useful information and would allow us to constrain the planet's mass and orbit further. Other future instruments include GPI 2.0, currently being moved to Gemini North, which will have a higher sensitivity and smaller inner working angles compared to GPI. While only a small number of the disks in our sample are accessible from Gemini North, those that are accessible and show signs of perturbations will make great candidates for future planet searches.

Beyond the HD 111520 system, the work in this thesis can be applied to other debris disk systems as well. For example, both the HD 110058 and HD 115600 systems have evidence of warps in their disks as seen in Chapter 3. Future work may involve further characterization of their morphologies using multiwavelength observations (e.g. HST/STIS observations of the HD 110058 disk), followed up by N-body simulations to constrain the properties of potential warp-driving planets. Such analysis can then be applied to observing proposals and potentially directly detecting the inferred planets. This procedure is also not limited to disks with warps, but disks with other asymmetric structures such as spirals (e.g. CE Ant), radial extent asymmetries (e.g. HD 30447), and multiple rings (e.g. HD 131835).

To summarize, my graduate work can be used beyond the sample of GPI debris disks presented in this thesis to better characterize debris disk morphologies in both a uniform and individual manner. By characterizing disk morphologies, we can reveal substructures and asymmetries that strongly suggest planet-disk interactions. Through N-body simulations, we can use the revealed disk substructures/asymmetries to constrain the mass and orbit of the perturbing planet, which will help determine the feasibility of direct detection with any instrument. The ultimate goal is to better understand planet-disk interactions, exoplanet demographics/populations, and the evolution of exoplanetary systems.

Bibliography

Acke, B., Min, M., Dominik, C., et al. 2012, *Astronomy & Astrophysics*, 540, A125, doi: 10.1051/0004-6361/201118581

Apai, D., Schneider, G., Grady, C. A., et al. 2015, *the Astrophysical Journal*, 800, 136, doi: 10.1088/0004-637X/800/2/136

Artymowicz, P. 1997, *Annual Review of Earth and Planetary Sciences*, 25, 175, doi: 10.1146/annurev.earth.25.1.175

Aumann, H. H., Gillett, F. C., Beichman, C. A., et al. 1984, *the Astrophysical Journal Letters*, 278, L23, doi: 10.1086/184214

Bailey, V., Meshkat, T., Reiter, M., et al. 2014, *the Astrophyical Journal Letters*, 780, L4, doi: 10.1088/2041-8205/780/1/L4

Bell, C. P. M., Mamajek, E. E., & Naylor, T. 2015, *Monthly Notices of the Royal Astronomical Society*, 454, 593, doi: 10.1093/mnras/stv1981

Bhowmik, T., Boccaletti, A., Thébault, P., et al. 2019, *Astronomy & Astrophysics*, 630, A85, doi: 10.1051/0004-6361/201936076

Bitsch, B., Trifonov, T., & Izidoro, A. 2020, *Astronomy & Astrophysics*, 643, A66, doi: 10.1051/0004-6361/202038856

Boccaletti, A., Augereau, J. C., Marchis, F., & Hahn, J. 2003, *the Astrophysical Journal*, 585, 494, doi: 10.1086/346019

Boccaletti, A., Sezestre, E., Lagrange, A. M., et al. 2018, *Astronomy & Astrophysics*, 614, A52, doi: 10.1051/0004-6361/201732462

Bowler, B. P., Blunt, S. C., & Nielsen, E. L. 2020, *the Astronomical Journal*, 159, 63, doi: 10.3847/1538-3881/ab5b11

Bowler, B. P., Tran, Q. H., Zhang, Z., et al. 2023, *the Astronomical Journal*, 165, 164, doi: 10.3847/1538-3881/acbd34

Brandner, W., Apai, D., Lenzen, R., Feldt, M., & Huélamo, N. 2005, in Astronomical Society of the Pacific Conference Series, Vol. 343, Astronomical Polarimetry: Current Status and Future Directions, ed. A. Adamson, C. Aspin, C. Davis, & T. Fujiyoshi, 75

Bruzzone, J. S. 2018, PhD thesis, University of Western Ontario, Canada

Buenzli, E., Thalmann, C., Vigan, A., et al. 2010, *Astronomy & Astrophysics*, 524, L1

Burns, J. A., Lamy, P. L., & Soter, S. 1979, *Icarus*, 40, 1, doi: 10.1016/0019-1035(79)90050-2

Carter, A. L., Skemer, A. J. I., Danielski, C., et al. 2021, in Society of Photo-Optical Instrumentation Engineers (SPIE) Conference Series, Vol. 11823, Techniques and Instrumentation for Detection of Exoplanets X, ed. S. B. Shaklan & G. J. Ruane, 118230H, doi: 10.1117/12.2594501

Carter, A. L., Hinkley, S., Kammerer, J., et al. 2023, *the Astrophysical Journal Letters*, 951, L20, doi: 10.3847/2041-8213/acd93e

Cataldi, G., Wu, Y., Brandeker, A., et al. 2020, *the Astrophysical Journal*, 892, 99, doi: 10.3847/1538-4357/ab7cc7

Chatterjee, S., Ford, E. B., Matsumura, S., & Rasio, F. A. 2008, *the Astrophysical Journal*, 686, 580, doi: 10.1086/590227

Chauvin, G., Lagrange, A. M., Beust, H., et al. 2012, *Astronomy & Astrophysics*, 542, A41, doi: 10.1051/0004-6361/201118346

Chen, C., Mazoyer, J., Poteet, C. A., et al. 2020, *the Astrophysical Journal*, 898, 55, doi: 10.3847/1538-4357/ab9aba

Chen, C. H., Mittal, T., Kuchner, M., et al. 2014, *the Astrophysical Journal Supplement Series*, 211, 25, doi: 10.1088/0067-0049/211/2/25

Chiang, E., & Fung, J. 2017, *the Astrophysical Journal*, 848, 4, doi: 10.3847/1538-4357/aa89e6

Choquet, É., Perrin, M. D., Chen, C. H., et al. 2016, *the Astrophysical Journal Letters*, 817, L2, doi: 10.3847/2041-8205/817/1/L2

Churcher, L., Wyatt, M., & Smith, R. 2011, *Monthly Notices of the Royal Astronomical Society*, 410, 2, doi: 10.1111/j.1365-2966.2010.17422.x

Crotts, K. A., Matthews, B. C., Esposito, T. M., et al. 2021, *the Astrophysical Journal*, 915, 58, doi: 10.3847/1538-4357/abff5c

Crotts, K. A., Draper, Z. H., Matthews, B. C., et al. 2022, *the Astrophysical Journal*, 932, 23, doi: 10.3847/1538-4357/ac6c86

Crotts, K. A., Matthews, B. C., Duchêne, G., et al. 2024, *the Astrophysical Journal*, 961, 245, doi: 10.3847/1538-4357/ad0e69

Currie, T., Lisse, C. M., Kuchner, M., et al. 2015, *the Astrophysical Journal Letters*, 807, L7, doi: 10.1088/2041-8205/807/1/L7

Cutri, R. M., Skrutskie, M. F., van Dyk, S., et al. 2003, VizieR Online Data Catalog, 2246, 0

Daemgen, S., Todorov, K., Quanz, S. P., et al. 2017, *Astronomy & Astrophysics*, 608, A71, doi: 10.1051/0004-6361/201731527

Daley, C., Hughes, A. M., Carter, E. S., et al. 2019, *the Astrophysical Journal*, 875, 87, doi: 10.3847/1538-4357/ab1074

Dawson, R. I., Murray-Clay, R. A., & Fabrycky, D. C. 2011, *the Astrophysical Journal Letters*, 743, L17, doi: 10.1088/2041-8205/743/1/L17

De Rosa, R. J., Nguyen, M. M., Chilcote, J., et al. 2020, *Journal of Astronomical Telescopes, Instruments, and Systems*, 6, 015006, doi: 10.1117/1.JATIS.6.1.015006

de Zeeuw, P. T., Hoogerwerf, R., de Bruijne, J. H. J., Brown, A. G. A., & Blaauw, A. 1999, *the Astronomical Journal*, 117, 354

Debes, J. H., Weinberger, A. J., & Kuchner, M. J. 2009, *the Astrophysical Journal*, 702, 318, doi: 10.1088/0004-637X/702/1/318

Delgrande, J. J., & Soanes, S. V. 1943, *Journal of the Royal Astronomical Society of Canada*, 37, 187

Dent, W. R. F., Wyatt, M. C., Roberge, A., et al. 2014, Science, 343, 1490, doi: 10.1126/science.1248726

Dohnanyi, J. S. 1969, *Journal of Geophysics Research*, 74, 2531, doi: 10.1029/JB074i010p02531

Donaldson, J. K., Lebreton, J., Roberge, A., Augereau, J. C., & Krivov, A. V. 2013, *the Astrophysical Journal*, 772, 17, doi: 10.1088/0004-637X/772/1/17

Draine, B. T. 2003, *Annual Review of Astronomy & Astrophysics*, 41, 241, doi: 10.1146/annurev.astro.41.011802.094840

Draper, Z. H., Matthews, B. C., Kennedy, G. M., et al. 2016a, *Monthly Notices of the Royal Astronomical Society*, 456, 459, doi: 10.1093/mnras/stv2696

Draper, Z. H., Marois, C., Wolff, S., et al. 2014, in *Ground-based and Airborne Instrumentation for Astronomy V*, ed. S. K. Ramsay, I. S. McLean, & H. Takami, Vol. 9147, 91474Z, doi: 10.1117/12.2057156

Draper, Z. H., Duchêne, G., Millar-Blanchaer, M. A., et al. 2016b, *the Astrophysical Journal*, 826, 147, doi: 10.3847/0004-637X/826/2/147

Duchêne, G., Rice, M., Hom, J., et al. 2020, *the Astronomical Journal*, 159, 251, doi: 10.3847/1538-3881/ab8881

Engler, N., Schmid, H. M., Quanz, S. P., Avenhaus, H., & Bazzon, A. 2018, *Astronomy & Astrophysics*, 618, A151, doi: 10.1051/0004-6361/201832674

Engler, N., Schmid, H. M., Thalmann, C., et al. 2017, *Astronomy & Astrophysics*, 607, A90, doi: 10.1051/0004-6361/201730846

Engler, N., Lazzoni, C., Gratton, R., et al. 2020, *Astronomy & Astrophysics*, 635, A19, doi: 10.1051/0004-6361/201936828

Engler, N., Milli, J., Gratton, R., et al. 2022, arXiv e-prints, arXiv:2211.11767, doi: 10.48550/arXiv.2211.11767

Esposito, T. M., Fitzgerald, M. P., Graham, J. R., et al. 2016, *the Astronomical Journal*, 152, 85, doi: 10.3847/0004-6256/152/4/85

Esposito, T. M., Duchêne, G., Kalas, P., et al. 2018, *the Astronomical Journal*, 156, 47, doi: 10.3847/1538-3881/aacbc9

Esposito, T. M., Kalas, P., Fitzgerald, M. P., et al. 2020, *the Astronomical Journal*, 160, 24, doi: 10.3847/1538-3881/ab9199

Faber, P., & Quillen, A. C. 2007, *Monthly Notices of the Royal Astronomical Society*, 382, 1823, doi: 10.1111/j.1365-2966.2007.12490.x

Feldt, M., Olofsson, J., Boccaletti, A., et al. 2017, *Astronomy & Astrophysics*, 601, A7, doi: 10.1051/0004-6361/201629261

Follette, K. B. 2023, *Publications of the Astronomical Society of the Pacific*, 135, 093001, doi: 10.1088/1538-3873/aceb31

Foreman-Mackey, D., Hogg, D. W., Lang, D., & Goodman, J. 2013, *Publications of the ASP*, 125, 306, doi: 10.1086/670067

Forgan, D., & Rice, K. 2013, *Monthly Notices of the Royal Astronomical Society*, 432, 3168, doi: 10.1093/mnras/stt672

Gaia Collaboration. 2020, VizieR Online Data Catalog, I/350

Gaia Collaboration, Brown, A. G. A., Vallenari, A., et al. 2021, *Astronomy & Astrophysics*, 649, A1

Gallenne, A., Desgrange, C., Milli, J., et al. 2022, *Astronomy & Astrophysics*, 665, A41, doi: 10.1051/0004-6361/202244226

Gibbs, A., Wagner, K., Apai, D., et al. 2019, *the Astronomical Journal*, 157, 39, doi: 10.3847/1538-3881/aaf1bd

Goebel, S., Currie, T., Guyon, O., et al. 2018, *the Astronomical Journal*, 156, 279, doi: 10.3847/1538-3881/aaeb24

Goldreich, P., Lithwick, Y., & Sari, R. 2004, *Annual Review of Astronomy & Astrophysics*, 42, 549, doi: 10.1146/annurev.astro.42.053102.134004

Goldreich, P., & Lynden-Bell, D. 1965, *Monthly Notices of the Royal Astronomical Society*, 130, 97, doi: 10.1093/mnras/130.2.97

Greaves, J. S., Holland, W. S., Matthews, B. C., et al. 2016, *Monthly Notices of the Royal Astronomical Society*, 461, 3910, doi: 10.1093/mnras/stw1569

Guyon, O. 2018, *Annual Review of Astronomy & Astrophysics*, 56, 315, doi: 10.1146/annurev-astro-081817-052000

Hahn, J. M., & Malhotra, R. 2005, *the Astronomical Journal*, 130, 2392, doi: 10.1086/452638

Hales, A. S., Marino, S., Sheehan, P. D., et al. 2022, *the Astrophysical Journal*, 940, 161, doi: 10.3847/1538-4357/ac9cd3

Han, Y., Wyatt, M. C., & Dent, W. R. F. 2023, *Monthly Notices of the Royal Astronomical Society*, 519, 3257, doi: 10.1093/mnras/stac3769

Han, Y., Wyatt, M. C., & Matrà, L. 2022, *Monthly Notices of the Royal Astronomical Society*, 511, 4921, doi: 10.1093/mnras/stac373

Heap, S. R., Lindler, D. J., Lanz, T. M., et al. 2000, *the Astrophysical Journal*, 539, 435, doi: 10.1086/309188

Hedman, M. M., & Stark, C. C. 2015, *the Astrophysical Journal*, 811, 67, doi: 10.1088/0004-637X/811/1/67

Henyey, L. G., & Greenstein, J. L. 1941, *the Astrophysical Journal*, 93, 70, doi: 10.1086/144246

Hines, D. C., Schneider, G., Hollenbach, D., et al. 2007, *the Astrophysical Journal Letters*, 671, L165, doi: 10.1086/525016

Hom, J., Patience, J., Esposito, T. M., et al. 2020, *the Astronomical Journal*, 159, 31, doi: 10.3847/1538-3881/ab5af2

Hom, J., Patience, J., Chen, C. H., et al. 2024, *Monthly Notices of the Royal Astronomical Society*, 528, 6959, doi: 10.1093/mnras/stae368

Hughes, A. M., Duchêne, G., & Matthews, B. C. 2018, *Annual Review of Astronomy & Astrophysics*, 56, 541, doi: 10.1146/annurev-astro-081817-052035

Hung, L.-W., Fitzgerald, M. P., Chen, C. H., et al. 2015a, *the Astrophysical Journal*, 802, 138, doi: 10.1088/0004-637X/802/2/138

Hung, L.-W., Duchêne, G., Arriaga, P., et al. 2015b, *the Astrophysical Journal Letters*, 815, L14, doi: 10.1088/2041-8205/815/1/L14

Ingraham, P., Perrin, M. D., Sadakuni, N., et al. 2014, in *Society of Photo-Optical Instrumentation Engineers (SPIE) Conference Series*, Vol. 9147, 7, doi: 10.1117/12.2057437

Jackson, A. P., Wyatt, M. C., Bonsor, A., & Veras, D. 2014, *Monthly Notices of the Royal Astronomical Society*, 440, 3757, doi: 10.1093/mnras/stu476

Janson, M., Brandeker, A., Olofsson, G., & Liseau, R. 2021, *Astronomy & Astrophysics*, 646, A132, doi: 10.1051/0004-6361/202039990

Johnson, B. C., Lisse, C. M., Chen, C. H., et al. 2012, *the Astrophysical Journal*, 761, 45, doi: 10.1088/0004-637X/761/1/45

Jones, J. W., Chiang, E., Duchene, G., Kalas, P., & Esposito, T. M. 2023, arXiv e-prints, arXiv:2303.10189, doi: 10.48550/arXiv.2303.10189

Kalas, P., Fitzgerald, M. P., & Graham, J. R. 2007, *the Astrophysical Journal Letters*, 661, L85, doi: 10.1086/518652

Kalas, P., Graham, J. R., & Clampin, M. 2005, *Nature*, 435, 1067–1070, doi: 10.1038/nature03601

Kalas, P., Graham, J. R., Fitzgerald, M. P., & Clampin, M. 2013, *the Astrophysical Journal*, 775, 56, doi: 10.1088/0004-637X/775/1/56

Kalas, P., & Jewitt, D. 1995, *the Astronomical Journal*, 110, 794, doi: 10.1086/117565

Kalas, P. G., Rajan, A., Wang, J. J., et al. 2015, *the Astrophysical Journal*, 814, 32, doi: 10.1088/0004-637X/814/1/32

Kasper, M., Apai, D., Wagner, K., & Robberto, M. 2015, *the Astrophysical Journal Letters*, 812, L33, doi: 10.1088/2041-8205/812/2/L33

Kiefer, F., Lecavelier des Etangs, A., Augereau, J. C., et al. 2014, *Astronomy & Astrophysics*, 561, L10, doi: 10.1051/0004-6361/201323128

Kiefer, F., Van Grootel, V., Lecavelier des Etangs, A., et al. 2023, arXiv e-prints, arXiv:2301.07418, doi: 10.48550/arXiv.2301.07418

Kóspál, Á., Moór, A., Juhász, A., et al. 2013, *the Astrophysical Journal*, 776, 77, doi: 10.1088/0004-637X/776/2/77

Kral, Q., Marino, S., Wyatt, M. C., Kama, M., & Matrà, L. 2019, *Monthly Notices of the Royal Astronomical Society*, 489, 3670, doi: 10.1093/mnras/sty2923

Kral, Q., Matrà, L., Kennedy, G. M., Marino, S., & Wyatt, M. C. 2020, *Monthly Notices of the Royal Astronomical Society*, 497, 2811, doi: 10.1093/mnras/staa2038

Kratter, K., & Lodato, G. 2016, *Anual Review of Astronomy & Astrophysics*, 54, 271, doi: 10.1146/annurev-astro-081915-023307

Krivov, A. V., & Wyatt, M. C. 2021, *Monthly Notices of the Royal Astronomical Society*, 500, 718, doi: 10.1093/mnras/staa2385

Lagrange, A. M., Bonnefoy, M., Chauvin, G., et al. 2010, *Science*, 329, 57, doi: 10.1126/science.1187187

Lagrange, A. M., Langlois, M., Gratton, R., et al. 2016, *Astronomy & Astrophysics*, 586, L8, doi: 10.1051/0004-6361/201527264

Lagrange, A. M., Meunier, N., Rubini, P., et al. 2019, Nature Astronomy, 3, 1135, doi: 10.1038/s41550-019-0857-1

Langlois, M., Gratton, R., Lagrange, A. M., et al. 2021, *Astronomy & Astrophysics*, 651, A71, doi: 10.1051/0004-6361/202039753

Lee, E. J., & Chiang, E. 2016, *the Astrophysical Journal*, 827, 125

Lee, E. J., & Chiang, E. 2016, *the Astrophysical Journal*, 827, 125, doi: 10.3847/0004-637X/827/2/125

Lieman-Sifry, J., Hughes, A. M., Carpenter, J. M., et al. 2016, *the Astrophysical Journal*, 828, 25, doi: 10.3847/0004-637X/828/1/25

Lin, J. W., & Chiang, E. 2019, *the Astrophysical Journal*, 883, 68, doi: 10.3847/1538-4357/ab35da

Lisse, C. M., Chen, C. H., Wyatt, M. C., & Morlok, A. 2008, in 39th Annual Lunar and Planetary Science Conference, Lunar and Planetary Science Conference, 2119

Löhne, T. 2020, *Astronomy & Astrophysics*, 641, A75, doi: 10.1051/0004-6361/202037858

MacGregor, M. A., Wilner, D. J., Chandler, C., et al. 2016, *the Astrophysical Journal*, 823, 79, doi: 10.3847/0004-637X/823/2/79

MacGregor, M. A., Matrà, L., Kalas, P., et al. 2017, *the Astrophysical Journal*, 842, 8, doi: 10.3847/1538-4357/aa71ae

MacGregor, M. A., Weinberger, A. J., Hughes, A. M., et al. 2018, *the Astrophysical Journal*, 869, 75, doi: 10.3847/1538-4357/aaec71

MacGregor, M. A., Hurt, S. A., Stark, C. C., et al. 2022, *the Astrophysical Journal Letters*, 933, L1, doi: 10.3847/2041-8213/ac7729

Macintosh, B., Graham, J. R., Ingraham, P., et al. 2014, *Proceedings of the National Academy of Science*, 111, 12661, doi: 10.1073/pnas.1304215111

Macintosh, B., Chilcote, J. K., Bailey, V. P., et al. 2018, in *Society of Photo-Optical Instrumentation Engineers (SPIE) Conference Series*, Vol. 10703, Adaptive Optics Systems VI, ed. L. M. Close, L. Schreiber, & D. Schmidt, 107030K, doi: 10.1117/12.2314253

Macintosh, B. A., Graham, J. R., Palmer, D. W., et al. 2008, in *Proceedings of the SPIE*, Vol. 7015, Adaptive Optics Systems, 701518, doi: 10.1117/12.788083

Maire, J., Ingraham, P. J., De Rosa, R. J., et al. 2014a, in *Society of Photo-Optical Instrumentation Engineers (SPIE) Conference Series*, Vol. 9147, *Society of Photo-Optical Instrumentation Engineers (SPIE) Conference Series*, 85, doi: 10.1117/12.2056732

Maire, J., Ingraham, P. J., De Rosa, R. J., et al. 2014b, in *Proceedings of the SPIE*, Vol. 9147, Ground-based and Airborne Instrumentation for Astronomy V, 914785

Malhotra, R. 1995, *the Astronomical Journal*, 110, 420, doi: 10.1086/117532

Maness, H. L., Kalas, P., Peek, K. M. G., et al. 2009, *the Astrophysical Journal*, 707, 1098, doi: 10.1088/0004-637X/707/2/1098

Marino, S. 2021, *Monthly Notices of the Royal Astronomical Society*, 503, 5100, doi: 10.1093/mnras/stab771

Marois, C., Lafrenière, D., Doyon, R., Macintosh, B., & Nadeau, D. 2006, *the Astrophysical Journal*, 641, 556, doi: 10.1086/500401

Marois, C., Macintosh, B., Barman, T., et al. 2008, *Science*, 322, 1348, doi: 10.1126/science.1166585

Marois, C., Zuckerman, B., Konopacky, Q. M., Macintosh, B., & Barman, T. 2010, *Nature*, 468, 1080, doi: 10.1038/nature09684

Martioli, E., Hébrard, G., Correia, A. C. M., Laskar, J., & Lecavelier des Etangs, A. 2021, *Astronomy & Astrophysics*, 649, A177, doi: 10.1051/0004-6361/202040235

Mason, B. D., Hartkopf, W. I., & Friedman, E. A. 2012, *the Astronomical Journal*, 143, 124, doi: 10.1088/0004-6256/143/5/124

Matrà, L., Marino, S., Kennedy, G. M., et al. 2018, *the Astrophysical Journal*, 859, 72, doi: 10.3847/1538-4357/aabcc4

Matrà, L., Wyatt, M. C., Wilner, D. J., et al. 2019, *the Astronomical Journal*, 157, 135, doi: 10.3847/1538-3881/ab06c0

Matthews, B. C., Sibthorpe, B., Kennedy, G., et al. 2010, *Astronomy & Astrophysics*, 518, L135, doi: 10.1051/0004-6361/201014667

Matthews, E., Hinkley, S., Vigan, A., et al. 2017, *the Astrophysical Journal Letters*, 843, L12, doi: 10.3847/2041-8213/aa7943

Michel, A., van der Marel, N., & Matthews, B. C. 2021, *the Astrophysical Journal*, 921, 72, doi: 10.3847/1538-4357/ac1bbb

Millar-Blanchaer, M. A., Graham, J. R., Pueyo, L., et al. 2015, *the Astrophysical Journal*, 811, 18, doi: 10.1088/0004-637X/811/1/18

Millar-Blanchaer, M. A., Perrin, M. D., Hung, L.-W., et al. 2016, in *Society of Photo-Optical Instrumentation Engineers (SPIE) Conference Series*, Vol. 9908, Ground-based and Airborne Instrumentation for Astronomy VI, ed. C. J. Evans, L. Simard, & H. Takami, 990836, doi: 10.1117/12.2233071

Milli, J., Vigan, A., Mouillet, D., et al. 2017, *Astronomy & Astrophysics*, 599, A108, doi: 10.1051/0004-6361/201527838

Milli, J., Engler, N., Schmid, H. M., et al. 2019, *Astronomy & Astrophysics*, 626, A54, doi: 10.1051/0004-6361/201935363

Montesinos, B., Eiroa, C., Krivov, A. V., et al. 2016, *Astronomy & Astrophysics*, 593, A51, doi: 10.1051/0004-6361/201628329

Moore, N. W. H., Li, G., Hassenzahl, L., et al. 2023, *the Astrophysical Journal*, 943, 6, doi: 10.3847/1538-4357/aca766

Morrison, S., & Malhotra, R. 2015, *the Astrophysical Journal*, 799, 41, doi: 10.1088/0004-637X/799/1/41

Mouillet, D., Larwood, J. D., Papaloizou, J. C. B., & Lagrange, A. M. 1997, *Monthly Notices of the Royal Astronomical Society*, 292, 896

Mustill, A. J., & Wyatt, M. C. 2009, *Monthly Notices of the Royal Astronomical Society*, 399, 1403, doi: 10.1111/j.1365-2966.2009.15360.x

Nagpal, V., Blunt, S., Bowler, B. P., et al. 2023, *the Astronomical Journal*, 165, 32, doi: 10.3847/1538-3881/ac9fd2

Nesvold, E. R., Naoz, S., & Fitzgerald, M. P. 2017, *the Astrophysical Journal Letters*, 837, L6, doi: 10.3847/2041-8213/aa61a7

Neugebauer, G., Beichman, C. A., Soifer, B. T., et al. 1984, *Science*, 224, 14, doi: 10.1126/science.224.4644.14

Nguyen, M. M., De Rosa, R. J., & Kalas, P. 2021, *the Astronomical Journal*, 161, 22, doi: 10.3847/1538-3881/abc012

Nielsen, E. L., De Rosa, R. J., Wang, J., et al. 2016, *the Astronomical Journal*, 152, 175, doi: 10.3847/0004-6256/152/6/175

Nielsen, E. L., De Rosa, R. J., Macintosh, B., et al. 2019, *the Astronomical Journal*, 158, 13, doi: 10.3847/1538-3881/ab16e9

Nielsen, E. L., De Rosa, R. J., Wang, J. J., et al. 2020, *the Astronomical Journal*, 159, 71, doi: 10.3847/1538-3881/ab5b92

Norfolk, B. J., Maddison, S. T., Marshall, J. P., et al. 2021, *Monthly Notices of the Royal Astronomical Society*, 507, 3139, doi: 10.1093/mnras/stab1901

Olofsson, J., Milli, J., Bayo, A., Henning, T., & Engler, N. 2020, *Astronomy & Astrophysics*, 640, A12, doi: 10.1051/0004-6361/202038237

Olofsson, J., Samland, M., Avenhaus, H., et al. 2016, *Astronomy & Astrophysics*, 591, A108, doi: 10.1051/0004-6361/201628196

Olofsson, J., van Holstein, R. G., Boccaletti, A., et al. 2018, *Astronomy & Astrophysics*, 617, A109, doi: 10.1051/0004-6361/201832583

Olofsson, J., Milli, J., Thébault, P., et al. 2019, *Astronomy & Astrophysics*, 630, A142

Olofsson, J., Thébault, P., Kral, Q., et al. 2022, *Monthly Notices of the Royal Astronomical Society*, 513, 713, doi: 10.1093/mnras/stac455

Oppenheimer, B. R., & Hinkley, S. 2009, *Annual Review of Astronomy & Astrophysics*, 47, 253, doi: 10.1146/annurev-astro-082708-101717

Padgett, D., & Stapelfeldt, K. 2015, in IAU Symposium, Vol. 314, Young Stars & Planets Near the Sun, ed. J. H. Kastner, B. Stelzer, & S. A. Metchev, 175–178, doi: 10.1017/S1743921315006456

Pan, M., Nesvold, E. R., & Kuchner, M. J. 2016, *the Astrophysical Journal*, 832, 81, doi: 10.3847/0004-637X/832/1/81

Pan, M., & Schlichting, H. E. 2012, *the Astrophysical Journal*, 747, 113, doi: 10.1088/0004-637X/747/2/113

Patel, R. I., Metchev, S. A., & Heinze, A. 2014, *the Astrophysical Journal Supplement Series*, 212, 10, doi: 10.1088/0067-0049/212/1/10

Pearce, T. D., & Wyatt, M. C. 2014, *Monthly Notices of the Royal Astronomical Society*, 443, 2541

Pearce, T. D., Launhardt, R., Ostermann, R., et al. 2022, *Astronomy & Astrophysics*, 659, A135, doi: 10.1051/0004-6361/202142720

Pecaut, M. J., & Mamajek, E. E. 2016, *Monthly Notices of the Royal Astronomical Society*, 461, 794, doi: 10.1093/mnras/stw1300

Perrin, M. D., Maire, J., Ingraham, P., et al. 2014a, in *Society of Photo-Optical Instrumentation Engineers (SPIE) Conference Series*, Vol. 9147, Ground-based and Airborne Instrumentation for Astronomy V, ed. S. K. Ramsay, I. S. McLean, & H. Takami, 91473J, doi: 10.1117/12.2055246

Perrin, M. D., Maire, J., Ingraham, P., et al. 2014b, in *Society of Photo-Optical Instrumentation Engineers (SPIE) Conference Series*, Vol. 9147, *Society of Photo-Optical Instrumentation Engineers (SPIE) Conference Series*, 3, doi: 10.1117/12.2055246

Perrin, M. D., Duchene, G., Millar-Blanchaer, M., et al. 2015, *the Astrophysical Journal*, 799, 182, doi: 10.1088/0004-637X/799/2/182

Petit, J.-M., Morbidelli, A., & Chambers, J. 2001, *Icarus*, 153, 338, doi: 10.1006/icar.2001.6702

Phillips, M. W., Tremblin, P., Baraffe, I., et al. 2020, *Astronomy & Astrophysics*, 637, A38, doi: 10.1051/0004-6361/201937381

Pickles, A. J. 1998, *Publications of the ASP*, 110, 863, doi: 10.1086/316197

Plavchan, P., Barclay, T., Gagné, J., et al. 2020, *Nature*, 582, 497, doi: 10.1038/s41586-020-2400-z

Rebollido, I., Stark, C. C., Kammerer, J., et al. 2024, *the Astronomical Journal*, 167, 69, doi: 10.3847/1538-3881/ad1759

Rein, H., & Liu, S. F. 2012, *Astronomy & Astrophysics*, 537, A128, doi: 10.1051/0004-6361/201118085

Ren, B., Choquet, É., Perrin, M. D., et al. 2019, *the Astrophysical Journal*, 882, 64, doi: 10.3847/1538-4357/ab3403

—. 2021, *the Astrophysical Journal*, 914, 95, doi: 10.3847/1538-4357/ac03b9

Ren, B. B., Rebollido, I., Choquet, É., et al. 2023, *Astronomy & Astrophysics*, 672, A114, doi: 10.1051/0004-6361/202245458

Rodet, L., Beust, H., Bonnefoy, M., et al. 2019, *Astronomy & Astrophysics*, 631, A139, doi: 10.1051/0004-6361/201935728

Schmid, H. M., Joos, F., & Tschan, D. 2006, *Astronomy & Astrophysics*, 452, 657, doi: 10.1051/0004-6361:20053273

Schneider, G., Grady, C. A., Hines, D. C., et al. 2014, *the Astronomical Journal*, 148, 59, doi: 10.1088/0004-6256/148/4/59

Schneiderman, T., Matrà, L., Jackson, A. P., et al. 2021, *Nature*, 598, 425, doi: 10.1038/s41586-021-03872-x

Sibthorpe, B., Kennedy, G. M., Wyatt, M. C., et al. 2018, *Monthly Notices of the Royal Astronomical Society*, 475, 3046, doi: 10.1093/mnras/stx3188

Smirnov-Pinchukov, G. V., Moór, A., Semenov, D. A., et al. 2022, *Monthly Notices of the Royal Astronomical Society*, 510, 1148, doi: 10.1093/mnras/stab3146

Smith, B. A., & Terrile, R. J. 1984, Science, 226, 1421, doi: 10.1126/science.226.4681.1421

Soummer, R., Perrin, M. D., Pueyo, L., et al. 2014, *the Astrophysical Journal Letters*, 786, L23, doi: 10.1088/2041-8205/786/2/L23

Stamatellos, D., & Whitworth, A. P. 2009, *Monthly Notices of the Royal Astronomical Society*, 392, 413, doi: 10.1111/j.1365-2966.2008.14069.x

Stapelfeldt, K. R., Holmes, E. K., Chen, C., et al. 2004, *the Astrophysical Journal Supplement Series*, 154, 458, doi: 10.1086/423135

Stasevic, S., Milli, J., Mazoyer, J., et al. 2023, *Astronomy & Astrophysics*, 678, A8, doi: 10.1051/0004-6361/202346720

Su, K. Y. L., Rieke, G. H., Misselt, K. A., et al. 2005, *the Astrophysical Journal*, 628, 487, doi: 10.1086/430819

Takasawa, S., Nakamura, A. M., Kadono, T., et al. 2011, *the Astrophysical Journal Letters*, 733, L39, doi: 10.1088/2041-8205/733/2/L39

Tamayo, D., Rein, H., Shi, P., & Hernandez, D. M. 2020, *Monthly Notices of the Royal Astronomical Society*, 491, 2885, doi: 10.1093/mnras/stz2870

Telesco, C. M., Fisher, R. S., Wyatt, M. C., et al. 2005, *Nature*, 433, 133, doi: 10.1038/nature03255

Terrill, J., Marino, S., Booth, R. A., et al. 2023, *Monthly Notices of the Royal Astronomical Society*, doi: 10.1093/mnras/stad1847

Thalmann, C., Janson, M., Buenzli, E., et al. 2013, *the Astrophysical Journal Letters*, 763, L29, doi: 10.1088/2041-8205/763/2/L29

Thebault, P., & Kral, Q. 2019, *Astronomy & Astrophysics*, 626, A24, doi: 10.1051/0004-6361/201935341

Thilliez, E., & Maddison, S. T. 2017, *Monthly Notices of the Royal Astronomical Society*, 464, 1434, doi: 10.1093/mnras/stw2427

Thommes, E. W., Duncan, M. J., & Levison, H. F. 2002, *the Astronomical Journal*, 123, 2862, doi: 10.1086/339975

Thureau, N. D., Greaves, J. S., Matthews, B. C., et al. 2014, *Monthly Notices of the Royal Astronomical Society*, 445, 2558, doi: 10.1093/mnras/stu1864

Toomre, A. 1964, *the Astrophysical Journal*, 139, 1217, doi: 10.1086/147861

Torres, C. A. O., Quast, G. R., da Silva, L., et al. 2006, *Astronomy & Astrophysics*, 460, 695, doi: 10.1051/0004-6361:20065602

Trilling, D. E., Bryden, G., Beichman, C. A., et al. 2008, *the Astrophysical Journal*, 674, 1086, doi: 10.1086/525514

Vizgan, D., Hughes, A. M., Carter, E. S., et al. 2022, *the Astrophysical Journal*, 935, 131, doi: 10.3847/1538-4357/ac80b8

Wahhaj, Z., Milli, J., Kennedy, G., et al. 2016, *Astronomy & Astrophysics*, 596, L4, doi: 10.1051/0004-6361/201629769

Wang, J. J., Ruffio, J.-B., De Rosa, R. J., et al. 2015, pyKLIP: PSF Subtraction for Exoplanets and Disks, Astrophysics Source Code Library, record ascl:1506.001. http://ascl.net/1506.001

Wang, J. J., Rajan, A., Graham, J. R., et al. 2014a, in *Society of Photo-Optical Instrumentation Engineers (SPIE) Conference Series*, Vol. 9147, Ground-based and Airborne Instrumentation for Astronomy V, ed. S. K. Ramsay, I. S. McLean, & H. Takami, 914755, doi: 10.1117/12.2055753

Wang, J. J., Rajan, A., Graham, J. R., et al. 2014b, in *Society of Photo-Optical Instrumentation Engineers (SPIE) Conference Series*, Vol. 9147, 55, doi: 10.1117/12.2055753

Wisdom, J. 1980, *the Astronomical Journal*, 85, 1122, doi: 10.1086/112778

Wolff, S. G., Perrin, M. D., Maire, J., et al. 2014, in *Society of Photo-Optical Instrumentation Engineers (SPIE) Conference Series*, Vol. 9147, *Society of Photo-Optical Instrumentation Engineers (SPIE) Conference Series*, 7, doi: 10.1117/12.2055678

Wyatt, M. C. 2005, *Astronomy & Astrophysics*, 433, 1007, doi: 10.1051/0004-6361:20042073

—. 2006, *the Astrophysical Journal*, 639, 1153, doi: 10.1086/499487

—. 2008, *Annual Review of Astronomy & Astrophysics*, 46, 339, doi: 10.1146/annurev.astro.45.051806.110525

Wyatt, M. C., Clarke, C. J., & Booth, M. 2011, Celestial Mechanics and Dynamical Astronomy, 111, 1, doi: 10.1007/s10569-011-9345-3

Wyatt, M. C., Dermott, S. F., Telesco, C. M., et al. 1999, *the Astrophysical Journal*, 527, 918, doi: 10.1086/308093

Xie, C., Choquet, E., Vigan, A., et al. 2022, *Astronomy & Astrophysics*, 666, A32, doi: 10.1051/0004-6361/202243379

Zakhozhay, O. V., Launhardt, R., Trifonov, T., et al. 2022, *Astronomy & Astrophysics*, 667, L14, doi: 10.1051/0004-6361/202244747

Zhou, J.-L., & Sun, Y.-S. 2003, *the Astrophysical Journal*, 598, 1290, doi: 10.1086/379061

Zuckerman, B. 2019, *the Astrophysical Journal*, 870, 27, doi: 10.3847/1538-4357/aaee66